Multi-terminal VSC-HVDC Based Offshore Wind-Farms Integration System Operation and Control

by

Mohamed A Abdelwahed

A thesis
presented to the University of Waterloo
in fulfillment of the
thesis requirement for the degree of
Doctor of Philosophy
in
Electrical and Computer Engineering

Waterloo, Ontario, Canada, 2017

Examining Committee Membership

The following served on the Examining Committee for this thesis. The decision of the Examining Committee is by majority vote.

External Examiner	Osama A. Mohammed Professor Department of Electrical and Computer Engineering Florida International University
Supervisor	Ehab F. El-Saadany Professor Department of Electrical and Computer Engineering University of Waterloo
Internal Member	Ramadan A. El-Shatshat Lecturer Department of Electrical and Computer Engineering University of Waterloo
Internal Member	Tarek Abdel-Galil Adjunct Assistant Professor Department of Electrical and Computer Engineering University of Waterloo
Internal-external Member	Gordon Savage Professor Department of System Design Engineering University of Waterloo

I hereby declare that I am the sole author of this thesis. This is a true copy of the thesis, including any required final revisions, as accepted by my examiners.

I understand that my thesis may be made electronically available to the public.

Abstract

Worldwide, many countries direct billions of dollars into the development of renewable energy sources; especially wind generation, in an effort to relieve global warming effects and other environmental concerns. As a result of increasing numbers of remotely-located large power offshore wind farms, the AC grid faces many technical challenges in integrating such plants; such as large submarine power transmission for extended distances, power sharing and transfer, as well as remotely located induction generation reactive power support. Offshore multi-terminal VSC based HVDC (MT VSC-HVDC) transmission systems represent a possible means of dealing with those challenges. This is due to their higher capacity, flexibility and controllability than offshore AC transmission. In addition, these offshore grids provide grid integration to remote offshore wind farms leading providing additional interconnection capacity to improve the trade of electricity between different AC grids.

This work presents a new centralized supervisory control strategy for controlling the power sharing and voltage regulation of MT VSC-HVDC integrating offshore wind farms. The main purpose of the proposed strategy is selecting the optimal parameters of the HVDC system VSCs' local controller. These optimal parameters are selected in order to achieve optimal system transient response and desired steady state operation.

In this work, an adaptive droop-based power-sharing control strategy is proposed. The primary objective is to control the sharing of the active power transmitted by a MT VSC-HVDC network among a number of onshore AC grids or offshore loads based on the desired percentage shares. The shared power is generated by remote generation plants (e.g., offshore wind farms) or is provided as surplus of AC grids. The desired percentage shares of active power are optimized by the system operator to fulfill the active power requirements of the connected grids with respect to meeting goals such as supporting energy adequacy, increasing renewable energy penetration, and minimizing losses. The control strategy is based on two hierarchal levels: voltage-droop control as the primary controller and an optimization based secondary (supervisory) controller for selecting the optimal droop reference voltages. Based on the DC voltage transient and steady state dynamics, a methodology for choosing the droop gains for droop controlled converters has been developed.

In addition, a new tuning methodology is proposed for selecting the optimum VSCs

local controller gains to enhance the transient performance and the small-signal stability of the system to mitigate the change of the operating conditions, taking into consideration the overall dynamics of the MT HVDC system. The VSCs' local control loops gains are selected to maximize the system bandwidth and improve the system damping. As a part of the proposed methodology, the derivation of the aggregated linearized state-space model of a MT VSC-HVDC based offshore transmission system is provided. Based on the derived model, a small signal stability analysis was performed to show the interaction of the modes and define the dominant eigenvalues of the system.

Furthermore, a communication-free DC voltage control strategy is presented for mitigating the effects of the power imbalance caused by permanent or temporary power-receiving converter outages. The proposed control strategy is targeted at fast power reduction of the wind power generation from the wind farms (WFs) in order to eliminate power imbalances in the HVDC network. This process is performed by decentralized control rules in the local controllers of the WF voltage source converter (VSC) and its wind turbines. The proposed strategy was designed to work with WFs based on both doubly fed induction generators (DFIGs) and permanent magnet synchronous generators (PMSGs).

The proposed control strategies were validated on the B4 CIGRE MT VSC-HVDC test system and different case scenarios were applied to show its feasibility and robustness. The validation process was performed using Matlab software programming and Matlab/Simulink based time domain detailed model.

Acknowledgments

Firstly, praise to Allah for his graces, blessing and guidance always and forever.

I would like to express my sincere gratitude to my advisor Prof. Ehab El-Saadany for the continuous support of my Ph.D study and related research. His guidance helped me in all the time of research and writing of this thesis. I could not have imagined having a better advisor and mentor for my Ph.D study. Besides my advisor, My thanks and appreciation are extend the rest of my thesis committee: Prof. Osama Mohammed, Assistant Prof. Tarek Abdelgalil, Dr. Ramadan El-Shatshat, and Prof. Gordon Savage, for their insightful comments and encouragement.

My deepest thanks and endless gratitude goes always to my mother, Nagwa Ali, for her support, encouragement, and continuous prayers. Also, I would like to express my special thanks and appreciation to my wife and my life partner, Yassmin Allam, who always does the best for me and our family. In addition, I thank my siblings for supporting me spiritually throughout writing this thesis and my life in general.

Last but not the least, I would like to thank my research colleagues and my friends for their support, helpful advises and assistance in my research work and thesis writing.

Mohamed Abdelaziz Abdelwahed

University of Waterloo

July 2017

Dedication

"Praise to Allah , who has guided us to this; and we would never have been guided if Allah had not guided us."[1]

To my father, Abdelaziz,

To my mather, Nagwa,

To my wife, Yassmin,

To my children, Hana, Leen, Seba and Belaal

To my siblings, Mahmoud, Ahmed, Lubna, Omar, Hossam and Neamat.

[1] *Holy Quran*, Al-A'raaf - 43

Table of Contents

List of Tables

List of Figures

Nomenclature

Acronyms

AC	Alternating Current
DC	Direct Current
DVC	Direct Voltage Control
FRT	Fault Ride Through
GS	Grid Side
HVDC	High Voltage Direct Current
LCC	Line Commutated Converter
MT	Multi-terminal
OPF	Optimal Power Flow
PCC	Point of Common Coupling
PWM	Pulse Width Modulation
SCR	Short Circuit Ratio
VMM	Voltage Margin Method
VSC	Voltage Sources Converter

WF	Wind Farm

Parameters

$\boldsymbol{A}$	a linearized state-space model state matrix
$\boldsymbol{B}$	a linearized state-space model input matrix
$\boldsymbol{C}$	a linearized state-space model output matrix
$\boldsymbol{D}$	a linearized state-space model disturbance matrix
ω_o	The AC grid nominal frequency in rad/sec
C_{DC}	The VSC DC capacitor
C_f	The AC filter capacitor
C_{ij}	The capacitance of the line between buses i and j
DF	the deloading factor of the wind farm
DF_{min}	the minimum de-loading factor of the wind farm
F_{WF_o}	the wind farm nominal frequency
G_{ij}	The conductance of the line between buses i and j
K_{i_d}	The Integral gain of the d-axis outer control loop PI controller of the GS VSC
$K_{i_{in}}$	The Integral gain of the inner control loop PI controller
$K_{i_{out}}$	The Integral gain of the outer control loop PI controller of the WF-VSC
$K_{i_{pll}}$	The Integral gain of PLL
K_{i_q}	The Itegral gain of the q-axis outer control loop PI controller of the GS VSC

K_{P_d}	The proportional gain of the d-axis outer control loop PI controller of the GS VSC
$K_{P_{in}}$	The proportional gain of the inner control loop PI controller
$K_{P_{out}}$	The proportional gain of the outer control loop PI controller of the WF-VSC
$K_{P_{pll}}$	The proportional gain of the PLL
K_{P_q}	The proportional gain of the q-axis outer control loop PI controller of the GS VSC
L_f	The AC filter reactor inductance
L_g	The AC grid equivalent inductance
L_{ij}	The inductance of the line between buses i and j
$P_{W_{rated}}$	the wind farm per-unit rated power
R_D	The droop gain
R_f	The AC filter reactor resistance
R_g	The AC grid equivalent resistance
R_{ij}	The resistance of the line between buses i and j
$V_{dc_{max}}$	the maximum DC voltage
$V_{dc_{min}}$	the minimum DC voltage
$V_{dc_{th}}$	the DC voltage threshold
$V_{o_{max}}$	the maximum no-load voltage parameter
V_o	The DC voltage at no-load
Z_g	The AC grid equivalent impedance

Indices and Sets

M	the set of power input buses (buses of rectification mode VSCs)
N	the set of power output buses (buses of inversion mode VSCs)
n_λ	The number of eigenvalues
n_{b_i}	the set of buses connected to the bus i
N_b	the set of all DC grid buses
O	the set of connection buses (no VSCs are connected)

Variables

$(.)^*$	the refernce value of the variable (.)
$\boldsymbol{H}$	the steady-state gain matrix
$\boldsymbol{l}$	The left eigenvector
$\boldsymbol{r}$	The right eigenvector
$\Delta \boldsymbol{I}_{max}$	the vector of maximum change in the input currents to the HVDC grid
ΔV_{max}	the maximum DC voltage deviation
λ	The eigenvalue
ω	The AC grid radial frequency
σ	the real part of an eigenvalue
θ_{pll}	The PLL output angle
F_{WF}	the wind farm frequency
I_{dc}	The VSC output DC current
i_f	The AC filter reactor current

n	the percentage power share
P	The active power
P_G	the active power input (generation) to the DC grid
P_{loss}	the transmission power loss in the DC grid
P_{max}	the maximum wind power generation command signal
Q	The reactive power
U	an AC voltage
U_c	The AC voltage at the converter AC terminals
U_t	The AC voltage at the PCC point of the VSC
u_{WF}	the wind farm AC voltage
V	a DC voltage
V_{dc}	The DC voltage at the terminals of the VSC
$\boldsymbol{G}(s)$	the closed loop transfer matrix
I_{ij}	The DC current of the line connecting buses i and j
U_g	The AC grid voltage
x	a state variable

Chapter 1

Introduction

1.1 Preface

Wind power generation is expected to increase worldwide. The European Wind Energy Association (EWEA) anticipates that installed wind farms (WFs) will generate approximately 180 GW annually by 2020 and 300 GW by 2030 [3], with a considerable contribution from offshore wind farms. The rise in offshore wind generation is attributable to a number of factors, such as the limited number of suitable onshore sites, as well as the associated visual and noise pollution that gives rise to public opposition to future onshore installations. Offshore sites can also harness wind speeds of up to 20 percent higher velocities, with resulting energy yields up to 70 percent greater than on land [4], [1]. Due to increases in the size of offshore WFs and their distance, as shown in Fig. 1.1 [1], their integration with onshore AC grids using AC transmission, is limited by the reactive power demand of both submarine cables, and wind-turbine induction generators [5].

High-voltage direct current (HVDC) transmission systems, Fig. 1.2, especially the ones equipped with voltage- source converters (VSCs), are considered a promising solution in the field of offshore bulk power transmission because of their considerable advantages: ability to connect asynchronous AC grids that have different frequencies, higher flexibility and controllability, limited short-circuit fault currents, smaller filters, and black-start capabilities [6], [7]. In addition, the use of multi-terminal (MT) HVDC networks, rather than

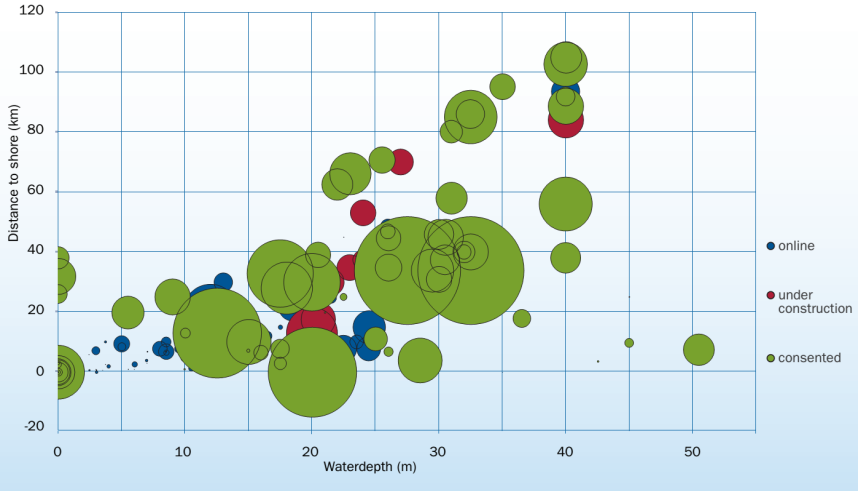

Figure 1.1: Typical European offshore wind farms distances from the shore, water depth and sizes [1]

point-to-point HVDC links, increases system reliability, power-trading capability, and the ability of smooth wind power fluctuations [8], [9].

1.2 Research Motivation

The integration of remotely located power generation plants, such as offshore wind farms, into the AC grid faces a number of challenges. For example, there are problems that may appear when disconnecting these power generation plants after fault. Moreover, there is a need for transferring huge amounts of power and the need for more reactive power support for induction based generation [10]. These challenges stimulate more interest in MT HVDC transmission systems which benefit from the technological advances of power electronics and VSC technologies. Point-to-point and multi-terminal HVDC transmission, based on LCC converter technology, research has been conducted in the past. However, recently, VSC based HVDC system has become a new topic of research, especially multi-terminal VSC-HVDC systems.

Nowadays, there are three multi-terminal HVDC systems in operation. The first MT HVDC system was installed by ABB, based on LCC technology, in Canada in 1986 as a

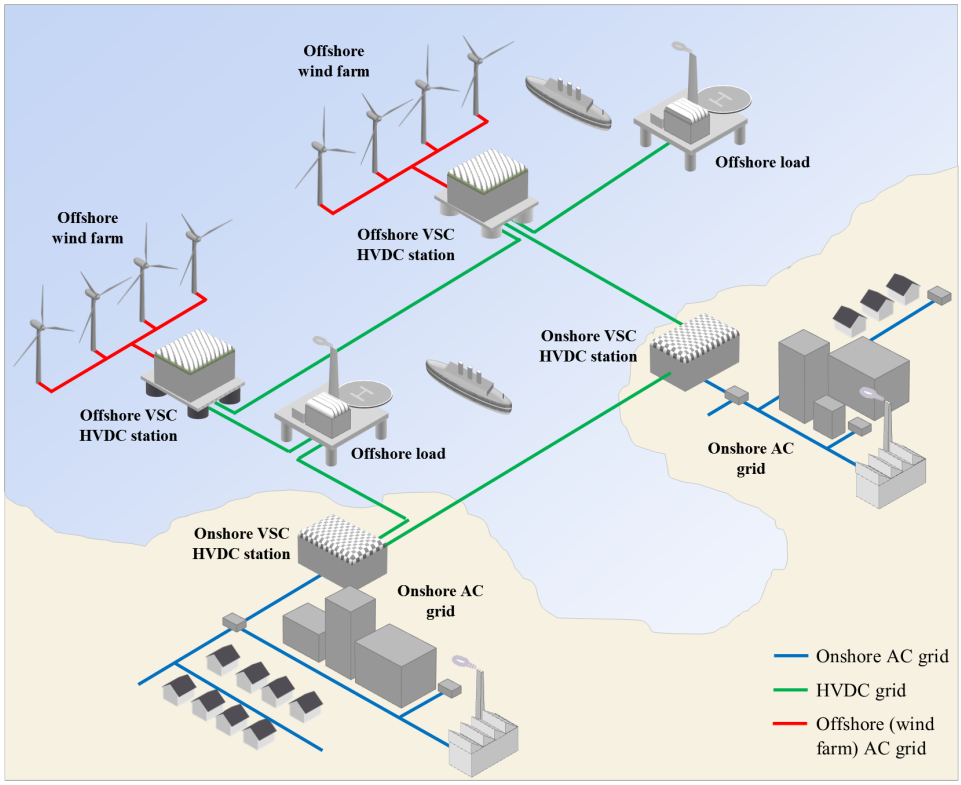

Figure 1.2: Typical multi-terminal VSC-HVDC based offshore wind farms integration system

point-to-point HVDC link between Quebec and New England. A third terminal in Massachusetts, USA, was added in 1992, creating the first three terminal HVDC system, and it is planned to be extended to become a 5 terminal system [11]. The second multi-terminal HVDC grid is Italy-Corsica-Sardinia, which is a three terminal LCC-HVDC system deployed in 2012 [12]. The third system is the Shin-Shinano substation in Japan, which was installed in 1999 [13]. The substation consists of three back-to-back VSCs to connect a 50Hz grid with other 60 Hz grids. This system cannot be considered a genuine MT VSC-HVDC system due to lack of transmission lines between the converters. The North Sea region is one of the areas that can benefit from the advantages of the MT-HVDC transmission system, due to the existence of offshore wind farms, offshore oil/gas platforms, and the need to connect some AC grids, such as English, Swedish and Norwich grids, to the

European continental AC grid.

The MT VSC-HVDC technology needs to mature before being used in practical and commercial applications. Despite encouraging works in the literature on operation, control and protection of VSC-based MT HVDC, there still remain several gaps in this system which need further investigation and understanding such as:

1. On large scale MT HVDC system, an accurate power sharing control and voltage regulation based on predefined desired shares using DC voltage droop control is needed. In addition, the droop gains effects on the DC voltage dynamics need to be studied, thus, a methodology of selecting the droop gains considering the DC grid voltage dynamics is required.

2. Due to the nonlinearity of the MT VSC-HVDC systems, Local VSCs controller parameters need to be tuned to mitigate the change in the operating conditions to maximize the system bandwidth and minimize the damping. The overall HVDC network dynamics and the interaction between the different components of the system should be considered in the tuning algorithm.

3. While sufficient work has been done in the area of temporary outage, caused by an AC fault in the onshore grid, fault ride through in offshore wind farm integration systems based on point-to-point HVDC transmission, few of them deal with MT VSC-HVDC networks. The permanent or long-time onshore converter outage case scenarios in MT HVDC system were not studied. Hence, a new communication-free DC voltage control strategy is needed to relieve the effects of permanent onshore VSC outages in offshore MT HVDC systems by regulating the DC voltage of the HVDC network with improved system power and voltage dynamics.

1.3 Research Objectives and contributions

1.3.1 Research Objectives

The proposed work focuses on the integration of offshore wind farms and loads to different onshore AC grids using offshore MT VSC-HVDC transmission systems. In such systems,

the generated power, from the offshore wind farms or the surplus active power of onshore AC grids, need to be transmitted and shared among different onshore AC grids based on a certain desired share. The desired shares are predefined in order to fulfill various objectives such as increasing the penetration of renewable energy sources, supporting the grid frequency and grid energy adequacy, and loss minimization. Regardless of the system configuration and topology, power sharing control should be performed without violating the system limits (e.g. voltage operating region, line current capacity and VSC power rating etc.). Furthermore, improved dynamic performance and system stability are needed. Importantly, the system is a nonlinear system, where the dynamic performance and stability margin change depending on the change in the system operating conditions. In case of an occurrence of a permanent outage in one of the inversion mode grid side converters, which produces power imbalance and voltage instability in the HVDC grid, the system must continue to operate in order to deliver power to the non-faulted terminals. The effects of that outage should be cleared in order to achieve a proper stable operation in the remaining system. To fulfill these requirement, the research objectives of this work are:

1. Achieving Accurate power sharing based on pre-defined desired-sharing schemes while consider the DC voltage transient and steady-state dynamics.
2. Improving the system stability and dynamic performances by increasing the system bandwidth at acceptable damping.
3. Mitigating the effects of the onshore converter outage occurrence especially the permanent outage and recover the system to the pre-outage state.

1.3.2 Contributions

To achieve the research objectives, a central supervisory control strategy is proposed to achieve the first two main objectives in normal operation:

1. Develop a novel power-sharing control strategy that utilizes an adaptive voltage-droop scheme, in which the voltage-droop parameters are optimally selected as a means of achieving accurate power sharing based on the desired shares. These shares

are optimized in advance by the system operator in order to fulfill the active power requirements of the connected AC grids. Furthermore, the DC voltage dynamics, including transient and steady-state performance, are considered when adapting the droop parameters.

2. Develop a new tuning methodology for selecting the optimum local controller parameters of the VSCs in an offshore MT HVDC network to mitigate the effects of changes in the operating conditions on the transient performance and the small-signal stability of the system.

   However, in some abnormal cases when the onshore output converters operate at their maximum capacity and lose the ability of regulating the DC voltage, which may happen in the case of a converter outage, the proposed supervisory controller cannot control the system alone and prevent the system collapse, thus the third contribution has been performed, which is:

3. Develop a new control strategy to mitigate DC overvoltage effects without producing oscillations in the DC voltage and the wind power generation in case of permanent outage in an onshore VSCs, which can be used in temporary fault/outage ride through control as well.

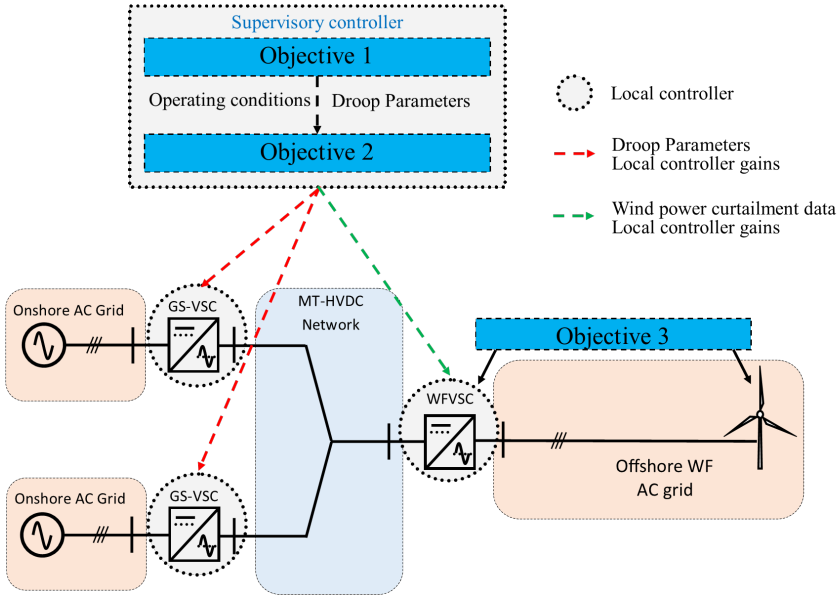

Figure 1.3: Thesis Objectives

1.4 Thesis Organization

The remainder of this thesis is organized as follows:

Chapter 2 provides background and a survey of the literature related to the operation and control of MT VSC-HVDC based wind farms integration system.

Chapter 3 presents the transient and steady-state mathematical modeling of the system that are used in the next chapters.

Chapter 4 introduces the proposed power sharing control strategy of multi-terminal VSC-HVDC transmission systems utilizing adaptive voltage droop.

Chapter 5 illustrates the proposed VSCs local controller gains tuning methodology for MT HVDC VSCs based offshore wind farms integration systems.

Chapter 6 introduces the proposed DC voltage control during permanent converter-outages for power flow continuity in offshore multi-terminal VSC-HVDC systems.

Chapter 7 presents the thesis conclusions and contributions.

Chapter 2

Background and Literature Survey

This chapter provides a general overview of MT VSC-HVDC systems with the aim of explaining their history and evolution. First of all, the concept of the multi-terminal HVDC system and its need is presented, together with its advantages with respect to the common AC grids. Secondarily, the main HVDC converter technologies are described and the main advantages and drawbacks of each of them are briefly discussed. Finally, a general state-of-the-art is explained and an introduction to dc networks topologies is done.

2.1 Introduction

A multi-terminal VSC-HVDC transmission system is the interconnection of more than two VSC stations via DC cables in different topologies, e.g., radial, ring and meshed. It is the evolution of traditional two terminals (point-to-point) HVDC transmission systems. The MT HVDC system provides the ability to connect multiple AC grids, remote power plant and remote loads together. This transmission system is considered a promising technology for the integration of massive generation from renewable sources into the power system. Furthermore, it can be used to trade the electric power safely across national borders.

2.2 Multi-Terminal HVDC System Components

The main components of HVDC network are the converter stations and HVDC transmission lines.

2.2.1 HVDC VSC converter Station

The converter stations are used to connect the HVDC transmission network with other grids, e.g., AC grids, DC grids, remote power plants. There are two types of HVDC converter station based on the type of connected grid: AC-DC converter to interface with AC grids and bidirectional DC-DC converter to interface with other DC grids with different voltage level and configuration. The commonly used converter station in MT HVDC networks is based on AC-DC VSC. The VSCs work in two modes of operation: rectification mode (AC to DC conversion) when the power flows from the AC side to the DC side, and inversion mode (DC to AC conversion) as the power flows from the DC to the AC side.

The main components of the VSC station are the converter, the phase reactor, the AC filter and the DC capacitor as shown in Fig. 2.1. On the AC side of the converter, the converter is connected to the AC grid through a three-phase reactor, shunt low-pass filter and transformer. On the other hand, the DC network is connected to the converter through DC smoothing capacitors and high frequency filters.

AC-DC converters

As a result of the development of the fully controlled semiconductor technologies, the VSC has been promoted to reach important voltage levels. The VSC consists of IGBTs and diodes. The IGBTs are fully controlled devices that conduct the current in one direction. Therefore, a diode is connected in anti-parallel to enable current conduction in the opposite direction. The VSCs operate at a switching frequency of more than 1 kHz to eliminate low order harmonics. Thereby, a filter is required only to high order harmonics that is significantly smaller in size than the LCC smoothing filter.

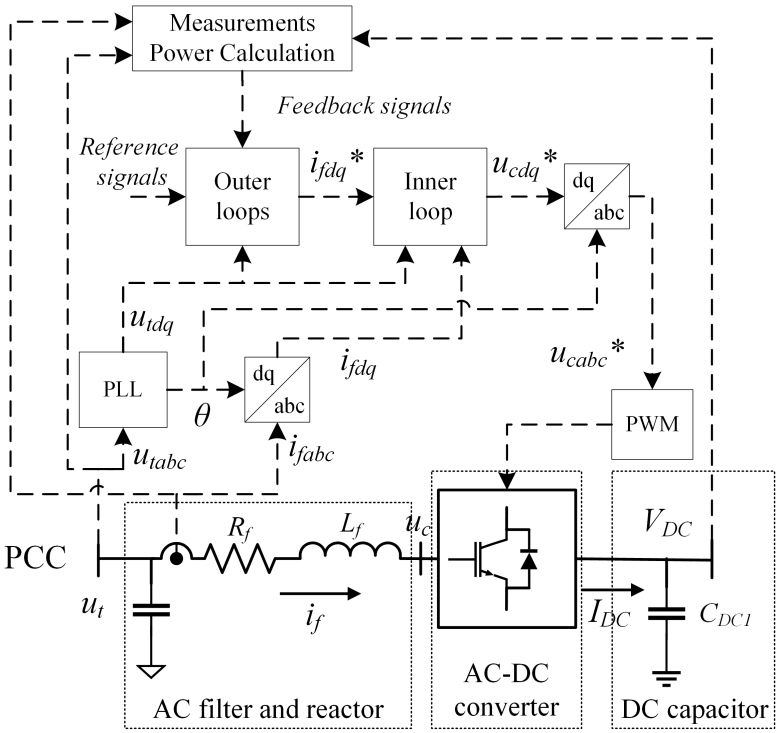

Figure 2.1: HVDC components and control structure

Phase reactor and the low-pass filter

The phase reactor is part of low pass filter; it has high inductance with low resistance. The reactor is one of the main components that affects the active and reactive power control. The shunt low-pass filter prevents the output high frequency harmonics of the converter from entering the AC grid.

DC capacitors

The DC capacitor is used to smooth the DC voltage at the terminals of the converter by keeping it within a small range via charging and discharging. It is used also as an energy storage unit. It has a dominant effect on the voltage and power dynamics in the DC network.

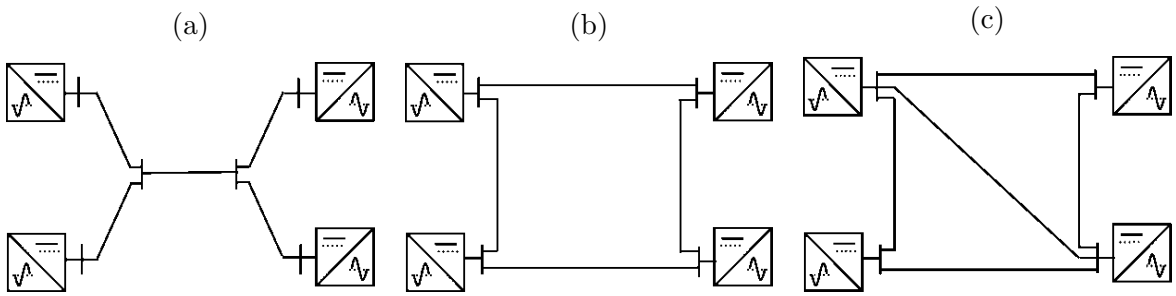

Figure 2.2: MT-HVDC topologies (a) Radial (b) Ring (c) Meshed

2.2.2 HVDC transmission lines

The multi-terminal HVDC transmission lines has two configurations: unipolar (2 terminals) or bipolar (three terminals). There are many topologies such as radial, ring, or meshed topologies as shown in Fig. 2.2. The selection of the topology depends on a number of factors. One of these factors is the economic consideration that depends on cable length and ratings, geographic nature of the cable path, the number and the ratings of protection devices, etc. In addition to the economics, the technical aspects such as the system reliability, flexibility and efficiency need to be taken into account [3],[4]. As concluded in [14], the radial topology has the lowest cost and transient short circuit fault current, but it also has lower reliability and efficiency in comparison to the other topologies. On the other hand, the meshed topology is more reliable and has lower transmission loss; however, it is more expensive.

2.3 Multi-terminal VSC-HVDC Control Structure

In the MT-HVDC system, the system converters control their local variables through their local controllers based on desired set-points and control parameters. These set-points and control parameters are calculated and then sent by a central controller to the system converters for achieving global objectives of the overall systems. Thereby, the MT-HVDC transmission network control system has a two-levels hierarchal structure. The two levels of the control systems are the primary and the secondary control levels, as shown in Fig. 2.3.

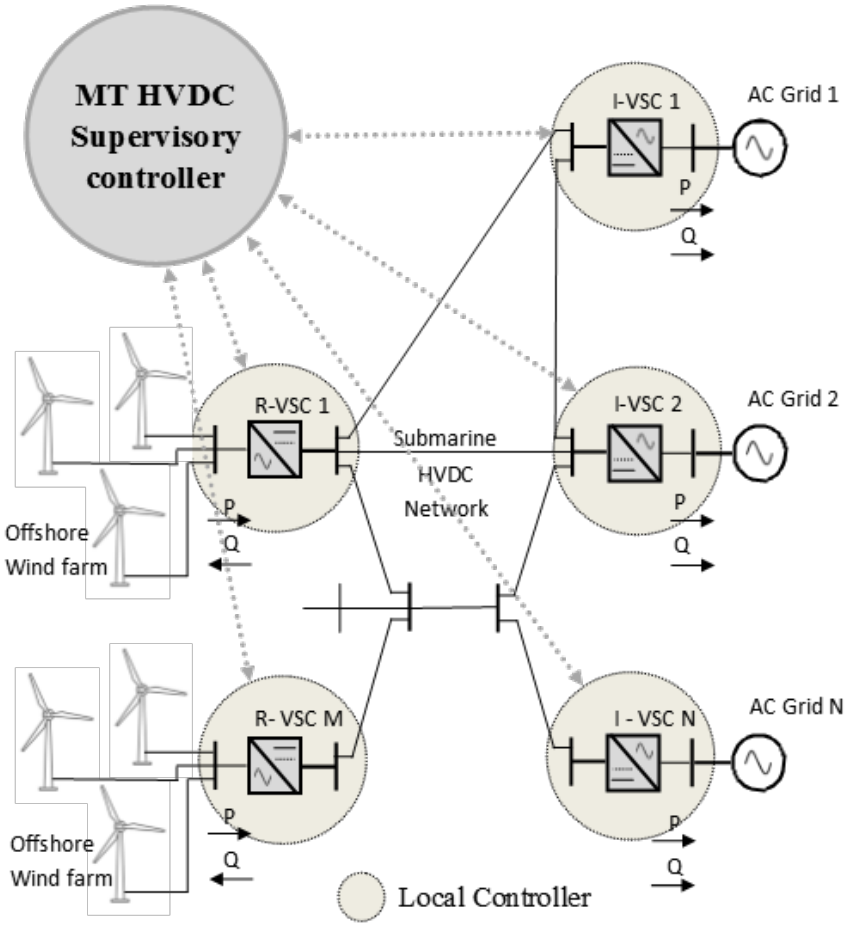

Figure 2.3: VSC-HVDC control structure

2.3.1 Primary control level

The primary control level is the local controller of the VSC stations, the purpose of this controller is controlling the local variables of the VSC, such as the AC filter reactor current, terminals AC voltage, terminal DC voltage, active and reactive power. Decoupled dq - current control technique is the commonly used technique in VSC controllers. This technique provides the possibility to control the two components of the AC current, i.e., the direct (real) and quadratic (imaginary) components, independently [15]. The local controller consists of a number of cascaded control loops. The main control loop is the

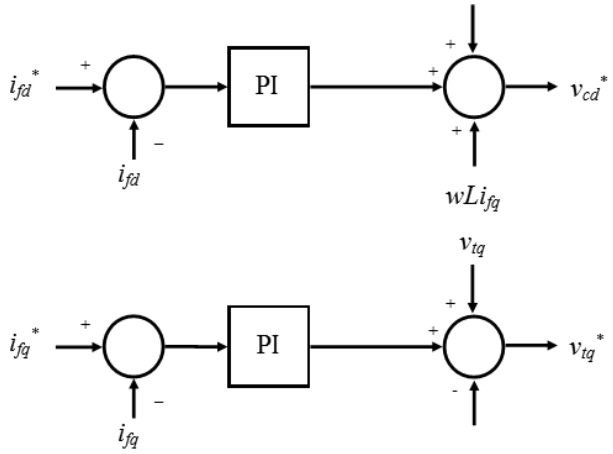

Figure 2.4: Inner decoupled-current control loops

inner current loop, which controls the AC reactor current. the reference current values are calculated by the outer loops, which define the VSC mode of operation [7],[16], [16], [17].

Inner control loops

The inner loop is based on a PI controller that is responsible for controlling the decoupled current components of the filter reactor, i_{f_d} and i_{f_q}. these two current components are controlled by generating the reference voltages $u^*_{c_d}$ and $u^*_{c_q}$, in dq frame, of the converter. The reference current signals $i^*_{f_d}$ and $i^*_{f_q}$ are generated from the outer loop which will be explained later. A feed forward signal for the PCC voltage is used to fully decouple the VSC's inner control loop dynamics from those of the load. Fig. 2.4 illustrate the implementation of inner current control loop.

Phase locked loop

The phase locked loop (PLL) is used to synchronize the VSC to the AC grid by making sure that the d-axis is always aligned with the terminal voltage phase a. This process is performed by controlling the VSC frequency and the transformation angle θ_{pll}, which is used in the transformation from abc to dqo frames and vice versa, to make the q component of the terminal voltage always zero. In addition, the PLL is used to measure the connected

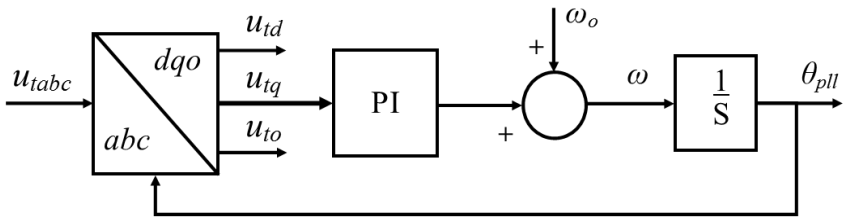

Figure 2.5: Inner decoupled-current control loops

AC grid frequency [18], [19]. The implementation of the PLL that is used in this work is shown in Fig. 2.5.

2.3.2 Outer control loops

The outer loop is the part in the VSC local controller that defines the mode of operation of the converter. It produces the reference decoupled currents $i^*_{f_d}$ and $i^*_{f_q}$ for the inner loop, so that it is possible to control two different variables independently. As shown in Fig. 2.6, in grid-imposed frequency VSCs, the active power or the DC voltage are controlled by controlling the d-axis current component. On the other hand, the reactive power or the AC voltage at the point of common coupling (PCC) are controlled by controlling the q-axis current component [20]. For the grid-imposed frequency, there are four possible modes, P-Q, P-Vac, Vdc-Q and Vdc-Vac. While, in the frequency controlled VSC, as in the WF VSC, the outer loops are responsible for controlling the dq components of the voltage at the PCC, Fig. 2.7 shows the outer control loop of the WF VSC [18].

2.3.3 Droop control in DC grids

In AC systems, the synchronous generators control their output active power by means of power frequency droop characteristics. By increasing the system demand, the system frequency decreases, which in turn makes the output active power of the synchronous generator increase, and vice versa. On the other hand, reactive power voltage droop controls the system voltage by delivering reactive power to the system. In the DC grid, the DC voltage level and the Active power at any bus are correlated, while, the DC voltage and

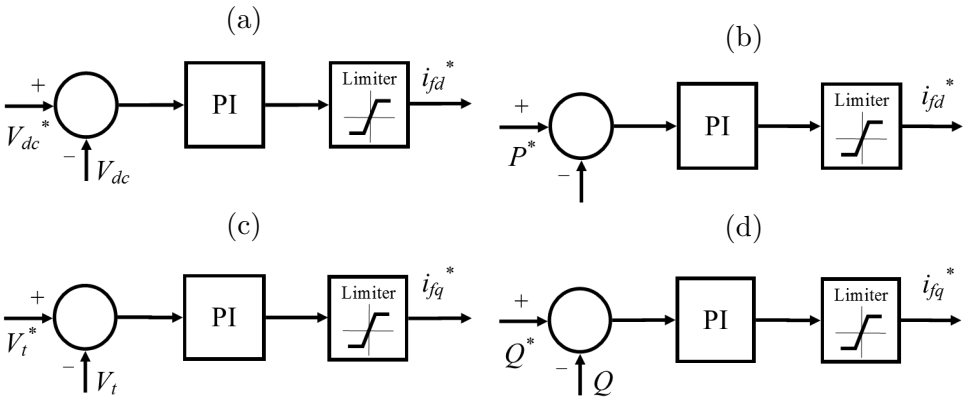

Figure 2.6: Outer control loops of the grid connected VSC (a) DC voltage controller, (b) Active power controller, (c) AC voltage controller, (d) reactive power controller

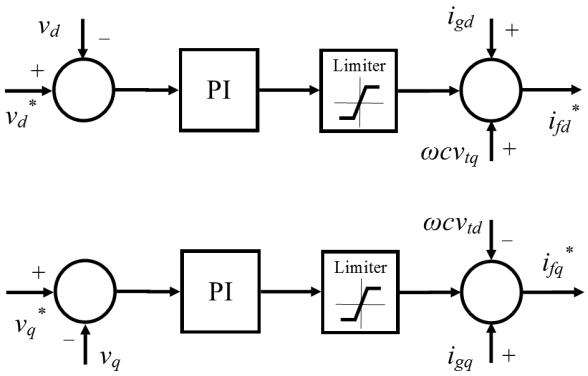

Figure 2.7: Outer control loop of the WF VSC.

the active power are directly controlled by controlling the d-axis AC current component, it is not possible to directly control both of them simultaneously. Therefore, as in AC grid, the frequency and the active power can be controlled by means of droop control concept. In the DC grid, the DC voltage and the active power can be controlled simultaneously by means of V-I or V-P droop control, see Fig. 2.8 [21], [22], [23]. In this work, DC voltage-current droop is used. Hence, the reference value of the DC voltage controller is calculated by (2.1), or the reference value of the active power outer control loop is calculated by (2.3),

as follows:

$$V^*_{dc_i} = V_{o_i} + R_{D_i} I_{dc_i} \tag{2.1}$$

where V_o is the converter DC voltage at no load, R_D the current based voltage droop gain, V_{dc} is the DC voltage reference value of the i^th VSC terminals and I_{dc} is the measured DC current input of the i^th VSC.

$$I^*_{dc_i} = \frac{1}{R_{D_i}}(V_{dc_i} - V_{o_i}) \tag{2.2}$$

$$P^*_i = I^*_{dc} V_{dc} = \frac{V_{dc_i}}{R_{D_i}}(V_{dc_i} - V_{o_i}) \tag{2.3}$$

where V_{dc_i} is the measured DC voltage at the i^th VSC.

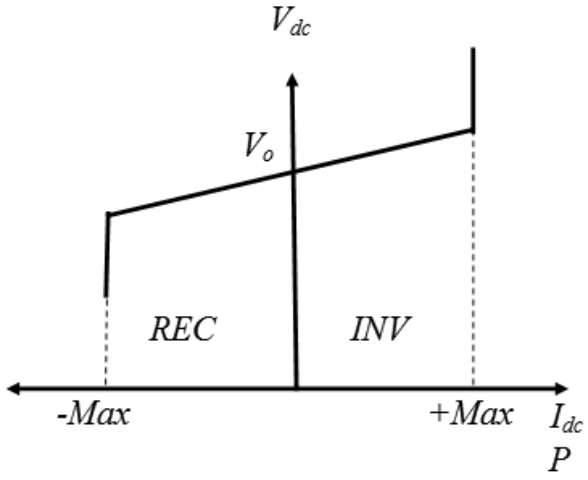

Figure 2.8: Droop characteristics in DC grids

2.3.4 The secondary (supervisory) control level

The supervisory control level of a MT HVDC transmission system is responsible for calculating the control parameters and set-points of the system VSCs' local controller to achieve certain transient and steady-state operation objectives. The supervisory control levels can be based on centralized controller that receives the measurement data from the

local controllers, then calculates the required control parameters and set-points and then sends them back to the local controllers. Otherwise, distributed control concept can be used on the supervisory level to increase the system reliability, in which the system VSCs share some common data, i.e., measurements and set-points, and locally calculate their local control parameters and set-points.

In this work, the main objective of the supervisory controller is to calculates and tune the optimal control parameters for power sharing control and the DC voltage regulation process and enhancing the transient responses of the local controllers.

2.4 Power Sharing Control and DC Voltage Regulation in MT VSC-HVDC Network

One of the main applications of the MT VSC-HVDC transmission system is the integration of offshore wind farms. In this application, MT HVDC system transfers the power generated from the offshore wind farms to onshore AC grids, in addition to the power trade between the different grids. The imported power to the MT HVDC system is shared among AC grid in a certain scheme while keeping the DC voltage at the system buses within a certain range. This power sharing scheme depends on many objectives such as minimizing the transmission losses, sharing ratio or priority order.

There are multiple techniques performing the operation of power sharing control and the voltage regulation [24][32]. These techniques can be classified into 2 main categories: Master-Slave techniques and Distributed DC voltage control techniques. Each of these categories is divided into centralized and decentralized control strategies.

2.4.1 Master-slave techniques.

In the master-slave method, one converter is responsible for DC voltage regulation, while the other converters work in constant control mode. The DC voltage is regulated by the master converter using the direct DC voltage control outer loop. The other converters (the slaves) control the power flow in the system by working in constant power mode. The

reference power settings of these converters are calculated through an optimal power flow algorithm in a centralized location, usually in the master converter station, to perform a certain power sharing scheme. To insure the power sharing accuracy and the active power balance, high speed communication is needed between the centralized controller and the local controllers. The DC voltage reference value in the master converter is defined to prevent system voltages from violating system limits [25]. An OPF algorithm is one of the algorithms used for achieving certain objectives such as minimum transmission losses without violating the limits. This method provides accurate power sharing; however, it has many drawbacks such as: the need for fast communication, the master converter holds all power fluctuations in the system, it is difficult to regulate the voltage in large networks through one converter, and it cannot provide good reliability due to a single voltage regulator [22].

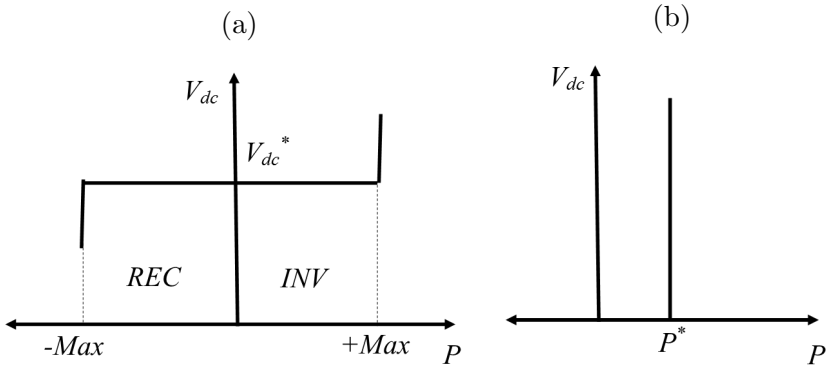

Figure 2.9: P-V characteristics of (a) the master converter and (b) the slaves.

In [26], the authors propose an operation planning algorithm based on an observer-based management system (OBMS). The Multi-terminal HVDC system in this work is a master-slave configuration with a single slack bus in the DC network, but the position of this slack bus is not fixed. The algorithm determines the optimal location of the slack bus and optimal settings of the other power controlled converters based on the energy marked schedules in the AC grids connected to the HVDC network. The main drawbacks of the previous algorithm are: the difficulty in regulating the voltage in large systems and the existence of one converter to regulate the voltage which reduces the reliability of the

system.

To reduce dependency on fast communication and increase system reliability, decentralized control strategies such as the voltage margin method (VMM) and fixed voltage-droop-based methods have been proposed. VMM is a modified version of the master-slave method whereby the voltage control operation is rotated in turn among different converters based on their local voltage and power levels [27], [24]. The main drawback of this method is the high amount of voltage oscillation resulting from hunting dynamics of the master transfer [28], [29]. The modified VMM proposed in [28] combines the Vdc-P droop relation and the voltage margin; the purpose of the droop is to reduce the hunting dynamics and the oscillation.

To increase the system reliability, a fixed-decentralized voltage-droop based method is proposed, inspired by the power-frequency droop in AC systems, voltage regulation is distributed among a number of converters, with the active power being shared based on their droop characteristics. However, high accuracy of power sharing cannot be guaranteed because the output power sharing changes with the changing in the DC voltage level at the system buses due to the wind power fluctuation, hence the droop parameters need to be updated [30].

2.4.2 Distributed DC voltage control techniques

To increase power-sharing accuracy, distributed voltage control methods are used, such as distributed direct voltage or adaptive droop-based control. The responsibility for voltage control is distributed among a number of converters by means of direct voltage control or droop-based control. The control parameters and set-points are periodically computed in a centralized controller and are then sent to different converters via low-speed communication.

Distributed direct DC voltage control Methods

The distributed direct voltage control, DVC, is proposed in [15][13], [31][36], [32][37]. these studies employ a loss minimization OPF algorithm, which determines the voltage set-points of direct-voltage-controlled converters. The OPF is performed in every control cycle, which

could be a matter of minutes, so the existence of fast communication is not needed. An N-1 contingency analysis is performed within the OPF to provide N-1 security to the system and make it operate during the outage of one of the DC voltage controlled converters. However, due to line resistances, the accuracy of the power sharing and the optimality of the loss minimization are affected by variations in wind power generation, especially when these variations are faster than the cycle for updating the voltage reference set-points. In addition, the voltage deviation and power sharing that occur after a converter outage are very sensitive to line resistances, and if communication is lost over a long period, the system stability will be affected, and the system voltage may violate recommended limits.

Adaptive droop based DC voltage and power sharing control

Because it provides droop-control stability in case of the communication loss, an adaptive voltage-droop method is used for overcoming the disadvantages of the DVC technique. The virtual resistance of the droop gain also reduces the sensitivity of the power sharing to line resistances so that the accuracy of the power sharing is increased. In the adaptive droop based methods, the parameters of the droop controllers are adapted to achieve different operation objectives. The work in [33] presents a methodology to calculate the droop gain of the droop based converter. This methodology uses circuit analysis technique to minimum transmission power losses in wind farm integration multi-terminal HVDC system. The main drawback of this methodology is the difficulty of applying it to meshed or ring topology systems. [34] uses the same technique that is used in [33] but the objective of this methodology is calculating the droop gains, at constant no-load voltage, in order to achieve a certain power sharing ratio between them. Also, this algorithm cannot be applied on large meshed or ring topology networks. The techniques used in [35] and [35] can work in a decentralized operation. However, the accuracy of the power sharing will change based on the change in the active power generation due to the network line resistances.

By increasing the system voltage to minimize the transmission losses, the converter losses, which are proportional to the operating voltages, will increase. The work in [36] presents an OPF algorithm that selects the optimum reference voltages of the droop based converters in the system, while making the droop gain fixed, in order to minimize the total losses of the system, which is the summation of transmission losses and the internal

converter losses. However, loss minimization as a power-sharing objective might not achieve desired power share preferences of each connected AC grid. These preferences can be supporting energy adequacy, increasing wind energy penetration, or maximizing converter loadability. An additional factor is that droop gain values affect both DC voltage dynamics and the accuracy of the power sharing [21], [20]. Despite these considerations, previous researchers did not take into account DC voltage transient dynamics in their power-sharing control algorithms. Although the authors of [21], [23], and [37] proposed methodologies for selecting droop gains considering the DC voltage dynamics. Their methods relied on the calculation of a factor to be multiplied by all droop gains predetermined from power-sharing control algorithms, in order to achieve optimal DC voltage dynamics without the violation of any constraints. Such methods could affect the accuracy of the power-sharing control. According to the available headroom of each converter station, the algorithm proposed in [38] adapts the droop gains, which is preselected with respect to the converter rating not from a power-sharing control algorithm, to share the burden after a converter outage considering the system stability. Without considering the power-sharing control, the droop parameters are optimized in order to not compromise the AC system stability after a converter outage and abrupt power set-points changing [39]. At the DC micro-grid level, an improved droop control for load current sharing of distributed generators (DGs) is proposed in [40]. This droop control improvement aims at increasing the accuracy of the load current sharing by modifying the droop controller reference voltage as a function of the average DC voltage and current, which are broadcasted among the DGs using low-bandwidth communication, while keeping the droop gains fixed.

2.5 Multi-terminal HVDC Small-Signal Stability Analysis And Control

This section presents a literature survey on the small signal stability analysis of VSC based multi-terminal HCVD, based on the linearized state space model derivation of the system. Then, a survey on the damping controller design and its parameters tuning is performed.

2.5.1 Small-signal stability analysis of a nonlinear system

Small signal stability analysis is applied to a system to study its stability in case of the application of small disturbances. The oscillation nature of the system variables after small disturbances submission determines the system stability. If this oscillation is small and damped the system is considered stable. Otherwise, the system is unstable if the oscillation diverges.

The commonly used tool to study the small signal stability of a nonlinear system is the Lyapunov linearization method. This method is based on the analysis of the eigenvalues of the linearized state space model approximation of the nonlinear system. By the analysis of the eigenvalues, the stability of the system can be judged; if all eigenvalues of the linearized approximation of the system have negative nonzero real part, the nonlinear system is considered stable around the equilibrium point. On the other hand, if one or more of these eigenvalues have positive real part, the linear system is unstable. For the critically stable linearized system, the nonlinear system stability status cannot be concluded. Due to the nonlinearity of the Multi-terminal HVDC system, its stability is affected by the operating point and the system components parameters [41].

In order to perform the small signal stability study using the Lyapunov linear method, a linearized state space model of the Multi-terminal VSC-HVDC was derived in a number of literature studies with different assumptions and configurations [21], [16], [17], [42], [43], [44]. The linearized state-space model is the aggregation of the system components linearized model, such as the VSCs, the DC network lines, the wind generators and AC grid.

The linearized state space model of a nonlinear system is in the form of:

$$\Delta \dot{\boldsymbol{x}} = \boldsymbol{A}\ \Delta \boldsymbol{x} + \boldsymbol{B}\ \Delta \boldsymbol{u} \tag{2.4}$$

$$\Delta \boldsymbol{Y} = \boldsymbol{C}\ \Delta \boldsymbol{x} + \boldsymbol{D}\ \Delta \boldsymbol{U} \tag{2.5}$$

where $\boldsymbol{A}$, $\boldsymbol{B}$, $\boldsymbol{C}$ and $\boldsymbol{D}$ are the system matrices; $\boldsymbol{x}$ is the state variable vector, which is the vector aggregating all system components state variables. The system inputs such as the reference set points signals, the wind speed and the load values.

Modal analysis of a linear system

The modal analysis is a methodology used to analyze the stability of a liner system by finding the eigenvalues. Using the sensitivity analysis, degree of the effectiveness of matrix A elements; hence, the system parameters and operating points, on a certain eigenvalue can be determined. Furthermore, the participation analysis can determine the degree of participation of the eigenvalues on a certain state variable.

Modes, eigenvalues and eigenvectors

The eigenvalues of a linear system can be calculated by (2.6)

$$\det\left(\boldsymbol{A}-\boldsymbol{\lambda I}\right)\ =0 \tag{2.6}$$

where λ is a vector of eigenvalues and $\boldsymbol{I}$ is the unity matrix. For any eigenvalue λ_i there are two nonzero eigenvectors l_i (the i^{th} left eigenvectors) and r_i (the i^{th} right eigenvector) such that

$$\boldsymbol{A}\boldsymbol{r}_i\ =\ \boldsymbol{\lambda}_i\ \boldsymbol{r}_i,\quad \forall i=1,2,3,\ldots,n_\lambda. \tag{2.7}$$

and

$$\boldsymbol{A}\boldsymbol{l}_i^T\ =\ \boldsymbol{\lambda}_i\ \boldsymbol{l}_i,\quad \forall i=1,2,3,...,n_\lambda. \tag{2.8}$$

where n_λ is the dimension of $\boldsymbol{A}$ and hence, the number of eigenvalues.

The modal analysis of a linear system is based on three n_λ-dimensional matrices called modal matrices.

$\boldsymbol{\Lambda}=diag\{\lambda_1,\lambda_2,\lambda_3,\ldots,\lambda_{n_\lambda}\}$

$\boldsymbol{X}_R=[\boldsymbol{r}_1,\boldsymbol{r}_2,\boldsymbol{r}_3,\ldots,\boldsymbol{r}_{n_\lambda}]$

$\boldsymbol{X}_L=[\boldsymbol{l}_1,\boldsymbol{l}_2,\boldsymbol{l}_3,\ldots,\boldsymbol{l}_{n_\lambda}]$

The modes of the system are the state variables of the system after linearization. The relation between the mode and the linearized state variable of the system is presented in (2.9) and (2.10).

$$\Delta\mathbf{x}\left(t\right)=\mathbf{X}_R.\boldsymbol{z}(t) \tag{2.9}$$

$$\boldsymbol{z}\,(t) = \mathbf{X}_L.\Delta\mathbf{x}\,(t) \tag{2.10}$$

Sensitivity analysis

The sensitivity analysis measures the degree of the effectiveness of an element in A matrix on a certain eigenvalue; hence, the effects of a certain system parameter on eigenvalues can be determined. The sensitivity factor of an element a_{kj} on an eigenvalue λ_i can be found by (2.11)

$$\frac{\partial \lambda_i}{\partial a_{kj}} = l_{ki}\ r_{ji} \tag{2.11}$$

where, r_{ji} is the j^{th} element in r_i and l_{ki} is the k^{th} element in l_i.

Participation factor analysis

To find the participation degree of an eigenvalue in the dynamic response of a certain state variable, a factor called the participation factor is calculated using (2.13) to measure this degree of participation. Equation (2.12) illustrates the relationship between a state variable $\Delta x_k(t)$ and the system eigenvalues.

$$\Delta x_k(t) = \sum_{i=1}^{n} p_{ki}\lambda_i \tag{2.12}$$

where, p_{ki} is the participation factor of i^{th} eigenvalue in the k^{th} state variable.

$$p_{ki} = r_{ki}\ l_{ki} \tag{2.13}$$

where, r_{ki} is the k^{th} element in r_i and l_{ki} is the k^{th} element in l_i

2.5.2 Small-signal stability analysis of MT VSC-HVDC linearized state space model

Many stability studies were performed on point-to-point VSC-HVDC systems [45], [46], [47]. However, for MT VSC-HVDC, linearized models of distributed direct voltage controlled MT VSC-HVDC are derived in detail in [17] and [16]. In [17] all converters are

connected to AC grids that are considered stiff grids for simplicity. Small signal stability analysis is applied to a two-terminal and three-terminal VSC-HVDC network to study the effect of changing the active power set point on the system stability through the eigenvalues analysis. In addition, a study on the effect of the DC voltage PI controller parameter was performed. [16] derived a linearized state space model for a MT VSC-HVDC transmission system. This system consists of wind farms based on fixed speed induction generators. These wind farms are connected to an AC grid containing a synchronous machine through a MT VSC-HVDC network. In the HVDC network there are two wind farm VSC stations and two grid side VSC stations acting as two connecting points to the AC grid. A small signal stability study on a base-case scenario was carried out. The author found that the states of the synchronous machine influence the eigenvalues that dominate the response of the system; hence, to achieve good damping performance the synchronous machine controller should be taken into account. Furthermore, by proper design of the VSC control parameters, fast damping of the super-synchronous oscillation can be achieved. Studies of the VSC control parameters for both wind farm and grid side converters were accomplished. However, in [16] the authors didn't consider the dynamics of the DC network lines and the AC grid line impedance. The authors of [43] performed a small signal stability analysis on the active power control of a MT VSC-HVDC system in different mode of operation: centralized DC voltage control and droop control modes. The study aimed to identify the interaction and local modes of the different converters in the system. In addition, a more detailed model of DC cables with termination inductors was considered.

2.5.3 MT-HVDC VSC local controller parameters tuning

The commonly used control scheme in HVDC VSCs local controller is that based on the dq-decoupled current control. The dynamic model of the VSC converter based on this control scheme is explained in detail in chapter 3, which is divided into two control stages: the inner (current) control loop and the outer control loop that is responsible for defining the VSC operating modes. There are other control schemes with different assumption and structures as compared to those presented in [48], [15], [49][26], [50] and [51].

The local controller parameters (gains) need to be tuned to improve the transient response of the system. Due to the cascaded structure of the decoupled current control

scheme, the response of the inner loop needs to be much faster, therefore, its gains need to be tuned for that purpose. However, the stability enhancement and error cancellation are achieved by proper tuning of the outer loop controller parameters [52]. The authors of [52] and [53] state two methods used in tuning the local controller parameters: Modulus Optimum criterion and Symmetrical Optimum condition methods. The simplicity and fast response of Modulus Optimum make it suitable for tuning the inner loop parameters. This method is based on cancellation of the dominant (largest) time constant of the plant, while keeping the closed loop gain higher than unity (by performing pole placement). On the other hand, the Symmetrical Optimum criterion is used to tune the outer loop gains; it is suitable for the systems that have one or more poles near or at the origin, where pole placement is not effective. In [53] the most probable location of the dominant poles, which is used to tune a simplified control structure of the VSC-HVDC system. The simplified model depends on the system transfer function type (type 1 or type 2) and the parameters will be functions of reactor parameters, switching frequency, PWM gain, damping ratio and frequency. Other tuning technique based on particle swarm optimization algorithm PSO was performed in [54]. The PSO algorithm is used to select the optimum settings for the controller parameters of a point-to-point VSC-HVDC system to minimize the system error function that is the summation of the errors in the VSC control variable, which are DC and AC voltages, and the dq currents. The work in [55] was carried out to achieve a robust controller, by selecting the optimum PI control parameters by genetic algorithm optimization in order to minimize the standard infinite time quadratic performance index.

All previously mentioned tuning techniques were used to tune VSCs PI controller parameters in the system that contains a single VSC or in a conventional point-to-point HVDC link. Furthermore, the effect of the DC line was not taken into consideration; only the effects of the DC capacitor and the AC reactor (filter) were considered. In a multi-terminal VSC-HVDC network, multiple converters are responsible for controlling the DC voltage and the active power. Therefore, achieving optimal transient response through tuning the controller of each converter separately is difficult due to the interaction between the network converters.

2.6 DC Voltage Control During a Permanent Grid Side Converter Outage

Point-to-point HVDC links or MT HVDC networks isolate the offshore WF AC grids from the effects of onshore AC grid faults, which leads to temporary or permanent outages the onshore converters. This isolation results in the continuation of wind power generation by the wind turbines at the pre-fault operating level. If the onshore HVDC converters that receive the offshore wind power generation operate close to the maximum power capacity, they will be unable to absorb the active power of the disconnected onshore converter. In such cases, all onshore converters, which are responsible for regulating the DC voltage, operate at their rated power (i.e., in constant power control mode) and lose their ability to regulate the DC voltage. As a result, an overvoltage occurs, triggering protection devices and possibly leading to system collapse. For these reasons, the literature includes reports of numerous fault-ride-through (FRT) control strategies that have been proposed in order to provide a system with FRT capabilities. Some of these FRT control strategies are already being used in point-to-point HVDC links, as summarized in the following subsections.

2.6.1 Fast excess power absorption strategies

In these strategies, the mitigation of DC overvoltages effects that occur due to power imbalances in an HVDC network is achieved through the absorption of the excess power in the form of dissipated power in braking resistors though a DC chopper or through stored energy in energy storage systems. The DC chopper method, which is commonly used in conventional point-to-point HVDC transmission, requires simple control rules for triggering the DC chopper if the DC voltage exceeds a specified threshold value [56], [57], [58]. The authors of [59] proposed a method for absorbing the excess power after a converter outage with the use of a flywheel energy storage system (FESS). The primary advantage of these methods is that they are decentralized and need simpler control rules. However, additional fully rated equipment, e.g., an HVDC chopper plus a resistor for each power-receiving converter, or an HVDC VSC-driven FESS are needed. Furthermore, the thermal capacity of the resistance or the storage capacity limit their power absorption capability.

2.6.2 Communication-based strategy

In this control approach, communication links are employed to send fast wind power reduction signals from the centralized controller of the HVDC system to each individual wind generator in the connected WFs [60],[61], [62]. This method requires a fast communication infrastructure because the response of the FRT control action is limited by the communication speed. Furthermore, the extra cost of the communication links must also be considered [63].

2.6.3 Decentralized fast wind power reduction strategies

These types of FRT control strategies are decentralized and entail no requirement for additional hardware. To achieve a fast reduction in wind power, they use the WF-VSCs for reducing the AC voltage level of the WF grid as a means of emulating a short circuit fault in the offshore grid, or of raising the frequency that accompanies a rise in the DC voltage due to a power imbalance in the DC links. The authors of [64] employed this type of action for reducing electromagnetic wind power generation. However, this method can be used only with wind turbines based on an induction generator, e.g., a doubly fed induction generator (DFIG). The FRT control strategies proposed in [63] and [57] involve the same actions, i.e., a drop in the AC voltage or a rise in the frequency, in order to trigger the FRT rules for controlling DFIG and permanent-magnet-synchronous generator (PMSG) wind turbines. With respect to DFIGs, an AC voltage-level drop or a frequency rise reduces the electromagnetic wind power generation incorporated with the FRT controller proposed in [65] and [66] in order to limit inrush currents by restricting the rotor current. In a PMSG controller, under specific conditions, the voltage or the frequency signals trigger the FRT rules, as proposed in [67], [68].

2.6.4 Permanent GS-VSC outage scenario

The previously mentioned FRT control strategies were originally proposed for point-to-point HVDC links in order to mitigate the effects of a temporary AC fault, in a connected onshore AC grid, which leads to a temporary outage of the power-receiving VSC, i.e., a

grid-side VSC (GS-VSC). These strategies were also applied on MT HVDC systems by the authors of [57]. In the case of permanent or long-time onshore converter outages, point-to-point HVDC link must be turned off, and FRT strategies are therefore unnecessary. Nevertheless, in MT HVDC networks, the system must continue to operate in order to deliver power to the non-faulted terminals. The permanent or long-time onshore converter outage case scenarios in MT HVDC system were not studied in literature, and the previously proposed FRT control strategies for onshore AC grid faults were not tested on such scenarios. The use of power-absorption based FRT control strategies with permanent onshore converter outages is limited by the thermal capacity of the DC chopper resistance or by the storage capacity of the FESS. The fast wind power control strategies proposed in [65], [66], [67], and [69], which are based on wind generator FRT control, limit the wind generator current and power through on/off control and produce a high degree of oscillation in the wind power, the WF AC voltage, and the HVDC voltage, as revealed in the simulation results for those studies.

2.7 Discussion

Through the literature provided in this chapter, it is clear that adequate work has been performed with respect to power sharing control in MT VSC-HVDC transmission systems to meet certain power sharing schemes while regulating the system voltage. The reliable techniques, with acceptable accuracy, are distributed direct voltage control or DC voltage droop control. Neither method needs fast communication, while the droop based control systems are characterized by lower sensitivity to the variation in power generation and higher stability in case of communication loss. However, active power sharing control based on predefined desired sharing scheme is not covered in previous works. In addition, previous researchers did not take into account DC voltage transient dynamics when selecting the droop parameters in their proposed power-sharing control algorithms.

Furthermore, most of the literature dealing with VSCs local controller parameters tuning takes into consideration the VSC dynamic only, regardless of the system dynamics and the interactions between the system components, which therefore cannot guarantee optimum dynamic performance. In addition, due to the nonlinearity of the MT HVDC transmission system, any change in the system operating point affects the dynamic per-

formance and stability of the system. A few studies performed the tuning algorithm for the VSC controller parameters while also taking the dynamics of the system into consideration in point-to-point VSC-HVDC transmission link, or in MT HVDC system but with simplified VSC models, which do not include all parameters and control loops. The works that studied the small signal stability of the MT VSC-HVDC based offshore wind farms integration system did not take into consideration the dynamics of the DC grid lines.

While sufficient work has been done in the area of DC overvoltage control during a temporary converter outage, caused by an AC fault in the onshore grid, in offshore wind farm integration systems based on point-to-point HVDC transmission, few of them deal with MT VSC-HVDC networks. However, in the case of permanent or long-time onshore converter outages, point-to-point HVDC link must be turned off, and FRT strategies are therefore unnecessary. Nevertheless, in MT HVDC networks, the system must continue to operate in order to deliver power to the non-faulted terminals. The permanent or long-time onshore converter outage case scenarios in MT HVDC system were not studied in literature, and the previously proposed FRT control strategies for onshore AC grid faults were not tested on such scenarios. By performing an investigation on these cases. Using such strategies to deal with permanent VSC outages is either infeasible, such as with DC chopper and FESS methods, or produces large oscillations in the system variables, such as fast wind power reduction methods. These oscillations arise as a result of the use of discontinuous (on/off) control rules in the wind generators. Accordingly, a new communication-free DC overvoltage control strategy is needed to relief the effects of permanent onshore VSC outages in offshore MT HVDC systems by regulating the DC voltage of the HVDC network without producing oscillations in the system power and voltages.

Chapter 3

Multi-terminal VSC-HVDC Modelling

3.1 Introduction

In order to perform any transient or steady-state analysis on MT VSC-HVDC transmission systems, the electromechanical transient dynamics and steady state models of the system components should be clarified. In this chapter, the transient models of the MT VSC-HVDC system components and the DC network steady-state model are provided. These models are used in building the system simulation model, establishing a small signal state-space model that can be used in small signal stability studies in chapter 5, and tuning the converter control parameters. Furthermore, the steady-state models of the system components are important in building the power flow algorithms used in any voltage regulation and power sharing algorithm in chapter 5.

3.2 Dynamic Modeling of The MT VSC-HVDC System

In this section the dynamic equations of the system components, which describes the system dynamic performance, are provided. As explained in section 2.2, there are two main components of the MT HVDC system: the VSCs stations and the DC network. In case of a VSC is connected to a weak AC grid, the dynamic model of the connected Ac grid should be considered in the overall system modeling. Therefore, the dynamic differential equations of the overall system can be divided into three groups: the VSC, the AC grid and the DC grid. To simplify the process of building the state-space model of the system, the VSC AC filter capacitor equation is added to the AC grid model, and the VSC DC capacitor is added to the DC lines capacitors and their equation is added to the DC network model [17]. As shown in Fig. 3.1.

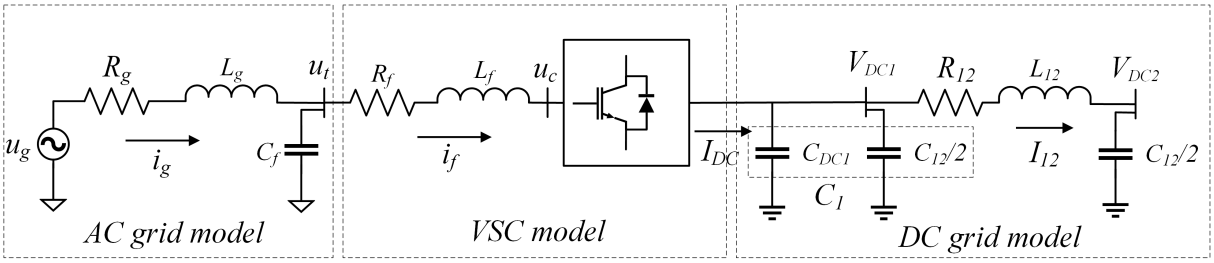

Figure 3.1: HVDC system components and models

3.2.1 Dynamic model of the system VSCs stations

In the MT VSC-HVDC transmission system, there two types of converters: grid side converters (GS VSC) and wind farm converters (WF VSC). All the VSCs in the system have the same inner control loops. However, their outer loops are different based on the mode of operation. In this work, all power input GS VSCs, i.e., rectifiers, operate in constant power control mode, all power output GS VSC, i.e., inverters, operate in droop control mode to regulate the DC voltage and control the power sharing. On the other hand, the WF VSC operates in AC voltage and frequency control mode.

The AC reactor model and the inner control loops

The inner loop is used to control the Ac reactor current dq components to achieve the set-points from the outer loops. Equations (3.1) and (3.2) are the dynamic equations of the AC reactor current dq components.

$$\frac{d}{dt}i_{f_d} = -\frac{R_f}{L_f}i_{f_d} + wi_{f_q} - \frac{1}{L_f}u_{c_d} + \frac{1}{L_f}u_{t_d} \tag{3.1}$$

$$\frac{d}{dt}i_{f_q} = -\frac{R_f}{L_f}i_{f_q} - wi_{f_d} - \frac{1}{L_f}u_{c_q} + \frac{1}{L_f}u_{t_q} \tag{3.2}$$

where R_f and L_f are the resistance and inductance of the phase reactor, u_{c_d} and u_{c_q} are the converter terminal voltage AC components in dq-frame, u_{t_d} and u_{t_q} are the d,q AC voltage components of the voltage at the PCC, i_{f_d} and i_{f_q} are Phase reactor current ac components in dq-frame, and ω is the AC grid frequency in rad/sec.

The dq current components are controlled by adjusting the reference converter voltage $u^*_{c_d}$ and $u^*_{c_q}$ by the inner loop PI controller, as shown in (3.3) to (3.6):

$$v^*_{c_d} = -K_{p_{in}}(i^*_{f_d} - i_{f_d}) - M_d + \omega L_f i_{f_q} + v_{t_d} \tag{3.3}$$

$$v^*_{c_q} = -K_{p_{in}}(i^*_{f_q} - i_{f_q}) - M_q - \omega L_f i_{f_d} + v_{t_q} \tag{3.4}$$

$$\frac{d}{dt}M_d = K_{i_{in}}(i^*_{f_d} - i_{f_d}) \tag{3.5}$$

$$\frac{d}{dt}M_q = K_{i_{in}}(i^*_{f_q} - i_{f_q}) \tag{3.6}$$

where $Kpin$ and K_{i_in} are the proportional and integral gains of the inner PI controller, and M_d and M_q are the auxiliary states of the inner loop integral controller.

the signal processing and the valve switching dynamics of the converter can be modeled as a 1^{st} order differential equation shown below:

$$\boldsymbol{v}_{cdq} + \tau_c \frac{d}{dt}\boldsymbol{v}_{cdq} \ = \boldsymbol{v}^*_{cdq} \tag{3.7}$$

However, due to the very small converter time constant τ_c, which is $\tau_c = \frac{1}{F_{SW}}$, and the switching frequency F_{SW} is very high, greater than 1 kHz, the dynamics of the converter delay can be neglected.

In addition to the inner control loop equation, the PLL dynamic equations can be written as follows:

$$\frac{d}{dt}\theta_{pll} = K_{p_{pll}} u_{t_q} + M_{pll} \tag{3.8}$$

$$\frac{d}{dt}M_{pll} = K_{i_{pll}} u_{t_q} \tag{3.9}$$

From (3.1) to (3.4), the dynamic equation of the dq current components can be written as follows:

$$\frac{d}{dt}i_{f_d} = -\frac{K_{p_{in}} + R_f}{L_f} i_{f_d} + \frac{K_{p_{in}}}{L_f} i^*_{f_d} + \frac{1}{L_f} M_d \tag{3.10}$$

$$\frac{d}{dt}i_{f_q} = -\frac{K_{p_{in}} + R_f}{L_f} i_{f_q} + \frac{K_{p_{in}}}{L_f} i^*_{f_q} + \frac{1}{L_f} M_q \tag{3.11}$$

To couple the AC side with the DC side of the VSC, we assume that the converter switches are lossless. Hence, the DC active power is equal to the AC active power at PCC subtracting the losses in R_f, as in (3.12):

$$P_{DC} = I_{DC} V_{DC} = P_{AC} = 1.5(u_{t_d} i_{f_d} + u_{t_q} i_{f_q}) - i^2_{f_d} R_f - i^2_{f_q} R_f \tag{3.12}$$

then

$$I_{DC} = \frac{u_{t_d} i_{f_d} + u_{t_q} i_{f_q} - i^2_{f_d} R_f - i^2_{f_q} R_f}{V_{DC}} \tag{3.13}$$

The outer control loops

In this work, there are three different types of the VSCs based on the control mode: Droop controlled GS VSCs, Constant power controlled VSCs, and AC voltage-frequency

controlled WF VSCs. This subsection provides the modeling of the outer control loop of the three types.

Constant power control mode

This control mode is used in rectification mode VSCs, in which the reference dq current signals is calculated by the outer loops to control active and reactive power flow through the converter. Equations (3.14) to (3.17) are the outer control loops equations of the constant power control:

$$i^*_{f_d} = K_{p_d}(P^* - P) + N_d \tag{3.14}$$

$$i^*_{f_q} = -K_{p_q}(Q^* - Q) + N_q \tag{3.15}$$

$$\frac{d}{dt}N_d = K_{i_d}(P^* - P) \tag{3.16}$$

$$\frac{d}{dt}N_d = -K_{i_q}(Q^* - Q) \tag{3.17}$$

where P and Q are the measured imported/exported active and reactive of the VSC.

$$P = u_{t_d}\ i_{g_d} +\ u_{t_q}\ i_{g_q} \tag{3.18}$$

$$Q = u_{t_q}\ i_{g_d} -\ u_{t_d}\ i_{g_q} \tag{3.19}$$

DC voltage droop control mode

For the droop controlled VSCs, the outer loop is the same as that of the constant power controlled VSCs. However, instead of using constant reference signal, the reference signal of the active power is calculated by the DC voltage droop equation (2.3).

AC voltage and frequency controlled VSCs

For wind farms or isolated grids, the HVDC VSC station acts as the AC slack bus for the entire grid and carries the responsibility of controlling the AC voltage and the

frequency. In wind farms, the HVDC terminal controls the AC voltage and the frequency, while the wind generators control their output active and reactive powers. The Ac voltage level at the PCC of the WF VSC is controlled by controlling its dq components through the outer loop of the local controller as in (3.20) and (3.21). On the other hand, instead of measuring the frequency using a PLL as in the grid-frequency imposed VSCs, a constant frequency signal is applied to a VCO to emulate the PLL and generate the reference frame transformation angle required for the transformation from the abc frame to the dqo frame and vice versa [18]:

$$i^*_{f_d} = K_{p_{out}}(u^*_{t_d} - u_{t_d}) + Nd - \omega C_f u_{t_q} + i_{g_d} \tag{3.20}$$

$$i^*_{f_q} = K_{p_{out}}(u^*_{t_q} - u_{t_q}) + Nq + \omega C_f u_{t_d} + i_{g_q} \tag{3.21}$$

$$\frac{d}{dt}N_d = K_{i_{out}}(u^*_{t_d} - u_{t_d}) \tag{3.22}$$

$$\frac{d}{dt}N_q = K_{i_{out}}(u^*_{t_q} - u_{t_q}) \tag{3.23}$$

3.2.2 Dynamic model of the AC grid

In this work, the AC grid is modeled by its reduced order Thévenin equivalent circuit shown in Fig. 3.1. which is consists of a voltage source as a slack bus and a series complex impedance. The magnitude of the equivalent impedance Z_g is based on the short circuit ratio of the AC grid (3.24), and this magnitude is considered the main difference between a stiff (a strong) grid and a weak grid [19], [70] and [46]. And the values of the equivalent resistance R_g and inductance L_g are calculated from the X/R ratio, as the angle of the impedance is calculated from $\phi_g = tan^{-1}(\frac{X}{R})$. Hence, $R_g = |Z_g|cos\phi_g$ and $L_g = \frac{X_g}{\omega}sin\phi_g$.

$$|Zg| = \frac{U_g^2/SCR}{P_{rated}} \tag{3.24}$$

The dynamic equations of the AC grid equivalent circuit and the AC filter capacitor are stated as follows:

$$\frac{d}{dt}i_{g_d} = -\frac{R_g}{L_g}i_{g_d} + w\ i_{g_q} - \frac{1}{L_g}u_{t_d} + \frac{1}{L_g}u_{g_d} \tag{3.25}$$

$$\frac{d}{dt}i_{g_q} = -\frac{R_g}{L_g}i_{g_q} - w\ i_{g_d} - \frac{1}{L_g}u_{t_q} + \frac{1}{L_g}u_{g_q} \tag{3.26}$$

$$\frac{d}{dt}u_{t_d} = \frac{1}{C_f}i_{g_d} - \frac{1}{C_f}i_{f_d} + \omega\ u_{t_q} \tag{3.27}$$

$$\frac{d}{dt}u_{t_q} = \frac{1}{C_f}i_{g_q} - \frac{1}{C_f}i_{f_q} - \omega\ u_{t_d} \tag{3.28}$$

where the u_{g_d} and u_{g_q} are the real and imaginary components of the grid voltage in dq frame, which is the reference frame of the VSC. In steady-state operation, the dq frame is synchronized with the AC grid reference frame (xy), i,e,. $\theta_{pll_{dq}} = \theta_{pll_{xy}}$. And in case of the occurrence of any disturbances, the dynamics of the PLL shifts the dq frame from the xy frame by a certain angle θ during the transient period. Hence, $\theta_{pll_{dq}} = \theta_{pll_{xy}} + \theta$. Therefore, in order to couple the two reference frames, the grid voltage $u_{g_{xy}}$ is transferred to the dq frame as follows:

$$u_{g_d} = \hat{U}_g cos(\delta) sin(\theta_{pll_{dq}}) - \hat{U}_g sin(\delta) cos(\theta_{pll_{dq}}) \tag{3.29}$$

$$u_{g_q} = \hat{U}_g cos(\delta) cos(\theta_{pll_{dq}}) + \hat{U}_g sin(\delta) sin(\theta_{pll_{dq}}) \tag{3.30}$$

where $\hat{U}_g$ is the magnitude of the grid voltage, and δ is angle between the grid voltage u_g and the voltage at the PCC u_t.

In wind farms, the outer voltage control loops dynamics are decoupled by the feed forward apart from the wind farm grid dynamics. Therefore, the wind farm AC grid is modeled as an ideal three-phase current source in parallel with the AC filter capacitor. The value of the WF VSC input current $i_g = \frac{S_g}{3\hat{V}_t}$, and the dynamic equations of the WF AC grid are (3.27) and (3.28).

3.2.3 Dynamic model of the HVDC network

In this work, the DC cables and lines are modeled by the equivalent π-sections model. as shown in Fig. 3.1. For every i^{th} DC bus, the i^{th} VSC's DC capacitor is combined with the cable equivalent capacitance at that bus, resulting in a dynamic differential equation for the DC voltage V_{DC_i} at the bus i (3.31). For the DC lines between the buses i and j, equation (3.32) shows the dynamic equation of the line conductor current I_{ij}.

$$\frac{d}{dt}V_{DC_i} = \frac{1}{C_i}I_{DC_i} + \frac{1}{C_i}\sum I_{ij},\ \forall i \in N_B\ \&\ j \in n_B. \tag{3.31}$$

$$\frac{d}{dt}I_{ij} = -\frac{R_{ij}}{L_{ij}}I_{ij} + V_{DC_i} - V_{DC_j},\ \sum I_{ij},\ \forall i \in N_B\ \&\ j \in n_b. \tag{3.32}$$

where I_{DC_i} is the output current of the VSC at the i^{th} bus, $C_i = C_{DC_i} + 0.5\sum C_{ij}, \forall i, j \in N_B$, R_{ij}, L_{ij} and C_{ij} are the equivalent parameters (resistance , inductance and capacitance, respectively) of the line between buses i and j.

3.3 Steady-State Model of the MT HVDC Network

To implement the OPF algorithm responsible for calculating the optimal droop-control reference voltages, the steady-state model of the MT VSC-HVDC network is derived. In this model, DC transmission lines are assumed to be purely resistive. Equation (3.33) is the general load flow equation at bus i [71]:

$$G_{ii}V_i^2 - V_i\sum_{j\in n_b} G_{ij}\mathrm{V_j} - P_i = 0\ \ \forall\ i\ \ \in N_B\ \ \ j \in n_b \tag{3.33}$$

where $G_{ij} = 1/R_{ij}$ is the line conductance between buses i and j; P_i is the net input power of the converter i (from bus i to converter i); V_i and V_j are the DC voltages of the i^{th} and j^{th} buses, respectively; and $G_{ii} = \sum G_{ij}\ \forall\ i\ \in N_B\ \&j \in n_b$

In MT HVDC networks, there are three types of buses in the network (power output buses, power input buses, and connection buses), the power flow equations are as follows:

Power Output Buses : The buses, which are connected to the current droop-control converters, using the droop equation (2.3) and substituting it into (3.33) gives the following droop equation for bus i:

$$G_{ii}V_i^2 - V_i \sum_{j \in n_b} G_{ij}V_j + G_{Di}V_i\,(V_i - V_{oi}) = 0 \;\forall\; i \;\in N \tag{3.34}$$

where $G_{D_i} = \frac{1}{R_{D_i}}$.

Power Input Buses : Equation (3.33) is the load flow equation for the bus that is connected to a rectification mode converter and whose output power is controlled through a constant power controller. At steady-state, the output power of that converter equals its reference active power setting.

$$G_{ii}V_i^2 - V_i \sum_{j \in n_b} G_{ij}V_j - P_i^* = 0 \;\forall\; i \;\in M \tag{3.35}$$

where P_i is the active power of the i^{th} power input converter.

Connection Buses : The connection bus is the bus that is not connected to any converter; the following is the load flow equation at connection bus i:

$$G_{ii}V_i^2 - V_i \sum_{j \in n_b} G_{ij}V_j = 0 \;\forall\; i \;\in O \tag{3.36}$$

where N, M, and O are the sets of the output, input, and connection buses, respectively; Ii is the input or output DC current at the i^{th} node; and V_{o_i} and R_{D_i} are the droop-control parameters of the converter at the i^{th} node.

3.4 Discussion

Through this chapter, A mathematical modeling of MT VSC-HVDC is illustrated for both transient and steady-state dynamics. The steady- state modeling is presented to be used

in chapter 4 for the load flow analysis and optimal power sharing control algorithms, while, the transient dynamics mathematical modeling equation is used for deriving the linearized state-space model of the MT VSC-HVDC transmission system to be used in the proposed tuning methodology in chapter 5.

Chapter 4

Power Sharing Control Strategy of Multi-terminal VSC-HVDC Transmission Systems Utilizing Adaptive Voltage Droop

4.1 Introduction

In this chapter a power-sharing control strategy that utilizes an adaptive voltage-droop scheme is provided. In the proposed power-sharing control strategy, the voltage-droop parameters are optimally selected as a means of achieving accurate power-sharing based on the desired shares, which are optimized in advance by the system operator in order to fulfill the active power requirements of the connected AC grids to achieve their local operating objectives, while also including consideration of the DC voltage dynamics, including transient and steady-state performance.

4.2 Proposed Power-Sharing Control Strategy

The proposed power-sharing controller is a two-level hierarchal controller [72]. Its layout in Fig. 4.1 includes a high-level supervisory centralized controller that computes and sends the optimal droop parameters (i.e., R_D and V_o) to the primary controller of the power output converters. In order to achieve the main two objectives of the control strategy, which are the DC voltage dynamics enhancement and the power-sharing control accuracy improvement, the supervisory controller selects the optimal droop parameters in two steps following receipt of the required data: the DC network configuration and parameters, the available input power, and the desired power shares. At the beginning, the optimal droop gains of the droop-controlled converters (i.e., output converters) are selected once using the methodology explained in subsection 4.2.1. However, this process should be repeated for each change in the HVDC network configuration (i.e., a change in the number of converters due to a converter entering or exiting the service, or a change in the DC network topology because of the connection or disconnection of DC links).

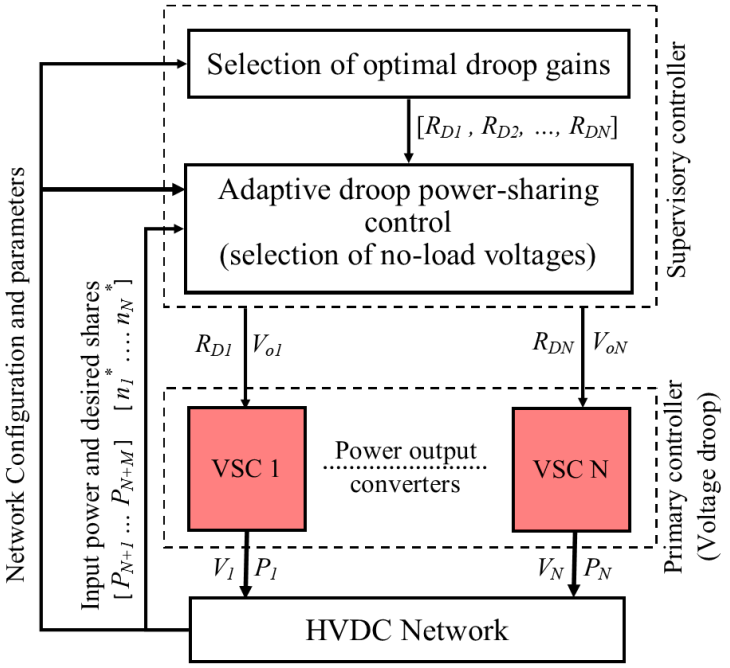

Figure 4.1: Structure of the proposed MT VSC-HVDC power-sharing controller

After selecting the droop gains, the supervisory controller chooses the optimal values for the droop reference voltage using the power sharing control algorithm explained in subsection 4.2.2. The data required for performing this process is the power available to be input to the HVDC network, specifically, the generation from connected wind farms, which can be obtained from the forecasted data, and/or the surplus active power that can be imported from connected AC grids. An additional requirement is the desired percentage shares, which is set by the operator based on a variety of scenarios. For example, in the priority-sharing scheme, one of the power output converters would be assigned the priority of absorbing a specific amount of active power, while the other converters would share the extra power. The power shares may change based on the power trading that takes place during the day. This process is repeated periodically so that the percentage shares is maintained at the desired value. The updating rate of the droop parameters is set based on the rate of change of the wind power. Any deviation in the input power produces a deviation in the output buses voltage level, which in turn affects the power-sharing accuracy. Hence, the faster the update rate, the better the power-sharing accuracy given reliable communication speed.

4.2.1 Methodology for selecting the optimal droop gains

The value of the droop gain affects the system DC voltage dynamics as a result of the change in the DC power input to the system (i.e., active power that is delivered by wind farm VSCs). As revealed in the simulation results presented below, changing the droop gain value affects both transient and steady-state DC voltage dynamics. Increasing the droop gains tends to improve the transient response of the DC voltage, and the accuracy of the power-sharing increases as the sensitivity of the sharing to transmission line resistance decreases; however, the steady-state voltage level at the DC network buses increases and may exceed the upper voltage limits (+5%) [21]. The small-signal stability analysis expressed in section (4.2.2) confirms that the system is stable for any positive droop gain value. When the droop gains are increased, all of the eigenvalues become increasingly negative without any effect on the damping frequency. The objective of the proposed methodology is the selection of the optimal droop-gain values that will lead to the best possible DC voltage transient response to variations in input power or an output converter

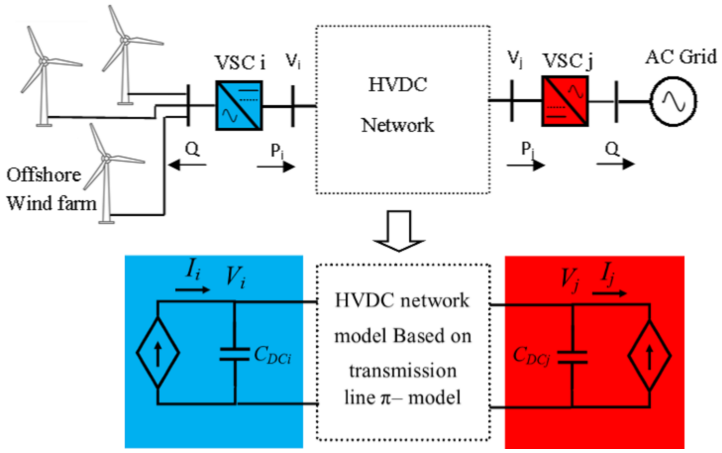

Figure 4.2: Average model of an MT VSC-HVDC system

outage, without changes in the system parameters and without violating the voltage limits [73].

In this work, to study the DC voltage transient as a function of the droop gains, a state-space model of the MT HVDC system is derived for the droop-gain selection. The dynamics associated with the converter switching and the harmonics are not considered. Thus, the VSCs are represented by their average models, in which the DC side is modeled as a current source with a capacitor in parallel, see Fig. 4.2 [21], [74]. However, the derivation of the system model are based on a main assumption, which is the inner and the outer control loops of the onshore VSCs are assumed to be well designed and to have a first or second order filter response. According to these assumptions, the AC voltage at the point of common coupling of the onshore VSC is not affected by the power flow through the converter. Furthermore, in the offshore wind farms, the VSC controls the frequency and the AC voltage. The AC voltage level at the wind farm VSC terminals is controlled regardless of the amount of power flowing through the converter. In addition, according to the small signal stability analysis in [38], the critical modes, i.e., the most right eigenvalues, are mostly associated with the DC network and the droop controller states. Hence, the DC voltage dynamics are further influenced by the DC network parameters and the droop gains. Accordingly, each VSC is represented by a current source in parallel with a DC capacitor. This representation is also used for droop controlled DGs in DC microgrids [40]:

The DC current values of the droop-controlled VSCs can be calculated using (2.2), and for any i^{th} power input VSC, its output DC current value Ii is proportional to its incoming active power Pi, assuming that its voltage Vi always remains close to its nominal value [21], hence, the current value is hence

$$I_i = \frac{P_i}{V_i} \tag{4.1}$$

Equations (4.2) to (4.7) represent the dynamic differential equations for the system.

Lines Equations:

$$\frac{d}{dt}I_{ij} = -\frac{R_{ij}}{L_{ij}}I_{ij} + \frac{1}{L_{ij}}(V_i - V_j),\ \forall\ i \in N_B\ \&\ j \in n_b. \tag{4.2}$$

where R_{ij} and L_{ij} are the resistance and inductance of the DC link between nodes i and j, respectively; V_i and V_j are the DC voltages of nodes i and j, respectively; and I_{ij} is the current flows from node i to node j. All DC line connecting the DC buses are numbered from 1 to T in the state space model, where T is the total number of the DC lines. Thus, they are numbered from I_{l_1} to I_{l_T}.

Buses Equations:

For power output (droop-based buses), the closed loop transfer function of the DC voltage controller, in which the reference voltage I_i^* is calculated by the droop equation (2.3), is assumed to have a first order filter response as in (4.3):

$$\frac{I_i(s)}{I_i^*(s)} = \frac{1}{\tau_c S + 1}. \tag{4.3}$$

where τ_C is the time constant of the VSC. From (4.3) the dynamic differential equation of the DC voltage controller is as follows

$$I_i^* = \tau_C \frac{d}{dt}I_i + I_i,\ \forall\ i \in N. \tag{4.4}$$

Using equation (4.1) and (4.4), the dynamic equation of the power output buses is

$$\frac{d}{dt}\ V_i{=}\frac{-G_{D_i}}{C_i+G_{D_i}\ T}\ \ (V_i-V_{o_i})+\frac{1}{C_i+G_{D_i}\ T}\sum_{j\in n_b} I_{ij},\ \forall i\in N \tag{4.5}$$

For power input buses,

$$\frac{d}{dt}\ V_i{=}\frac{1}{C_i}\ I_i{+}\frac{1}{C_i}\sum_{j\in n_b} I_{ij}\quad \forall\ i\ \in M \tag{4.6}$$

For connection buses,

$$\frac{d}{dt}\ V_i{=}\frac{1}{C_i}\sum_{j\in n_b} I_{ij}\ \forall\ i\ \in O \tag{4.7}$$

where

$$C_i{=}C_{dci}{+}\ \sum_{j\in n_b} C_{ij}, \forall\ i\ \in N_B \tag{4.8}$$

$$G_{D_i}=\frac{1}{R_{Di}} \tag{4.9}$$

where N_B, N, M, and O are the sets of the total, output, input, and connection buses, respectively; n_b is the set of buses connected to bus i; I_i is the input or output DC current at the i^{th} node; and V_{o_i} and R_{D_i} are the droop-control parameters of the converter at the ith node. From equations (4.2) and (4.5) to (4.7) the state-space model can be represented as follows:

$$\dot{\boldsymbol{x}}_{\boldsymbol{DC}}=\boldsymbol{A}_{\boldsymbol{DC}}\ \boldsymbol{x}_{\boldsymbol{DC}}+\boldsymbol{B}_{\boldsymbol{DC}}\ \boldsymbol{u}_{\boldsymbol{DC}},\quad \boldsymbol{y}_{\boldsymbol{DC}}=\boldsymbol{C}_{\boldsymbol{DC}}\ \boldsymbol{x}_{\boldsymbol{DC}} \tag{4.10}$$

where

$\boldsymbol{x}_{\boldsymbol{DC}}{=}[I_{l_1}\ldots I_{l_T}\ \ V_1\ldots\ V_{N+M+P}]^T$

$\boldsymbol{u}_{\boldsymbol{DC}}=[V_{o_1}\ldots V_{o_N}\ldots\ I_{N+1}\ I_{N+2}\ldots\ I_{N+M}]^T$

$\boldsymbol{y}_{\boldsymbol{DC}}=[V_1V_2\ldots V_{N+M}\ ]^T$

To find a direct relation between the voltage deviation at the input buses and the variation in the input currents, the state-space model is modified through linearization as follows:

$$\Delta \dot{\boldsymbol{x}}_{\boldsymbol{DC}} = \boldsymbol{A}_{\boldsymbol{DC}}\ \Delta \boldsymbol{x}_{\boldsymbol{DC}} + \boldsymbol{B}_{\boldsymbol{DC}}\ \Delta \boldsymbol{u}_{\boldsymbol{DC}},\quad \Delta \boldsymbol{y}_{\boldsymbol{DC}} = \boldsymbol{C}_{\boldsymbol{DC}}\ \Delta \boldsymbol{x}_{\boldsymbol{DC}} \tag{4.11}$$

where

$\Delta \boldsymbol{x}_{\boldsymbol{DC}}$=$[\Delta i_{l1}\ \ldots\ \Delta i_{lT}\ \Delta V_1 \ldots\ \ \Delta V_{N+M+P}]^T$

$\Delta \boldsymbol{u}_{\boldsymbol{DC}}$=$[\Delta I_{N+1}\ \Delta I_{N+2} \ldots..\ \Delta I_{N+M}]^T = \boldsymbol{\Delta I}$

$\Delta \boldsymbol{y}_{\boldsymbol{DC}}$=$[\Delta V_{N+1} \Delta V_{N+2} \ldots..\Delta V_{N+M}\ ]^T = \boldsymbol{\Delta V}$

$$\overline{\boldsymbol{B}_{\boldsymbol{DC}}} = \begin{bmatrix} \frac{1}{C_{N+1}} & \cdots & 0 \\ \vdots & \ddots & \vdots \\ 0 & \cdots & \frac{1}{C_{N+M}} \end{bmatrix}$$

where $\boldsymbol{\Delta I}$ is the vector of the input bus incoming current, $\boldsymbol{\Delta V}$ is the vector of the input bus voltage, and R_l and L_l are the resistance and inductance of the DC line.

To find a relation between the steady-state voltage deviation and input power variations as a function of the droop gains, the transfer matrix of the system in 4.11, which is a function in the droop gains, as indicated in (4.12), and the steady-state gain matrix (4.13) [75] can be determined as follows:

$$\boldsymbol{G}\,(\boldsymbol{s}) = \frac{\Delta \boldsymbol{V}(\boldsymbol{s})}{\Delta \boldsymbol{I}(\boldsymbol{s})} = \overline{\boldsymbol{C}}(\boldsymbol{sI} - \boldsymbol{A})^{-1}\overline{\boldsymbol{B}} \tag{4.12}$$

$$\boldsymbol{H} = \lim_{\mathrm{s}\to 0} \boldsymbol{G}\,(\boldsymbol{s}) \tag{4.13}$$

The steady-state voltage deviation $\Delta \boldsymbol{V}_{ss}$ due to a change in the input current can then be calculated as follows:

$$\Delta \boldsymbol{V}_{ss} = \boldsymbol{H}.\ \boldsymbol{\Delta I}_{ss} \tag{4.14}$$

The maximum possible voltage deviation in the system is found from:

$$\Delta V_{max} = ||\boldsymbol{H}.\ \boldsymbol{\Delta I_{max}}||_{\infty} \tag{4.15}$$

where $\Delta \boldsymbol{I}_{max} = [\ \Delta I_{N+1_{max}}\ \Delta I_{N+2_{max}} \ldots..\ \Delta I_{N+M_{max}}]^T$ is the vector containing the maximum possible changes in the input currents. To achieve the objective of this methodology, the real part absolute value of the least negative eigenvalue of the transition matrix $\mathbf{A}$ is maximized, thus guaranteeing the minimization of the real part of all of the eigenvalues

and hence enhancing the maximum overshoot and settling time of the voltage. The optimal droop gain selection optimization problem is formulated as in (4.16) and (4.17):

$$\min_{z}(\sigma_{max}\,(z)) \tag{4.16}$$

where σ_{max} is the maximum real part of the system eigenvalues. The objective function is subject to the following constraints:

$$\Delta V_{max}(z) \leq V_{DC\,max} - V_{o_{max}} \tag{4.17}$$

where z is the vector of the droop-controlled VSC droop gains as follows:

$$z=[R_{D_1}\ldots R_{D_N}]^T \tag{4.18}$$

$V_{o_{max}}$ is the largest no-load voltage value, which becomes the upper bound of the voltage reference values in the DC OPF algorithm, as explained in the next subsection, and $\Delta V_{max_{out_i}}(z)$ is the steady-state maximum DC voltage deviation as a result of the disconnection of the output converter i. The value of $\Delta V_{max_{out_i}}(z)$ is calculated for all possible single output converter outage scenarios by using equations (4.12) to (4.15), but with the value of the disconnected converter i droop gain is set to $G_{D_i} = \frac{1}{R_{D_i}} = 0$. The value of $V_{o_{max}}$ is selected to be greater than the mid-point between $V_{dc_{max}}$ and $V_{dc_{min}}$ as in (4.19). Hence, when the power flow direction is reversed in an output converter the DC voltage will not violate the $V_{dc_{min}}$at the selected droop gains, which is selected to prevent the DC voltage from exceeding the upper limit at the maximum power, i.e. rated power.

$$V_{o_{max}} > \frac{V_{dc_{max}} + V_{dc_{min}}}{2} \tag{4.19}$$

In optimal droop gain selection methodology, the selection of the droop gain can be adjusted by changing the values of $V_{o_{max}}$ or$\Delta \boldsymbol{I}_{max}$. Selecting a lower $V_{o_{max}}$ value results in a higher droop gain without violation of the voltage limits, which increases the accuracy of the power-sharing. For extreme variations, the $\Delta \boldsymbol{I}_{max}$ vector elements are selected to represent the maximum change in the current and thus equal the twice rated current for the onshore grids VSCs or the rated current for wind farm VSCs. However, under normal operating conditions, fewer variations in active power occur because it does not change from zero to the rated value. Hence, $\Delta \boldsymbol{I}_{max}$ elements can be selected as the maximum possible change in the current during a specific period based on forecasted data. In this case, the droop-gain selection step could be repeated periodically whenever the value of $\Delta \boldsymbol{I}_{max}$ changes.

4.2.2 Optimal adaptive droop power-sharing control

The objective of the algorithm is the selection of optimal droop-control reference voltages for the output converters in order to achieve accurate active power-sharing based on optimized-predetermined desired shares. The algorithm is formulated as expressed in (4.20) to (4.28):

The objective function is the minimization of the root of the average squared errors:

$$\min_{\boldsymbol{v}} \sqrt{\frac{\sum_{i=1}^{N} e_i(v)^2}{N}} \tag{4.20}$$

where e_i is the difference between a) the desired percentage share n_i^*, which is set by the operator in order to define the percentage share of the total input power of each output converter, and b) the actual share of the power output by the i^{th} VSC, as calculated by (4.21); $\boldsymbol{v}$ is the vector of the output reference (no-load) voltages of the converters and the DC voltages at all buses, $\boldsymbol{v} = [V_{o_1} \dots V_{o_N}\ V_1 \dots V_N]^T$:

$$e_i = n_i^* - \frac{P_i}{P_G - P_{loss}} \tag{4.21}$$

where P_i is the power output through the i^{th} VSC that can be calculated from 2.3. P_G is the total power input to the HVDC network, i.e., the summation of the reference power values of the constant power-controlled converters in (4.22), and P_{loss} is the total transmission loss from the DC network, as computed by (4.23) and (4.28), respectively:

$$P_G = \sum_{\forall j \in M} P_j^* \tag{4.22}$$

$$P_{loss} = \sum_{\forall\ i \in N_B} \sum_{\forall\ j \in N_B} G_{ij}(V_i - V_j)^2 \tag{4.23}$$

The objective function is subject to the following constraints:

$$g(\boldsymbol{v}, \boldsymbol{P}) = [g_1 \dots g_{NB}]^T = 0 \tag{4.24}$$

$$V_{dc_{min}} \leq V_i \leq V_{dc_{max}}\ , \qquad \forall\ i \in N_B \tag{4.25}$$

$$V_{o_{min\,i}} \leq V_{o_i} \leq V_{o_{max}}, \quad \forall\, i \in N \tag{4.26}$$

$$|P_i| \leq P_{i_{max}}\ , \quad \forall\, i \in N \cup M \tag{4.27}$$

$$I_{dc_k} \leq I_{dc_{k_{max}}}\ , \quad \forall\, k \in L \tag{4.28}$$

where L is the set of DC network links. Equation (4.24) shows the nonlinear equality constraints, where, g_1 to g_N is represented by (3.34), g_{N+1} to g_{N+M} equals (3.35), and (3.36) shows the value of g_{N+M+1} to $\mathrm{g_{NB}}$. In the non-equality constraints (4.25) to (4.28), $V_{dc_{min}}$ and $V_{dc_{max}}$ are the lower and upper DC voltage terminal limits, respectively; $P_{i_{max}}$ indicates the maximum power of the i^{th} converter; and the maximum DC current capacity of the link k is denoted by $I_{dc_{k_{max}}}$, and $V_{o_{min\,i}}$ is the minimum no-load voltage value for the converter i. The value of $V_{o_{min\,i}}$ is calculated for every output converter by (4.29) in order to avoid the violation of the lower DC voltage limit after any power flow direction reversal in the output converter i.

$$V_{o_{min_i}} = V_{dc_{min}} + \frac{R_{D_i}\, P_{rated_i}}{V_{dc_{min}}}\ , \forall\, i \in N \tag{4.29}$$

where R_{D_i} and P_{rated_i} are the droop gain and the rated active power of the i^{th} output converter.

This optimal power flow optimization problem, which is nonlinearly constrained, is solved using a trust region reflective optimization algorithm [76].

4.3 Simulation Results

The proposed control strategy was validated on the CIGRE B4 DC grid test system, which includes two onshore AC grids and four offshore AC grids (wind farms). The AC grids are connected by three HVDC grids: DCS1, DCS2, and DCS3, with seven VSCs overall. Detailed system data can be found in [2].

In this work, the modified bipolar 400 KV DC grid DCS3 meshed HVDC grid (Fig. 4.3) was only used as a test system after some modifications, with two-offshore wind farms, D and C, connected to onshore AC grids A, B and E through overhead and cable DC links. AC grid B has two VSCs that interface with DCS3: Cb-B1 and Cb-B2 at buses: B1 and

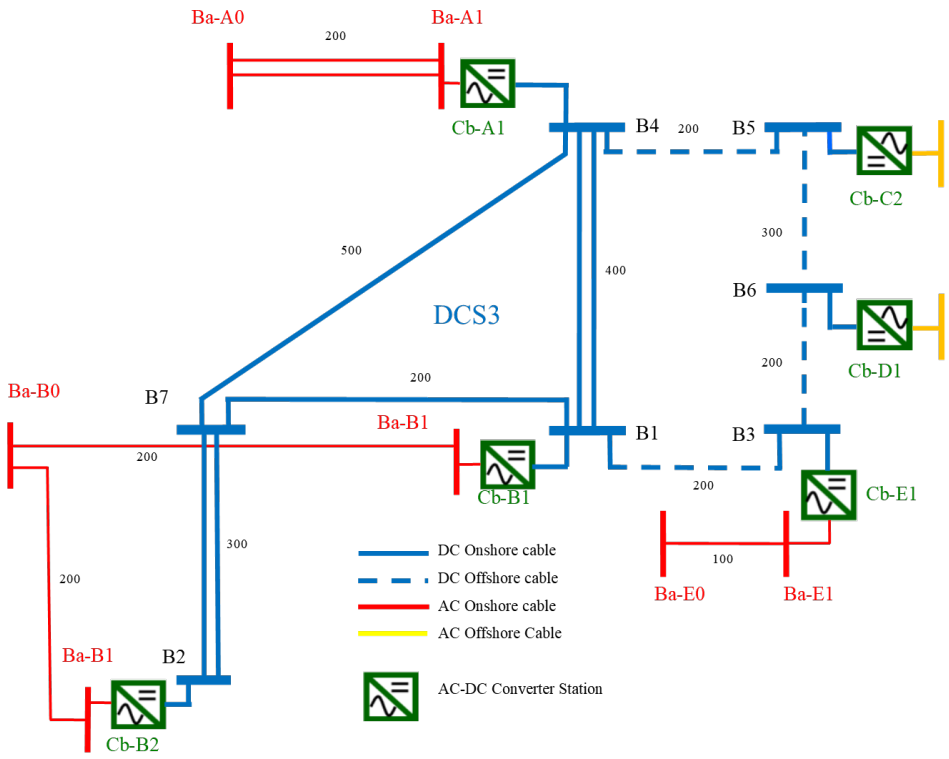

Figure 4.3: Modified CIGRE B4 DC grid test system (DCS3) [2]

B2, respectively. AC grids A and E, and wind farms D1 and C2 are connected to the DCS3 DC grid through VSCs: Cb-A1 at bus B4, Cb-E1 at bus B3, Cb-C2 at bus B5, and Cb-D1 at bus B6. The converter parameters and line data are as stated in Table 4.1 and Table 4.2, respectively. Per unit data were calculated based on common base values, as follows: $S_{base} = 1200\ MVA$, $V_{dc_{base}} = 400\ KV$ onshore and offshore $V_{AC_{base}} = 120KV$, The DC voltage limits of the system were set to be + 5 % and -10 %.

Based on predefined active power-sharing scheme, converters Cb-B1, Cb-B2, and Cd-E1 share the active power delivered to the DC grid, which is the summation of the power generated by wind farms C and D and that imported from AC grid A. The DSC3 grid buses are thus divided into three types of buses: three power output buses (B1, B2, and B3); three power input buses (B4, B5, and B6); and one connection bus (B7). To achieve this sharing scheme, the proposed supervisory controller selects and sends the optimal

droop parameters (i.e., R_D and V_o to converters Cb-B1 and Cb-B2 and to the Cd-E1 voltage-droop controller.

Table 4.1: Converter Station Data per Pole

	Cb-A1	Cb-B1	Cb-B2	Cb-C2	Cb-D2	Cd-E1
Srated [MW]	1200	1200	1200	400	800	1000
R_f [Ω]	0.403	0.403	0.403	1.21	0.605	1.92
L_f [mH]	33	33	33	98	49	800
C_f [F]	3.3	3.3	3.3	33	33	3.3
C_{dc} [F]	450	450	450	150	300	334

Table 4.2: Lines Data

	R [Ω/km]	L [mH/km]	C [μF/km]	G [μF/km]	I_{max} [A]
DC OHL 400 kV	0.0114	0.9356	0.0123	-	3500
DC Cable 400 kV	0.0095	2.112	0.1906	0.048	2265
AC cable 145 kV	0.0843	0.2526	0.1837	0.041	715
AC OHL 380 kV	0.02	0.8532	0.0135	-	3555

4.3.1 Effects of changing droop gains

The state-space model of the test system DC network is derived from (4.11) and the modeling steps explained in section 4.2. with the selection of the lines' currents and DC buses' voltages as the system states and the DC voltages at the input buses as the outputs, the system state space model (4.11) matrices are derived in the appendix.

Fig. 4.4b shows the effects of the droop-gain value on the DC voltage dynamics due to a step change in the input power (Fig. 4.4a), based on the assumption that all droop-control converters have the same R_D with $R_o = 0.95$. Increasing the value of the droop gain tends to improve the transient performance of the DC voltage; however, the deviation in the steady-state voltage increases and may violate voltage limits.

The small-signal stability study shows the system to be stable for all positive droop gain values and indicates that the system eigenvalues become increasingly negative as the droop gains rise, thus improving transient performance, as shown in Fig. 4.5.

(a)

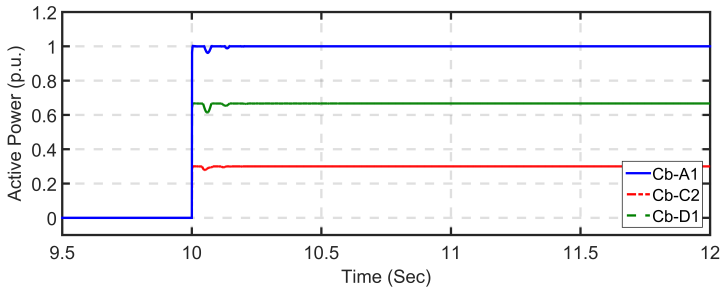

(b)

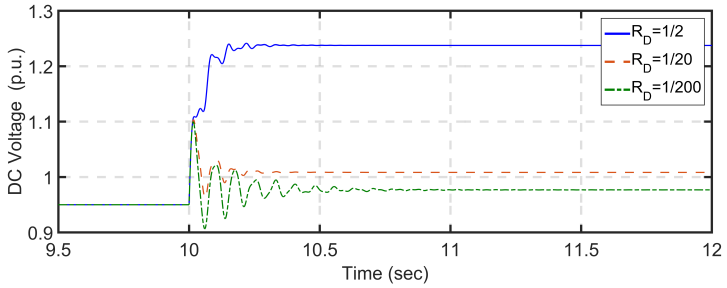

Figure 4.4: Changes in droop gains: (a) Step change in the input converter power. (b) Effect of the droop gain values on the DC voltage dynamics.

The supervisory controller selects the optimal droop gain for the system by setting the maximum change in the input currents to equal the p.u. rated power values of the power input converters, so $\Delta \boldsymbol{I_{max}} = [1,\ 0.666,\ 0.334]^T$ p.u. The optimal droop gains at two different $V_{o_{max}}$ values are shown in Table 4.3. As indicated in Fig.4.6, selecting a lower $V_{o_{max}}$ value results in higher droop gain values, and thus more accurate power-sharing with an enhanced dynamic response, all without violating the DC voltage limits at the power input buses.

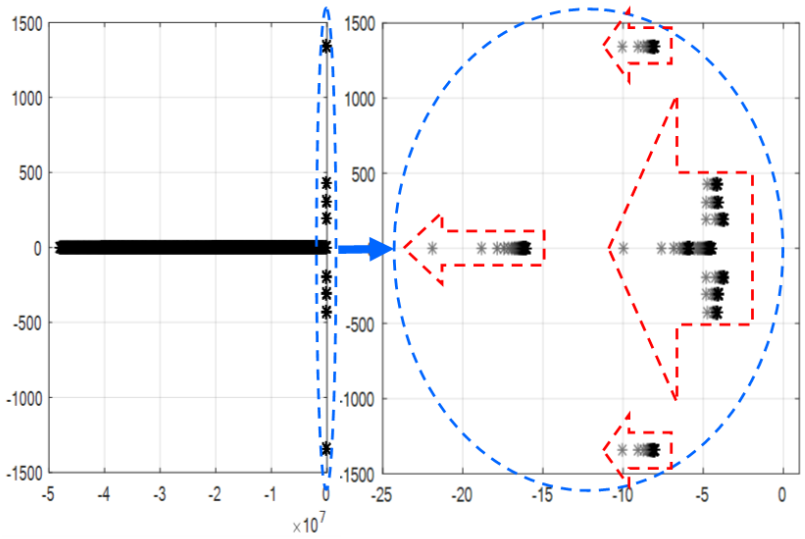

Figure 4.5: Movement of the eigenvalues due to the RD incremental from 0.001 to 1

Fig. 4.6 shows the DC voltage transient response after a converter outage in the Cb-E1 converter at second 10 as shown in Fig. 4.7. In this case, all power input converters deliver their rated power. The droop parameters of the output converters are set at $V_o = 0.95 p.u.$ and the R_D droop gains at the values that are listed in Table 4.3. As can be seen in Fig. 4.6, the selected droop gains by the droop gain selection methodology prevented the DC voltage from exceeding the upper limit.

Table 4.3: Optimum Droop Gains Values

$V_{o_{max}}$ [p.u.]	Cb-B1	Cb-B2	Cd-E1
1	0.01232	0.01249	0.01249
0.95	0.0597	0.05006	0.06697

(a)

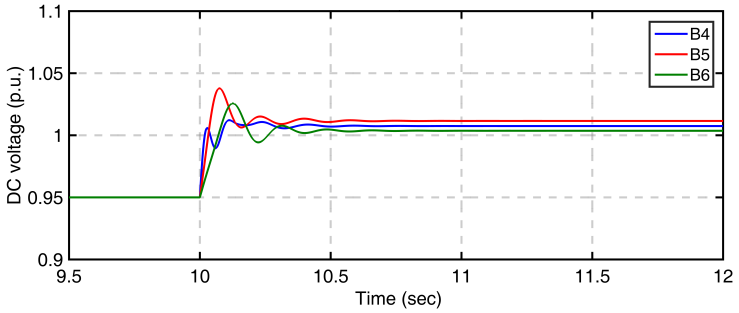

(b)

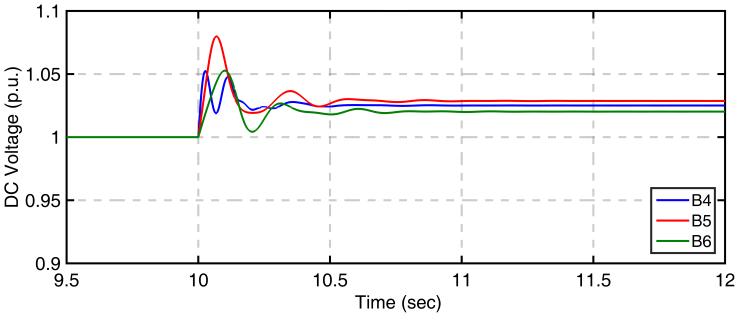

Figure 4.6: DC voltages of the input buses: a) $V_{o_{max}} = 0.95$; b) $V_{o_{max}} = 1$

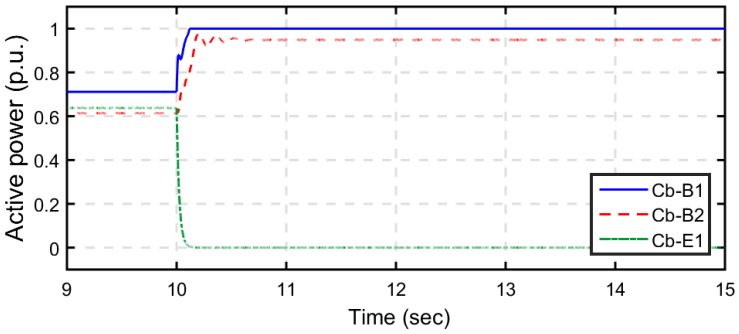

Figure 4.7: Active power of onshore power output converters during a converter outage.

4.3.2 Power-sharing base case

In this case, the active power delivered to the DC network by power input converters Cb-A1, Cb-C2, and Cb-D1 is equal to their rated power. The imported active power is shared among Cb-B1, Cb-B2, and Cd-E1 according to the desired percentage-shares of 30%:30%:40%, respectively. Their droop gains are set as in Table 4.3, with $V_{o_{max}} = 0.95$ p.u. Based on the available input power, desired shares, and droop-gain values, the proposed supervisory controller selects the optimal voltage reference for the power output controllers in order to achieve accurate power-sharing. Table 4.4 summarizes the results of the power flow for this case scenario. As can be seen, the optimal no-load voltage values produce actual power shares that are very close to the desired shares, while the DC voltage levels of the HVDC network are maintained within the recommended limits. The results reveal that the proposed control strategy provided accurate power-sharing control based on the desired sharing scheme.

Table 4.4: Power flow results for the base case scenario

DC Bus	Bus Type	Droop Parameters (R_D , V_o)	Voltage [p.u.]	Power [p.u.]	Percentage Share n
B1	Droop	0.0305, 0.9635	0.98145	-0.5885	29.99%
B2	Droop	0.0500, 0.9401	0.97042	-0.5885	29.99%
B3	Droop	0.0273, 0.9587	0.98058	-0.7847	40.02%
B4	P	-	0.996	1	-
B5	P	-	0.99975	0.6667	-
B6	P	-	0.99113	0.3333	-
B7	Connection	-	0.9782	-	-

However, if the input power to the HVDC system is changed and the no-load voltage values are not updated to the optimal values, the power-sharing control accuracy will be deteriorated and the deviation of the actual power shares from the desired shares will increase. Table V shows a power-sharing scenario with different input power. Two cases are considered: the first case is without optimizing the droop controller no-load voltage values after the input power diversion from the base case scenario values. The second case

is updating the no-load voltage values corresponding to the new input power. The new input powers are 0.5, 0.5, and 0.333 p.u. for VSCs Cb-A1, Cb-C2 and Cb-D1, respectively. The droop gains of the droop controllers are kept the same as the base case scenario. As can be concluded from the percentage shares (n) of the case of using non-optimal parameters and percentage shares (n) of the optimal parameter case in Table 4.5, which represent, the actual percentage shares of both cases, the accuracy of the power-sharing control worsened when the droop controller no-load voltage values are not updated. These findings demonstrate the importance of the proposed control strategy in improving the accuracy of power-sharing.

Table 4.5: Power flow results after changing the input power with and without optimal no-load voltage values

	Non-optimal				Optimal			
DC Bus	V_o	V [p.u.]	P [p.u.]	n	V_o	V [p.u.]	P [p.u.]	n
B1	0.9311	0.9692	0.3549	26.97%	0.9327	0.9748	0.3946	29.98%
B2	0.9101	0.9611	0.4092	31.09%	0.9183	0.9672	0.3946	29.98%
B3	0.992	0.9692	0.5518	41.93%	0.9199	0.9751	0.5271	40.04%
B4	-	0.9782	0.5	-	-	0.9838	0.5	-
B5	-	0.9822	0.5	-	-	0.9879	0.5	-
B6	-	0.9773	0.3333	-	-	0.9832	0.3333	-
B7	-	0.9666	-	-	-	0.9724	-	-

4.3.3 Sharing of variable-input-power case

This case demonstrates the ability of the control strategy to deal with input power caused by fluctuations in offshore wind farm generation or surplus power from AC grid A. Fig. 4.8 shows random variable power imported from wind farms C2 and D1 and from AC grid A. Converters Cb-B1, Cb-B2, and Cd-E1 share power according to the same sharing scheme as in the base case, 30%:30%:40%, respectively. The no-load voltage values of the droop controlled VSCs were calculated and updated every 1 second based on the droop gains listed in Table 4.3 at $V_{omax} = 0.95$ p.u. As can be seen in Fig. 4.9, the active power-sharing

among the output converters Cb-B1, Cb-B2, and Cd-E1 follows the desired percentage shares. At any instant, the sharing ratio is fixed, and because of transmission losses in the DC network, the total output power is slightly less than the total input power. The DC voltage level at all DC buses is within limits, as indicated in Fig. 4.10. These results show the effectiveness of the proposed control strategy in improving the accuracy of the power-sharing in the case of variable input power.

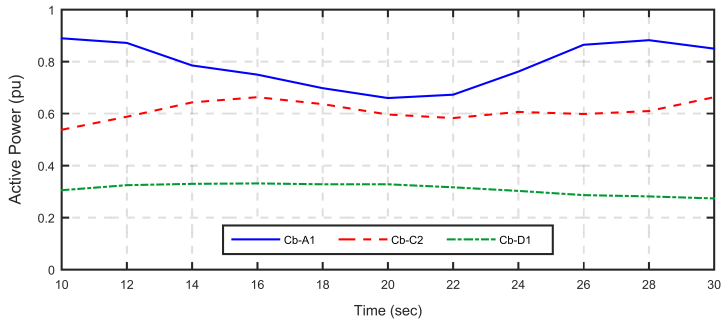

Figure 4.8: Variations in the input power.

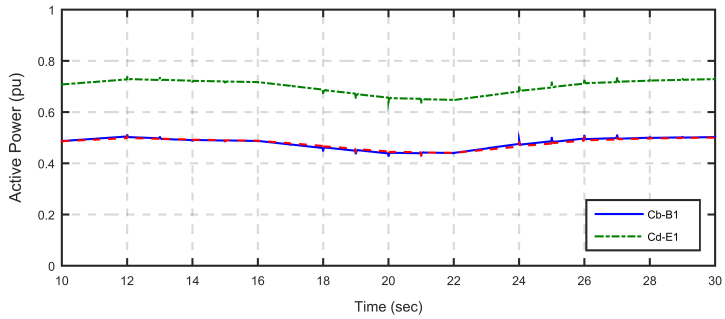

Figure 4.9: Power sharing between output converters.

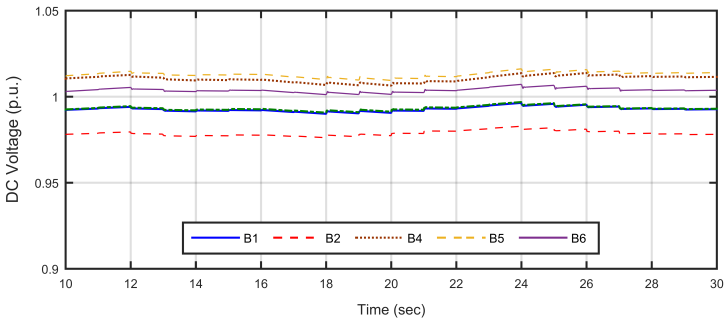

Figure 4.10: DC voltages of the buses with power variations.

4.4 Discussion

In this chapter, an OPF-based adaptive voltage-droop control strategy for power-sharing control, based on predefined desired power shares, and voltage regulation for MT VSC-HVDC based offshore wind farms integration system. The strategy has a two-layer hierarchal control structure, in which, the primary level of the power output converters, which share the incoming power, includes an adaptive voltage-droop controller. Where, the droop-gain and no-load voltage parameters are selected by the supervisory controller in order to achieve specific objectives: enhancing DC voltage dynamics and arriving at an accurate ratio for power-sharing control. To meet these objectives, an optimum droop-gain selection methodology, which includes consideration of the enhancement of DC voltage dynamics, was proposed as a means of improving the transient response of the DC voltage to changes in the input power without violating voltage limits. Optimal droop-reference voltages were then established by the proposed DC OPF-based power-sharing control algorithm. In all of the simulation results, the proposed control strategy determined an accurate ratio of power-sharing control, thus eliminating the drawbacks associated with conventional voltage-droop control. The proposed control strategy is used in controlling the steady state operation of the system. However, due the nonlinearity of the MT VSC-HVDC system and the change in the operating conditions, the VSC local controller parameters need to be tuned for optimal dynamic performance, which will be performed by the tuning methodology that is proposed in the next chapter.

Chapter 5

MT HVDC VSCs Local Controller Gains Tuning Methodology

5.1 Introduction

In this chapter, a tuning methodology is proposed for selecting the optimum local controller parameters of the VSCs in an offshore MT HVDC network to enhance the transient performance and the small-signal stability of the system. As part of the proposed methodology, the derivation of the aggregated linearized state-space model of a MT VSC-HVDC based offshore wind farm integration system is provided. Based on the derived model, a small-signal stability analysis is performed to show the modes interactions and define the dominant eigenvalues of the system. At the end of this chapter, the validation of the proposed methodology is performed by applying it to the Cigre B4 MT VSC-HVDC using Matlab/Simulink software.

5.2 MT VSC-HVDC Linearized State-Space Model

The linearized state-space model of the MT VSC-HVDC transmission system is derived from the dynamic equations of the system components and control system stated in chapter 3. To make the state-space system model generic and easy to be modified based according

to the system configuration, the system model is divided into multiple cascaded subsystems, as shown in Fig. 5.1. All VSCs has the same inner loop model, the differences between them are in the outer loop and the model of the connected grid.

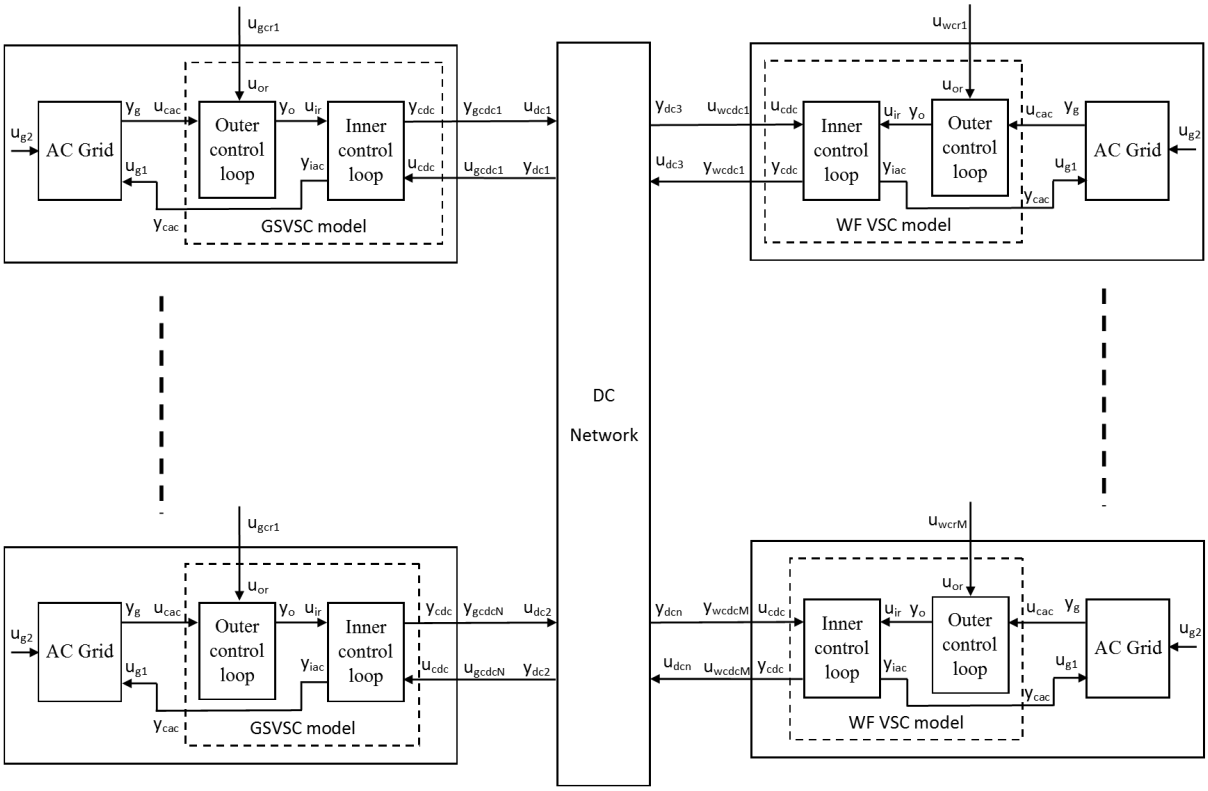

Figure 5.1: Linearized state-space model structure.

In this work, there are three types of outer control loops: rectification mode GS-VSC, inversion mode GS-VSC and the WF-VSC. The first type operates in constant power control mode, the second operates in droop control mode, and the third controls the AC voltage and frequency of the WF grid.

5.2.1 GS VSC linearized state-space model

Inner control loop and PLL

The inner control loop is common for all types of VSCs. In GS-VSC, the dynamics equations of the inner current control loop and the PLL are used to derive the linearized state-space model of the is subsystem. However, in WF-VSC, there is no PLL. Hence, only the inner loop dynamic equations are used in the inner loop subsystem model derivation.

GS-VSC inner loop State space model

By linearizing equations (3.5), (3.6), (3.8), (3.9), ((3.10) and (3.11), the inner loop plus PLL linearized model is derived to be as in (5.1):

$$\begin{aligned}
\Delta\dot{\boldsymbol{x_i}} &= \boldsymbol{A_i}\ \Delta\boldsymbol{x_i} + \boldsymbol{B_{i_{ac}}}\ \Delta\boldsymbol{u_{c_{ac}}} + \boldsymbol{B_{i_{dc}}}\ \Delta\boldsymbol{u_{c_{dc}}} + \boldsymbol{B_{i_r}}\ \Delta\boldsymbol{u_{i_r}} \\
\Delta\boldsymbol{y_{i_{ac}}} &= \boldsymbol{C_{i_{ac}}}\ \Delta\boldsymbol{x_i} + \boldsymbol{D_{i_{ac_1}}}\ \Delta\boldsymbol{u_{c_{ac}}} + \boldsymbol{D_{c_{dc_1}}}\ \Delta\boldsymbol{u_{i_{dc}}} + \boldsymbol{D_{i_{r_1}}}\ \Delta\boldsymbol{u_{i_r}} \\
\Delta\boldsymbol{y_{i_{dc}}} &= \boldsymbol{C_{i_{dc}}}\ \Delta\boldsymbol{x_i} + \boldsymbol{D_{i_{ac_2}}}\ \Delta\boldsymbol{u_{c_{ac}}} + \boldsymbol{D_{c_{dc_2}}}\ \Delta\boldsymbol{u_{i_{dc}}} + \boldsymbol{D_{i_{r_2}}}\ \Delta\boldsymbol{u_{i_r}}
\end{aligned} \tag{5.1}$$

where, $\Delta\boldsymbol{x}_i = \left[\Delta i_{f_d}\ \Delta i_{f_q}\ \Delta M_d\ \Delta M_q\ \Delta\theta_{pll}\ \Delta M_{pll}\right]^T$; $\Delta\boldsymbol{u}_{i_{ac}} = [\Delta i_{g_d}\ \Delta i_{g_q}\ \Delta u_{t_d}\ \Delta u_{t_q}]^T$; $\boldsymbol{u}_{i_{dc}} = [\Delta V_{dc}]$; $\Delta\boldsymbol{y}_{i_{ac}} = \left[\Delta i_{f_d}\ \Delta i_{f_q}\ \theta_{pll}\right]^T$; $\Delta\boldsymbol{y}_{i_{dc}} = [\Delta I_{dc}]$; and the state-space model matrices are as follows:

$$A_i = \begin{bmatrix}
\frac{-(R_f+K_{p_{in}})}{L_f} & 0 & \frac{1}{L_f} & 0 & 0 & 0 \\
0 & \frac{-(R_f+K_{p_{in}})}{L_f} & 0 & \frac{1}{L_f} & 0 & 0 \\
K_{i_{in}} & 0 & 0 & 0 & 0 & 0 \\
0 & K_{i_{in}} & 0 & 0 & 0 & 0 \\
0 & 0 & 0 & 0 & 0 & 1 \\
0 & 0 & 0 & 0 & 0 & 0
\end{bmatrix};$$

$$B_{i_{ac}} = \begin{bmatrix}
0 & 0 & 0 & 0 \\
0 & 0 & 0 & 0 \\
0 & 0 & 0 & 0 \\
0 & 0 & 0 & 0 \\
0 & 0 & 0 & K_{p_{pll}} \\
0 & 0 & 0 & K_{i_{pll}}
\end{bmatrix}; \quad B_{i_r} = \begin{bmatrix}
\frac{K_{p_{in}}}{L_f} & 0 \\
0 & \frac{K_{p_{in}}}{L_f} \\
K_{i_{in}} & 0 \\
0 & K_{i_{in}} \\
0 & 0 \\
0 & 0
\end{bmatrix}; \quad B_{i_{dc}} = \begin{bmatrix}
0 \\ 0 \\ 0 \\ 0 \\ 0 \\ 0
\end{bmatrix};$$

$$C_{i_{ac}} = \begin{bmatrix} 1 & 0 & 0 & 0 & 0 & 0 \\ 0 & 1 & 0 & 0 & 0 & 0 \\ 0 & 0 & 0 & 0 & 1 & 0 \end{bmatrix}; \qquad C_{i_{dc}} = \begin{bmatrix} \frac{1.5*u^o_{t_d}}{V^o_{dc}} & \frac{1.5*u^o_{t_q}}{V^o_{dc}} & 0 & 0 & 0 & 0 \end{bmatrix};$$

$$D_{i_{ac_1}} = \begin{bmatrix} 0 & 0 & 0 & 0 \\ 0 & 0 & 0 & 0 \\ 0 & 0 & 0 & 0 \end{bmatrix}; \qquad D_{i_{ac_2}} = \begin{bmatrix} 0 & 0 & 0 & 0 \end{bmatrix}; \qquad D_{i_{r_1}} = \begin{bmatrix} 0 & 0 \\ 0 & 0 \\ 0 & 0 \end{bmatrix};$$

$$D_{i_{r_2}} = \begin{bmatrix} 0 & 0 \end{bmatrix}; \qquad D_{i_{dc_1}} = \begin{bmatrix} 0 & 0 \end{bmatrix}; \qquad D_{i_{dc_2}} = \begin{bmatrix} \frac{1.5*(u^o_{t_d} i^o_{f_d} + u^o_{t_q} i^o_{f_q})}{V^o_{dc}} \end{bmatrix};$$

Outer control loop model

There are two types of outer control loops in GS-VSCs. For VSCs operate as rectifiers, the outer control loop controls the active and reactive power at constant reference values. However, for the outer control loops of the VSCs, operate as inverters, the active power reference is calculated by the droop equation (2.3).

The linearized state-space model of the outer loop is derived from the linearized equations of (3.14) to (3.17), and the state-space model is as follows:

$$\begin{aligned} \Delta \dot{\boldsymbol{x}}_o &= \boldsymbol{A}_o\ \Delta \boldsymbol{x}_o + \boldsymbol{B}_{o_{ac}}\ \Delta \boldsymbol{u}_{c_{ac}} + \boldsymbol{B}_{o_{dc}}\ \Delta \boldsymbol{u}_{c_{dc}} + \boldsymbol{B}_{o_r}\ \Delta \boldsymbol{u}_{i_r} \\ \Delta \boldsymbol{y}_o &= \boldsymbol{C}_o\ \Delta \boldsymbol{x}_o + \boldsymbol{D}_{o_{ac}}\ \Delta \boldsymbol{u}_{c_{ac}} + \boldsymbol{D}_{o_{dc}}\ \Delta \boldsymbol{u}_{i_{dc}} + \boldsymbol{D}_{o_r}\ \Delta \boldsymbol{u}_{o_r} \end{aligned} \tag{5.2}$$

where, $\Delta \boldsymbol{x}_o = [\Delta N_d / \Delta N_q]^T$;

$$A_o = \begin{bmatrix} 0 & 0 \\ 0 & 0 \end{bmatrix};$$

$$B_{o_{ac}} = \begin{bmatrix} -1.5K_{i_d} * u^o_{t_d} & -1.5K_{i_d} * u^o_{t_q} & -1.5K_{i_d} * i^o_{f_d} & -1.5K_{i_d} * i^o_{f_q} \\ 1.5K_{i_q} * u^o_{t_q} & -1.5K_{i_q} * u^o_{t_d} & -1.5K_{i_q} * i^o_{f_q} & 1.5K_{i_q} * i^o_{f_d} \end{bmatrix};$$

$$C_o = \begin{bmatrix} 1 & 0 \\ 0 & 1 \end{bmatrix};$$

$$D_{o_{ac}} = \begin{bmatrix} -1.5K_{p_d} * u^o_{t_d} & -1.5K_{p_d} * u^o_{t_q} & -1.5K_{p_d} * i^o_{f_d} & -1.5K_{p_d} * i^o_{f_q} \\ 1.5K_{p_q} * u^o_{t_q} & -1.5K_{p_q} * u^o_{t_d} & -1.5K_{p_q} * i^o_{f_q} & 1.5K_{p_q} * i^o_{f_d} \end{bmatrix};$$

In rectification mode VSC (constant power control)

$\boldsymbol{u}_{o_r} = [P^*\ Q^*]^T$

$$B_{o_r} = \begin{bmatrix} K_{i_d} & 0 \\ 0 & -K_{i_q} \end{bmatrix}; \quad B_{o_{dc}} = \begin{bmatrix} 0 \\ 0 \end{bmatrix};$$

$$D_{o_r} = \begin{bmatrix} K_{p_d} & 0 \\ 0 & -K_{p_q} \end{bmatrix}; \quad D_{o_{dc}} = \begin{bmatrix} 0 \\ 0 \end{bmatrix}.$$

In inversion mode VSC (droop control)

$\boldsymbol{u}_{o_r} = [Q^*]$

$$B_{o_r} = \begin{bmatrix} 0 \\ -K_{i_q} \end{bmatrix}; \quad B_{o_{dc}} = \begin{bmatrix} \frac{-K_{i_d}(2*V_d^o c - V_o)}{R_D} \\ 0 \end{bmatrix};$$

$$D_{o_r} = \begin{bmatrix} 0 \\ -K_{p_q} \end{bmatrix}; \quad B_{o_{dc}} = \begin{bmatrix} \frac{-K_{p_d}(2*V_d^o c - V_o)}{R_D} \\ 0 \end{bmatrix}.$$

The overall converter model

The overall converter model is derived by making $\Delta \boldsymbol{u}_{i_r} = \Delta \boldsymbol{y}_o$ with the substitution in (5.1). The overall converter model is as follows:

$$\begin{aligned} \Delta \dot{\boldsymbol{x}}_{\boldsymbol{c}} &= \boldsymbol{A_c}\ \Delta \boldsymbol{x_c} + \boldsymbol{B_{cac}}\ \Delta \boldsymbol{u_{cac}} + \boldsymbol{B_{cdc}}\ \Delta \boldsymbol{u_{cdc}} + \boldsymbol{B_{cr}}\ \Delta \boldsymbol{u_{cr}} \\ \Delta \boldsymbol{y_{cac}} &= \boldsymbol{C_{cac}}\ \Delta \boldsymbol{x_c} + \boldsymbol{D_{cac_1}}\ \Delta \boldsymbol{u_{cac}} + \boldsymbol{D_{cdc_1}}\ \Delta \boldsymbol{u_{cdc}} + \boldsymbol{D_{cr_1}}\ \Delta \boldsymbol{u_{ir}} \\ \Delta \boldsymbol{y_{cdc}} &= \boldsymbol{C_{cdc}}\ \Delta \boldsymbol{x_c} + \boldsymbol{D_{cac_2}}\ \Delta \boldsymbol{u_{cac}} + \boldsymbol{D_{cdc_2}}\ \Delta \boldsymbol{u_{cdc}} + \boldsymbol{D_{cr_2}}\ \Delta \boldsymbol{u_{cr}} \end{aligned} \tag{5.3}$$

$$A_c = \begin{bmatrix} A_i + B_{i_r} D_{o_{ac_1}} & B_{i_r} C_o \\ B_{o_{ac_1}} & A_o \end{bmatrix};$$

$$B_{c_{ac}} = \begin{bmatrix} B_{i_{ac}} + B_{i_r} D_{o_{ac}} \\ B_{o_{ac}} \end{bmatrix}; \quad B_{c_{dc}} = \begin{bmatrix} B_{i_{dc}} + B_{i_r} D_{o_{dc}} \\ B_{o_{dc}} \end{bmatrix}; \quad B_{c_r} = \begin{bmatrix} B_{i_r} D_{o_r} \\ B_{o_r} \end{bmatrix};$$

$$C_{c_{ac}} = \begin{bmatrix} C_{i_{ac}} + D_{i_{r_1}} D_{o_{ac}} & D_{i_{r_1}} C_o \end{bmatrix}; \quad C_{c_{dc}} = \begin{bmatrix} C_{i_{dc}} + D_{i_{r_2}} D_{o_{dc}} & D_{i_{r_2}} C_o \end{bmatrix};$$

$$D_{c_{ac_1}} = \begin{bmatrix} D_{i_{ac_1}} + D_{i_{r_1}} D_{o_{ac}} \end{bmatrix}; \quad D_{c_{dc_1}} = \begin{bmatrix} D_{i_{dc_1}} + D_{i_{r_1}} D_{o_{dc}} \end{bmatrix}; \quad D_{c_{r_1}} = \begin{bmatrix} D_{i_{r_1}} D_{o_r} \end{bmatrix};$$

$$D_{c_{ac_2}} = \begin{bmatrix} D_{i_{ac_2}} + D_{i_{r_2}} D_{o_{ac}} \end{bmatrix}; \quad D_{c_{dc_2}} = \begin{bmatrix} D_{i_{dc_2}} + D_{i_{r_2}} D_{o_{dc}} \end{bmatrix}; \quad D_{c_{r_2}} = \begin{bmatrix} D_{i_{r_2}} D_{o_r} \end{bmatrix};$$

The AC grid model

The AC grid model is derived from (3.25) to (3.30) after the linearization. Hence, the AC grid model is as follows:

$$\begin{aligned} \Delta\dot{\boldsymbol{x}}_g &= \boldsymbol{A}_g\ \Delta\boldsymbol{x}_g + \boldsymbol{B}_g\ \Delta\boldsymbol{u}_g \\ \Delta\boldsymbol{y}_g &= \boldsymbol{C}_g\ \Delta\boldsymbol{x}_g \end{aligned} \tag{5.4}$$

where $\Delta\boldsymbol{x}_g = [\Delta i_{g_d}\ \Delta i_{g_q}\ \Delta u_{t_d}\ \Delta u_{t_q}]^T$; $\Delta\boldsymbol{u}_g = \Delta\boldsymbol{y}_{c_{ac}}$; and the state-space model matrices are as follows:

$$A_g = \begin{bmatrix} \frac{-R_g}{L_g} & \omega & \frac{-1}{L_g} & 0 \\ -\omega & \frac{-R_g}{L_g} & 0 & \frac{-1}{L_g} \\ \frac{1}{C_f} & 0 & 0 & \omega \\ 0 & \frac{1}{C_f} & -\omega & 0 \end{bmatrix};$$

$$B_g = \begin{bmatrix} 0 & 0 & -\Delta\hat{U}_g^o cos(\delta^o)sin(theta^o) + \Delta\hat{U}_g^o cos(\delta^o)cos(theta^o) \\ 0 & 0 & -\Delta\hat{U}_g^o cos(\delta^o)sin(theta^o) + \Delta\hat{U}_g^o cos(\delta^o)cos(theta^o) \\ -\frac{1}{C_f} & 0 & 0 \\ 0 & -\frac{1}{C_f} & 0 \end{bmatrix};$$

$$C_g = \begin{bmatrix} 1 & 0 & 0 & 0 \\ 0 & 1 & 0 & 0 \\ 0 & 0 & 1 & 0 \\ 0 & 0 & 0 & 1 \end{bmatrix};$$

The combined state-space model of the GS-VSC and the connected AC grid

The system below, in (5.5), shows the linearized state-space model of a GS-VSC terminal (combined state-space model of the GS-VSC and the connected AC grid):

$$\begin{aligned} \Delta\dot{\boldsymbol{x}}_{\boldsymbol{gc}} &= \boldsymbol{A}_{gc}\ \Delta\boldsymbol{x}_{gc} + \boldsymbol{B}_{gc_{dc}}\ \Delta\boldsymbol{u}_{c_{dc}} + \boldsymbol{B}_{gc_r}\ \Delta\boldsymbol{u}_{\boldsymbol{gr_r}} \\ \Delta\boldsymbol{y}_{gc_{dc}} &= \boldsymbol{C}_{gc_{dc}}\ \Delta\boldsymbol{x}_{gc} +\ \boldsymbol{D}_{gc_{dc}}\ \Delta\boldsymbol{u}_{gc_{dc}} + \boldsymbol{D}_{gc_r}\ \Delta\boldsymbol{u}_{gc_r} \end{aligned} \tag{5.5}$$

where, $\Delta \boldsymbol{x_{gc}} = [\Delta \boldsymbol{x}_c \ \Delta \boldsymbol{x}_g]^T$; $\Delta \boldsymbol{y}_{gc_{dc}} = [\Delta I_{dc}]$; $\Delta \boldsymbol{u}_{gc_{dc}} = [\Delta V_{dc}]$; $\Delta \boldsymbol{u}_{gc_r} = [\Delta P^* \ \Delta Q^*]^T$ (for the constant P controlled GS-VSC) or $\Delta \boldsymbol{u}_{gc_r} = [\Delta Q^*]^T$ (for droop controlled GS-VSC); and the state-space model matrices are as follows:

$$A_{gc} = \begin{bmatrix} A_c & B_{c_{ac}} C_g \\ B_g C_{c_{ac}} & A_g + B_g D_{c_{ac_1}} C_g \end{bmatrix};$$

$$B_{gc_{dc}} = \begin{bmatrix} B_{c_{dc}} \\ B_g \ D_{c_{dc_1}} \end{bmatrix}; \quad B_{gc_r} = \begin{bmatrix} B_{c_r} \\ B_g \ D_{c_{r_1}} \end{bmatrix};$$

$$C_{gc_{dc}} = \begin{bmatrix} C_{c_{dc}} & 0_{1\times 4} \end{bmatrix}; \quad D_{gc_{dc}} = \begin{bmatrix} D_{c_{dc_2}} \end{bmatrix}; \quad D_{gc_r} = \begin{bmatrix} D_{c_{r_2}} \end{bmatrix}.$$

5.2.2 WF-VSC linearized state-space model

Inner control loop model

In the WF-VSC, there is no PLL. Therefore, equations (3.5), (3.6), ((3.10) and (3.11) are used to derive the inner loop linearized model in (5.6):

$$\begin{aligned} \Delta \dot{\boldsymbol{x_i}} &= \boldsymbol{A_i} \ \Delta \boldsymbol{x_i} + \boldsymbol{B_{i_{ac}}} \ \Delta \boldsymbol{u_{c_{ac}}} + \boldsymbol{B_{i_{dc}}} \ \Delta \boldsymbol{u_{c_{dc}}} + \boldsymbol{B_{i_r}} \ \Delta \boldsymbol{u_{i_r}} \\ \Delta \boldsymbol{y_{i_{ac}}} &= \boldsymbol{C_{i_{ac}}} \ \Delta \boldsymbol{x_i} + \boldsymbol{D_{i_{ac_1}}} \ \Delta \boldsymbol{u_{c_{ac}}} + \boldsymbol{D_{c_{dc_1}}} \ \Delta \boldsymbol{u_{i_{dc}}} + \boldsymbol{D_{i_{r_1}}} \ \Delta \boldsymbol{u_{i_r}} \\ \Delta \boldsymbol{y_{i_{dc}}} &= \boldsymbol{C_{i_{dc}}} \ \Delta \boldsymbol{x_i} + \boldsymbol{D_{i_{ac_2}}} \ \Delta \boldsymbol{u_{c_{ac}}} + \boldsymbol{D_{c_{dc_2}}} \ \Delta \boldsymbol{u_{i_{dc}}} + \boldsymbol{D_{i_{r_2}}} \ \Delta \boldsymbol{u_{i_r}} \end{aligned} \tag{5.6}$$

where, $\Delta \boldsymbol{x}_i = [\Delta i_{f_d} \ \Delta i_{f_q} \ \Delta M_d \ \Delta M_q]^T$; $\Delta \boldsymbol{u}_{i_{ac}} = [\Delta i_{g_d} \ \Delta i_{g_q} \ \Delta u_{t_d} \ \Delta u_{t_q}]^T$; $\boldsymbol{u}_{i_{dc}} = [\Delta V_{dc}]$; $\Delta \boldsymbol{y}_{i_{ac}} = \begin{bmatrix} \Delta i_{f_d} \ \Delta i_{f_q} \ \theta_{pll} \end{bmatrix}^T$; $\Delta \boldsymbol{y}_{i_{dc}} = [\Delta I_{dc}]$; and the state-space model matrices are as follows:

$$A_i = \begin{bmatrix} \frac{-(R_f + K_{p_{in}})}{L_f} & 0 & \frac{1}{L_f} & 0 \\ 0 & \frac{-(R_f + K_{p_{in}})}{L_f} & 0 & \frac{1}{L_f} \\ K_{i_{in}} & 0 & 0 & 0 \\ 0 & K_{i_{in}} & 0 & 0 \end{bmatrix};$$

$$B_{i_{ac}} = \begin{bmatrix} 0 & 0 & 0 & 0 \\ 0 & 0 & 0 & 0 \\ 0 & 0 & 0 & 0 \\ 0 & 0 & 0 & 0 \end{bmatrix}; \quad B_{i_r} = \begin{bmatrix} \frac{K_{p_{in}}}{L_f} & 0 \\ 0 & \frac{K_{p_{in}}}{L_f} \\ K_{i_{in}} & 0 \\ 0 & K_{i_{in}} \end{bmatrix}; \quad B_{i_{dc}} = \begin{bmatrix} 0 \\ 0 \\ 0 \\ 0 \end{bmatrix};$$

$$C_{i_{ac}} = \begin{bmatrix} 1 & 0 & 0 & 0 \\ 0 & 1 & 0 & 0 \end{bmatrix}; \qquad C_{i_{dc}} = \begin{bmatrix} \frac{1.5*u^o_{i_d}}{V^o_{dc}} & \frac{1.5*u^o_{tq}}{V^o_{dc}} & 0 & 0 \end{bmatrix};$$

$$D_{i_{ac_1}} = \begin{bmatrix} 0 & 0 & 0 & 0 \\ 0 & 0 & 0 & 0 \end{bmatrix}; \qquad D_{i_{ac_2}} = \begin{bmatrix} 0 & 0 & 0 & 0 \end{bmatrix}; \qquad D_{i_{r_1}} = \begin{bmatrix} 0 & 0 \\ 0 & 0 \end{bmatrix};$$

$$D_{i_{r_2}} = \begin{bmatrix} 0 & 0 \end{bmatrix}; \qquad D_{i_{dc_1}} = \begin{bmatrix} 0 & 0 \end{bmatrix}; \qquad D_{i_{dc_2}} = \begin{bmatrix} \frac{1.5*(u^o_{t_d} i^o_{f_d} + u^o_{t_q} i^o_{f_q})}{V^o_{dc}} \end{bmatrix};$$

Outer control loop

The outer control loop of the WF-VSCs controls the AC voltage at PCC. Thereby, The linearized state-space model of the outer loop is derived from the linearized equations of (3.20) to (3.23) to be as follows:

$$\begin{aligned} \Delta \dot{\boldsymbol{x}}_o &= \boldsymbol{A}_o \Delta \boldsymbol{x}_o + \boldsymbol{B}_{o_{ac}}\, \Delta \boldsymbol{u}_{c_{ac}} + \boldsymbol{B}_{o_{dc}}\, \Delta \boldsymbol{u}_{c_{dc}} + \boldsymbol{B}_{o_r}\, \Delta \boldsymbol{u}_{i_r} \\ \Delta \boldsymbol{y}_o &= \boldsymbol{C}_o\, \Delta \boldsymbol{x}_o + \boldsymbol{D}_{o_{ac}}\, \Delta \boldsymbol{u}_{c_{ac}} + \boldsymbol{D}_{o_{dc}}\, \Delta \boldsymbol{u}_{i_{dc}} + \boldsymbol{D}_{o_r}\, \Delta \boldsymbol{u}_{o_r} \end{aligned} \tag{5.7}$$

where, $\Delta \boldsymbol{x}_o = [\Delta N_d / \Delta N_q]^T$; $\Delta \boldsymbol{u}_{o_r} = [\Delta u^*_{t_d}] \;\; \Delta u^*_{t_q}]^T$; and the matrices are as follows:

$$A_o = \begin{bmatrix} 0 & 0 \\ 0 & 0 \end{bmatrix};$$

$$B_{o_{ac}} = \begin{bmatrix} 0 & 0 & K_{i_o} & 0 \\ 0 & 0 & 0 & K_{i_o} \end{bmatrix}; \quad B_{o_r} = \begin{bmatrix} -K_{i_o} & 0 \\ 0 & -K_{i_0} \end{bmatrix}; \quad B_{o_{dc}} = \begin{bmatrix} 0 \\ 0 \end{bmatrix};$$

$$C_o = \begin{bmatrix} 1 & 0 \\ 0 & 1 \end{bmatrix};$$

$$D_{o_{ac}} = \begin{bmatrix} 1 & 0 & K_{p_o} & \omega C_f \\ 0 & 1 & -\omega C_f & K_{p_o} \end{bmatrix};$$

$$D_{o_r} = \begin{bmatrix} -K_{p_o} & 0 \\ 0 & -K_{p_o} \end{bmatrix}; \quad D_{o_{dc}} = \begin{bmatrix} 0 \\ 0 \end{bmatrix}.$$

The overall WF converter model

The overall converter model is derived by making $\Delta \boldsymbol{u}_{i_r} = \Delta \boldsymbol{y}_o$ with the substitution in (5.8):

$$\begin{aligned}
\Delta \dot{\boldsymbol{x}}_{\boldsymbol{c}} &= \boldsymbol{A_c}\ \Delta \boldsymbol{x_c} + \boldsymbol{B}_{\boldsymbol{c_{ac}}}\ \Delta \boldsymbol{u}_{\boldsymbol{c_{ac}}} + \boldsymbol{B}_{\boldsymbol{c_{dc}}}\ \Delta \boldsymbol{u}_{\boldsymbol{c_{dc}}} + \boldsymbol{B}_{\boldsymbol{c_r}}\ \Delta \boldsymbol{u}_{\boldsymbol{c_r}} \\
\Delta \boldsymbol{y}_{\boldsymbol{c_{ac}}} &= \boldsymbol{C}_{\boldsymbol{c_{ac}}}\ \Delta \boldsymbol{x_c} + \boldsymbol{D}_{\boldsymbol{c_{ac_1}}}\ \Delta \boldsymbol{u}_{\boldsymbol{c_{ac}}} + \boldsymbol{D}_{\boldsymbol{c_{dc_1}}}\ \Delta \boldsymbol{u}_{\boldsymbol{c_{dc}}} + \boldsymbol{D}_{\boldsymbol{c_{r_1}}}\ \Delta \boldsymbol{u}_{\boldsymbol{i_r}} \\
\Delta \boldsymbol{y}_{\boldsymbol{c_{dc}}} &= \boldsymbol{C}_{\boldsymbol{c_{dc}}}\ \Delta \boldsymbol{x_c} + \boldsymbol{D}_{\boldsymbol{c_{ac_2}}}\ \Delta \boldsymbol{u}_{\boldsymbol{c_{ac}}} + \boldsymbol{D}_{\boldsymbol{c_{dc_2}}}\ \Delta \boldsymbol{u}_{\boldsymbol{c_{dc}}} + \boldsymbol{D}_{\boldsymbol{c_{r_2}}}\ \Delta \boldsymbol{u}_{\boldsymbol{c_r}}
\end{aligned} \tag{5.8}$$

$$A_c = \begin{bmatrix} A_i + B_{i_r} D_{o_{ac_1}} & B_{i_r} C_o \\ B_{o_{ac_1}} & A_o \end{bmatrix};$$

$$B_{c_{ac}} = \begin{bmatrix} B_{i_{ac}} + B_{i_r} D_{o_{ac}} \\ B_{o_{ac}} \end{bmatrix}; \quad B_{c_{dc}} = \begin{bmatrix} B_{i_{dc}} + B_{i_r} D_{o_{dc}} \\ B_{o_{dc}} \end{bmatrix}; \quad B_{c_r} = \begin{bmatrix} B_{i_r} D_{o_r} \\ B_{o_r} \end{bmatrix};$$

$$C_{c_{ac}} = \begin{bmatrix} C_{i_{ac}} + D_{i_{r_1}} D_{o_{ac}} & D_{i_{r_1}} C_o \end{bmatrix}; \quad C_{c_{dc}} = \begin{bmatrix} C_{i_{dc}} + D_{i_{r_2}} D_{o_{dc}} & D_{i_{r_2}} C_o \end{bmatrix};$$

$$D_{c_{ac_1}} = \begin{bmatrix} D_{i_{ac_1}} + D_{i_{r_1}} D_{o_{ac}} \end{bmatrix}; \quad D_{c_{dc_1}} = \begin{bmatrix} D_{i_{dc_1}} + D_{i_{r_1}} D_{o_{dc}} \end{bmatrix}; \quad D_{c_{r_1}} = \begin{bmatrix} D_{i_{r_1}} D_{o_r} \end{bmatrix};$$

$$D_{c_{ac_2}} = \begin{bmatrix} D_{i_{ac_2}} + D_{i_{r_2}} D_{o_{ac}} \end{bmatrix}; \quad D_{c_{dc_2}} = \begin{bmatrix} D_{i_{dc_2}} + D_{i_{r_2}} D_{o_{dc}} \end{bmatrix}; \quad D_{c_{r_2}} = \begin{bmatrix} D_{i_{r_2}} D_{o_r} \end{bmatrix};$$

The AC grid model

As the feed-forward part of the outer loop is used to fully decouple the dynamics of the VSC from the dynamics of the WF, The WF AC grid model by only the AC filter dynamic equations (3.27) and (3.28) only. These equations after the linearization are used to drive the state-space model of the WF grid to be as in (5.9).

$$\begin{aligned}
\Delta \dot{\boldsymbol{x}}_g &= \boldsymbol{A}_g\ \Delta \boldsymbol{x}_g + \boldsymbol{B}_{g_1}\ \Delta \boldsymbol{u}_{g_1}\ + \boldsymbol{B}_{g_2}\ \Delta \boldsymbol{u}_{g_2} \\
\Delta \boldsymbol{y}_g &= \boldsymbol{C}_g\ \Delta \boldsymbol{x}_g\ + \boldsymbol{D}_g\ \Delta \boldsymbol{u}_{g_1}
\end{aligned} \tag{5.9}$$

where $\Delta \boldsymbol{x}_g = [\ \Delta u_{t_d}\ \Delta u_{t_q}]^T$; $\Delta \boldsymbol{u}_{g_1} = \Delta \boldsymbol{y}_{c_{ac}}$; $\Delta \boldsymbol{u}_{g_2}[\Delta i_{g_d}\ \Delta i_{g_q}]^T$; and the state-space model matrices are as follows:

$$A_g = \begin{bmatrix} 0 & \omega \\ -\omega & 0 \end{bmatrix};$$

$$B_{g_1} = \begin{bmatrix} -\frac{1}{C_f} & 0 \\ 0 & -\frac{1}{C_f} \end{bmatrix}; \quad B_{g_2} = \begin{bmatrix} \frac{1}{C_f} & 0 \\ 0 & \frac{1}{C_f} \end{bmatrix};$$

$$C_g = \begin{bmatrix} 0 & 0 \\ 0 & 0 \\ 1 & 0 \\ 0 & 1 \end{bmatrix};$$

$$D_g = \begin{bmatrix} 1 & 0 \\ 0 & 1 \\ 0 & 0 \\ 0 & 0 \end{bmatrix};$$

The combined state-space model of the WF-VSC and the connected WF grid

The system below in (5.10) shows the linearized state-space model of a WF-VSC terminal (combined state-space model of the WF-VSC and the connected WF grid):

$$\begin{aligned} \Delta \dot{\boldsymbol{x}}_{\boldsymbol{wc}} &= \boldsymbol{A}_{wc}\ \Delta \boldsymbol{x}_{wc} + \boldsymbol{B}_{wc_{dc}}\ \Delta \boldsymbol{u}_{c_{dc}} + \boldsymbol{B}_{wc_r}\ \Delta \boldsymbol{u}_{\boldsymbol{wc_r}} \boldsymbol{B}_{wc_{ac}}\ \Delta \boldsymbol{u}_{\boldsymbol{wc_{ac}}} \\ \Delta \boldsymbol{y}_{wc_{dc}} &= \boldsymbol{C}_{wc_{dc}}\ \Delta \boldsymbol{x}_{wc} + \ \boldsymbol{D}_{wc_{dc}}\ \Delta \boldsymbol{u}_{wc_{dc}} + \boldsymbol{D}_{wc_r}\ \Delta \boldsymbol{u}_{wc_r} + \boldsymbol{D}_{wc_{ac}}\ \Delta \boldsymbol{u}_{wc_{ac}} \end{aligned} \tag{5.10}$$

where, $\Delta \boldsymbol{x}_{wc} = [\Delta \boldsymbol{x}_c\ \Delta \boldsymbol{x}_g]^T$; $\Delta \boldsymbol{y}_{wc_{dc}} = [\Delta I_{dc}]$; $\Delta \boldsymbol{u}_{wc_{dc}} = [\Delta V_{dc}]$; $\Delta \boldsymbol{u}_{wc_r} = [\Delta u^*_{t_d}\ \Delta u^*_{t_q}]^T$; and the state-space model matrices are as follows:

$$A_{wc} = \begin{bmatrix} A_c & B_{c_{ac}} C_g \\ B_g C_{c_{ac}} & A_g + B_g D_{c_{ac_1}} C_g \end{bmatrix};$$

$$B_{wc_{dc}} = \begin{bmatrix} B_{c_{dc}} \\ B_g\ D_{c_{dc_1}} \end{bmatrix}; \quad B_{wc_r} = \begin{bmatrix} B_{c_r} \\ B_g\ D_{c_{r_1}} \end{bmatrix}; \quad B_{wc_{ac}} = \begin{bmatrix} B_{c_{g_1}} \\ B_g\ D_{c_{g_1}} \end{bmatrix};$$

$$C_{wc_{dc}} = \begin{bmatrix} C_{c_{dc}} & 0_{1\times 4} \end{bmatrix}; \quad D_{wc_{dc}} = \begin{bmatrix} D_{c_{dc_2}} \end{bmatrix}; \quad D_{wc_r} = \begin{bmatrix} D_{c_{r_2}} \end{bmatrix}.$$

5.2.3 DC grid linearized state-space model

The linearized state-space model of the DC grid is derived from the dynamic equation of the DC lines (3.31) and the DC buses (3.31). For two terminal HVDC system connecting

one wind farm, at bus 2, to one AC grid, at bus 1, the linearized model is as shown in (5.11):

$$\begin{aligned} \Delta\dot{\boldsymbol{x}}_{\boldsymbol{dc}} &= \boldsymbol{A}_{dc}\ \Delta\boldsymbol{x}_{dc} + \boldsymbol{B}_{dc_1}\ \Delta\boldsymbol{u}_{dc_1} + \boldsymbol{B}_{dc_2}\ \Delta\boldsymbol{u}_{\boldsymbol{dc_2}} \\ \Delta\boldsymbol{y}_{dc_1} &= \boldsymbol{C}_{dc_1}\ \Delta\boldsymbol{x}_{dc} \\ \Delta\boldsymbol{y}_{dc_2} &= \boldsymbol{C}_{dc_2}\ \Delta\boldsymbol{x}_{dc} \end{aligned} \tag{5.11}$$

where $\Delta\boldsymbol{x}_{dc} = [\Delta I_{12}\ \Delta V_{dc_1}\ \Delta V_{dc_2}]^T$; $\Delta\boldsymbol{u}_{dc_1} = \Delta I_{dc_1}$; $\Delta\boldsymbol{u}_{dc_2} = \Delta I_{dc_2}$; $\Delta\boldsymbol{y}_{dc_1} = \Delta V_{dc_1}$; $\Delta\boldsymbol{y}_{dc_1} = \Delta V_{dc_1}$ and the model matrices are

$$A_{dc} = \begin{bmatrix} \frac{-R_{12}}{L_{12}} & \frac{-1}{L_{12}} & \frac{1}{L_{12}} \\ \frac{1}{C_1} & 0 & 0 \\ \frac{-1}{C_2} & 0 & 0 \end{bmatrix};$$

$$B_{dc_1} = \begin{bmatrix} 0 \\ \frac{1}{C_1} \\ 0 \end{bmatrix}; \quad B_{dc_1} = \begin{bmatrix} 0 \\ 0 \\ \frac{1}{C_2} \end{bmatrix};$$

$$C_{dc_1} = \begin{bmatrix} 0 & 1 & 0 \end{bmatrix}; \quad C_{dc_2} = \begin{bmatrix} 0 & 0 & 1 \end{bmatrix};$$

5.2.4 Overall linearized state-space model of a MT VSC-HVDC transmission system

The overall linearized state-space model of a MT VSC-HVDC system is built by performing $\Delta\boldsymbol{u}_{dc_i} = \Delta\boldsymbol{y}_{gc_i}$ at the grid side terminal bus i and $\Delta\boldsymbol{u}_{dc_j} = \Delta\boldsymbol{y}_{gc_;}$ at the wind farm terminal bus j. Hence, the model will be as in (5.12):

$$\begin{aligned} \Delta\dot{\boldsymbol{x}}_{\boldsymbol{sys}} &= \boldsymbol{A}_{sys}\ \Delta\boldsymbol{x}_{sys} + \boldsymbol{B}_{sys}\ \Delta\boldsymbol{u}_{sys} \\ \Delta\boldsymbol{y}_{sys} &= \boldsymbol{C}_{sys}\ \Delta\boldsymbol{x}_{sys} \end{aligned} \tag{5.12}$$

For the n terminals system with N GS-VSCs and M WF-VSCs, the vector of the system state variables $\Delta\boldsymbol{x}_{sys} = [\Delta\boldsymbol{x}_{gc_1}...\Delta\boldsymbol{x}_{gc_N}\ \Delta\boldsymbol{x}_{wc_1}...\Delta\boldsymbol{x}_{wc_M}\ \Delta\boldsymbol{x}_{dc}]^T$; the system inputs $\Delta\boldsymbol{u}_{sys} = [\Delta\boldsymbol{u}_{gc_{r_1}}...\Delta\boldsymbol{x}_{gc_{r_N}}\ \Delta\boldsymbol{u}_{wc_{r_1}}...\Delta\boldsymbol{u}_{wc_{r_M}}\ \ \Delta\boldsymbol{u}_{wc_{ac_1}}...\Delta\boldsymbol{u}_{wc_{ac_M}}]^T$. The state matrix and input matrix are as follows:

$$A_{sys} = \begin{bmatrix} A_{gc_1} & .. & 0_{12\times12} & 0_{12\times8} & .. & 0_{12\times8} & Bgc_{dc_1}Cdc_1 \\ : & : & : & : & : & : & : \\ 0_{12\times12} & .. & A_{gc_N} & 0_{12\times8} & .. & 0_{12\times8} & Bgc_{dc_M}Cdc_N \\ 0_{8\times12} & .. & 0_{8\times12} & A_{wc_1} & .. & 0_{8\times8} & Bwc_{dc_1}Cdc_{N+1} \\ : & .. & : & : & : & : & : \\ 0_{8\times12} & .. & 0_{8\times12} & 0_{8\times8} & .. & A_{wc_M} & Bwc_{dc_M}Cdc_{N+M} \\ B_{dc_1}Cgc_{dc_1} & .. & B_{dc_1}Cgc_{dc_1} & B_{dc_{N+1}}Cwc_{dc_1} & .. & B_{dc_{N+M}}Cwc_{dc_M} & ADC \end{bmatrix};$$

where $ADC = A_{dc} + B_{dc_1}Dgc_{dc_1}Cdc_1 + .. + B_{dc_N}Dgc_{dc_N}Cdc_N + B_{dc_{N+1}}Dwc_{dc_1}Cdc_{N+1} + .. + B_{dc_{N+M}}Dgc_{dc_M}Cdc_{N+M}$; and

$$B_{sys} = \begin{bmatrix} B_{gc_{r_1}} & .. & 0_{12\times1} & 0_{12\times2} & .. & 0_{12\times2} & 0_{12\times2} & 0_{12\times2} \\ : & : & : & : & : & : & : & : \\ 0_{12\times1} & .. & B_{gc_{r_N}} & 0_{12\times2} & .. & 0_{12\times2} & 0_{12\times2} & 0_{12\times2} \\ 0_{8\times1} & .. & 0_{8\times1} & B_{wc_{r_1}} & .. & 0_{8\times2} & 0_{8\times2} & 0_{8\times2} \\ : & .. & : & : & : & : & : & : \\ 0_{8\times1} & .. & 0_{8\times1} & 0_{8\times2} & .. & B_{wc_{r_1}} & 0_{8\times2} & 0_{8\times2} \\ 0_{8\times1} & .. & 0_{8\times1} & 0_{8\times2} & .. & 0_{8\times2} & B_{wc_{ac_1}} & 0_{8\times2} \\ : & : & .. & : & : & : & : & : \\ 0_{8\times1} & .. & 0_{8\times1} & 0_{8\times2} & .. & 0_{8\times2} & 0_{8\times2} & B_{wc_{ac_M}} \end{bmatrix};$$

The previously explained linearized state-space model of the MT VSC-HVDC system is used to build the test system linearized model, and its transfer matrix A_{sys} is used in the proposed tuning methodology and the small-signal analysis in the next sections.

5.3 Proposed VSCs Local Controller Parameters Tuning Methodology

Tuning the VSCs local controller gains, in a MT-HVDC based offshore wind farm integration system, is a challenging task, since a change in the system operating condition may lead to instability at a certain set of gains. The conventional tuning methods either adjust the control gains based on a tedious trial and error method, or utilize the pole placement

technique, which ignores the overall dynamics of the system or interactions between the system components. Thus, the VSCs local controller gains should be tuned to mitigate the change of the operating conditions.

This section illustrates methodology for tuning the VSCs' local controller gains at every scheduled change in the operating conditions [**?**]. The proposed methodology is performed by the central controller in multiple steps as follows:

1- For every change in the input power to the MT VSC-HVDC system the OPF based power sharing and voltage regulation controls strategy (chapter 4) is executed for selecting the droop parameters of the droop controlled VSCs. Based on the new droop parameters and input power, the new operating conditions are calculated.

2- The new operating conditions are substituted in the state matrix A_{sys} of system linearized state-space model.

3- The optimal parameters of the VSCs local controller are selected by an optimization algorithms to minimize the real part of the dominant eigenvalues and maximize their damping ratio to maximize the system bandwidth and damping.

4- The optimal parameters are sent to the system VSCs local controllers along with the optimal droop parameters.

The optimal VSCs local controller selection algorithm

The new optimal gains selection algorithm can be proposed to optimally select the VSCs local controller gains. The optimal gains are selected to maximize the system bandwidth and improve the system damping. Therefore, optimization problem is formulated, as follows:

The objective function is minimizing the real part of $\hat{\sigma}$ the state matrix A_{sys} dominant eigenvalue $\hat{\lambda}$ is shown in (5.13) as follows:

$$\min_{K}(F_1(K) = \hat{\sigma}) \tag{5.13}$$

subjected to the lower and upper limits constraints of K as follows:

$$K_l \geq \ K \ \leq K_u \tag{5.14}$$

where the gain vector $K = [K_{g_1}..K_{g_N} \ K_{w_1}..K_{w_M}]$; $K_{g_i} = [K_{p_{in}} K_{i_{in}} K_{p_d} K_{i_d} K_{p_q} K_{i_q} K_{p_{pll}} K_{i_{pll}}]$ $(\forall i \in N)$ is the gains vector of the i^{th} GS-VSC; and $K_{w_j} = [K_{p_{in}} K_{i_{in}} K_{p_o} K_{i_o}]$ $(\forall i \in M)$ is the gains vector of the j^{th} WS-VSC.

From the state matrix of the overall state-space matrix, the eigenvalues of the system Λ is calculated, and real part of the dominant pole $\hat{\sigma}$ is calculated by:

$$\hat{\sigma} = max(\Sigma) \tag{5.15}$$

where $\Sigma = \{\sigma_i, \sigma_i = Re(\lambda_i)\}, \forall \lambda_i \in \Lambda$.

The other objective is maximizing the damping of the system by maximizing the damping ratio $\hat{\zeta}$ of the dominant pole $\hat{\lambda}$.

$$\max_K (F_2(K) = \hat{\zeta}) \tag{5.16}$$

and

$$\hat{\zeta} = \left| \frac{\hat{\sigma}}{\hat{\lambda}} \right| \tag{5.17}$$

To combine the two objective functions, $F_1(K)$ and $F_2(K)$, in one optimization problem using the ϵ-constraint method employed [77]. The main advantage of this method is that it can identify a Pareto-optimal region regardless of whether the objective space is convex, non-convex, or discrete. Hence, it can solve the problem considering one of the objectives while limiting the remaining objectives within specific bounds. Hence, the second objective function $F_2(K)$ can be used as a soft constraint as follows:

$$F_2(K) - \epsilon > 0 \tag{5.18}$$

where ϵ is considered to limit the damping ratio to a value less than that maximally obtained from the Pareto front.

5.4 Time Domain Validation of The Proposed Methodology of Tuning the VSCs Local Controller Parameters

The modified Cigre B4 MT HVDC test system (Fig. 4.3), with the system parameters in Table 4.1 and Table 4.2, is used to validate the proposed tuning methodology. First, the linearized state-space model of the overall system is derived using steps in section 5.2. The linearized state-space model is verified and analyzed in subsection 5.4.1.

5.4.1 MT VSC-HVDC linearized state-space model verification and small-signal stability analysis

Time domain verification

The time domain verification of the linearized model (index "lin") is verified against the nonlinear model of the test system using MATLAB/Simulink SimPowerSystems. The inner control loop gains of the system VSCs have been tuned to have an equivalent time constant of 5 ms. The outer loop gains are selected in order to have a time constant 10 times of the inner loops. The droop gains of droop controlled VSCs are set at $R_D = 14\Omega$ (0.05 p.u.), with no load voltage $V_o = 400KV$. Fig. 5.2 and Fig. 5.3 show the responses of the linearized model compared to the time-domain nonlinear model to a 10% step rise in the wind power generation of WF-C and WF-D. The two wind farms were operating at 90% of their rated power before the step rise in their generation, while the VSC cb-A1 was injecting 50% on its rated power.

(a)

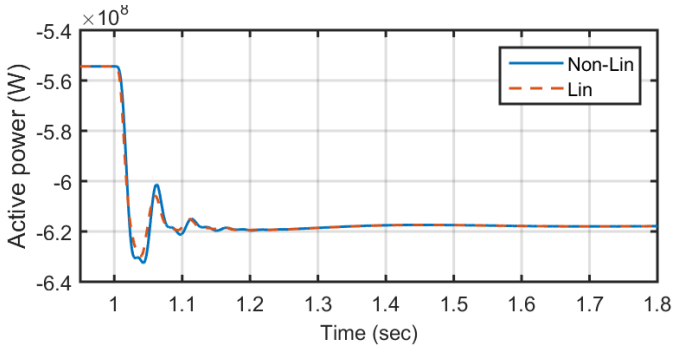

(b)

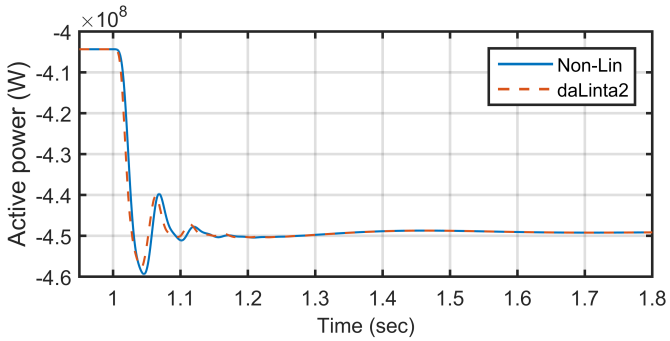

(c)

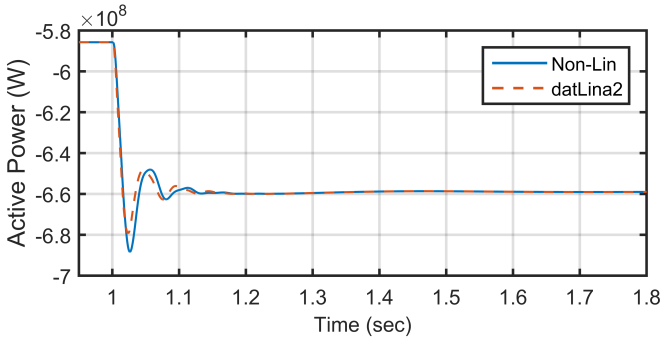

Figure 5.2: Active power response of the linearized model "Lin" and the time-domain nonlinear model "Non-Lin" of the VSCs at (a) bus 1 , (b)bus 2 and (c) bus 3.

(a)

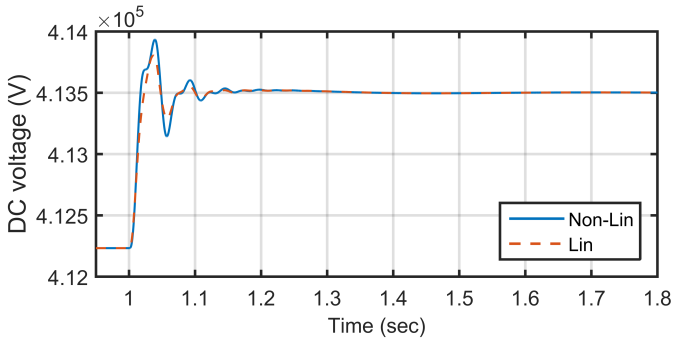

(b)

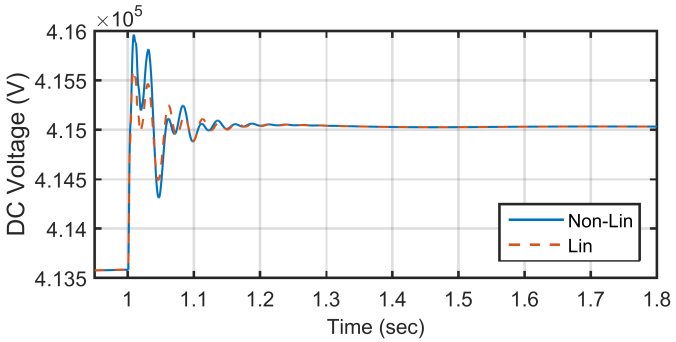

(c)

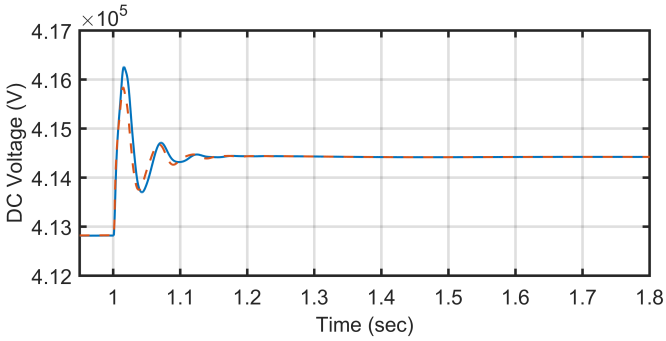

Figure 5.3: DC voltage response of the linearized model "Lin" and the time-domain non-linear model "Non-Lin" of the VSCs at (a) bus 4 , (b)bus 5 and (c) bus 6.

Small signal stability analysis

A small-signal stability analysis has been performed on the test system linearized model. From the analysis, the system has 79 eigenvalues. From the participation analysis, the faster eigenvalues belong to the inner loops of the all VSCs plus the outer control loops of the WF-VSCs. These eigenvalues are local to their states and do not interact with the other states. However, the slower eigenvalues belong to the states of the DC grid, PLLs, droop controlled VSCs outer loops. Due to the droop control of the GS-VSC converters, which control DC voltage indirectly, these eigenvalues participate in different percentages in the states of the GS-VSCs active-power control-loops and the DC grid. Due to the nonlinearity of the system, the eigenvalues change with the change in the operating conditions, which in turn leads to a system instability. Fig. 5.4 shows the change in the dominant eigenvalues due to a 20% incremental in the input power to the HVDC system from the wind farms and the AC grid A from 0.2 p.u. to 1 p.u. As can be seen, at some operating conditions, some eigenvalues move to the right of the imaginary axis and cause a system instability.

On the other hand, at certain local controllers' parameters and operating condition, as shown in Fig. 5.5, the root locus of the different subsystems (terminals) show that they are stable, while the eigenvalues of the overall system state matrix in Fig. 5.6 shows a degree of instability.

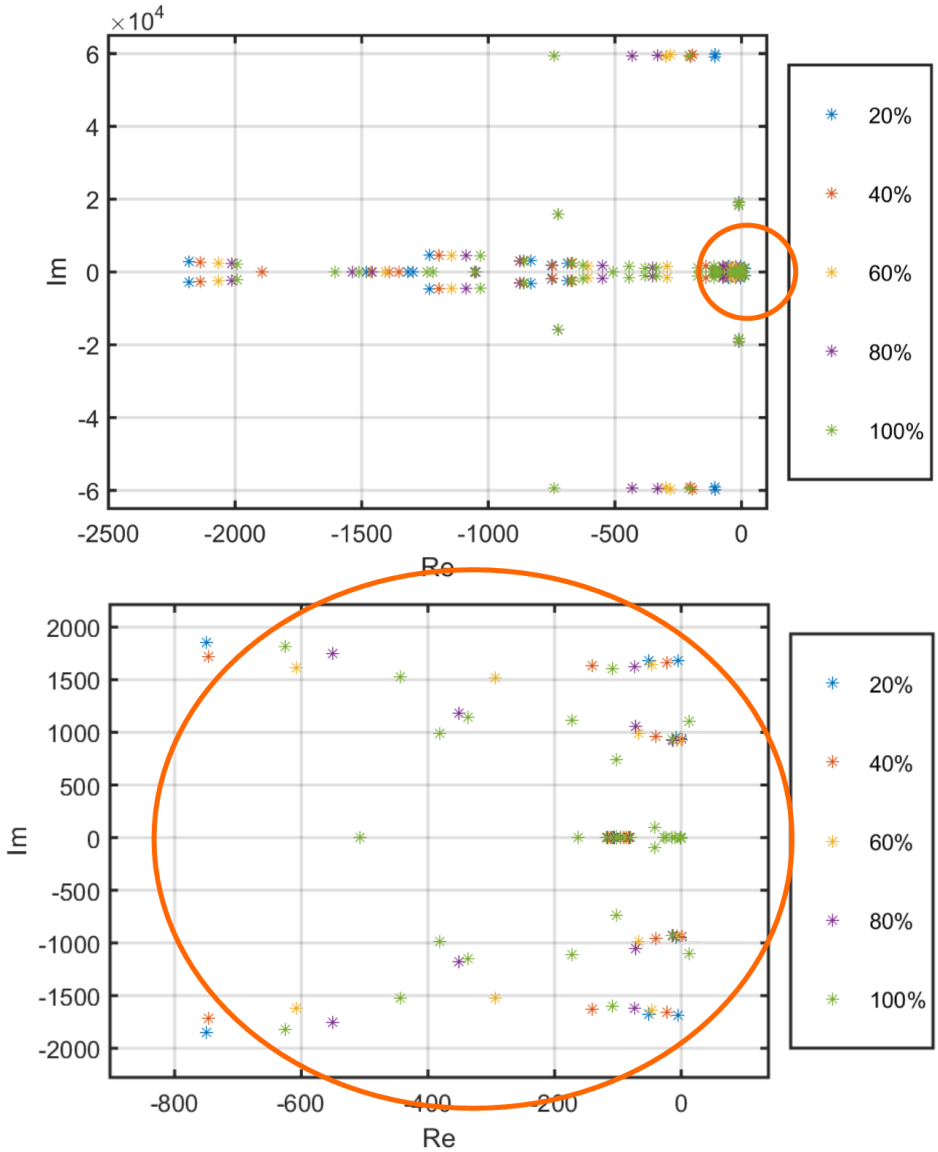

Figure 5.4: Effects of the change in operating points on the system eigenvalues.

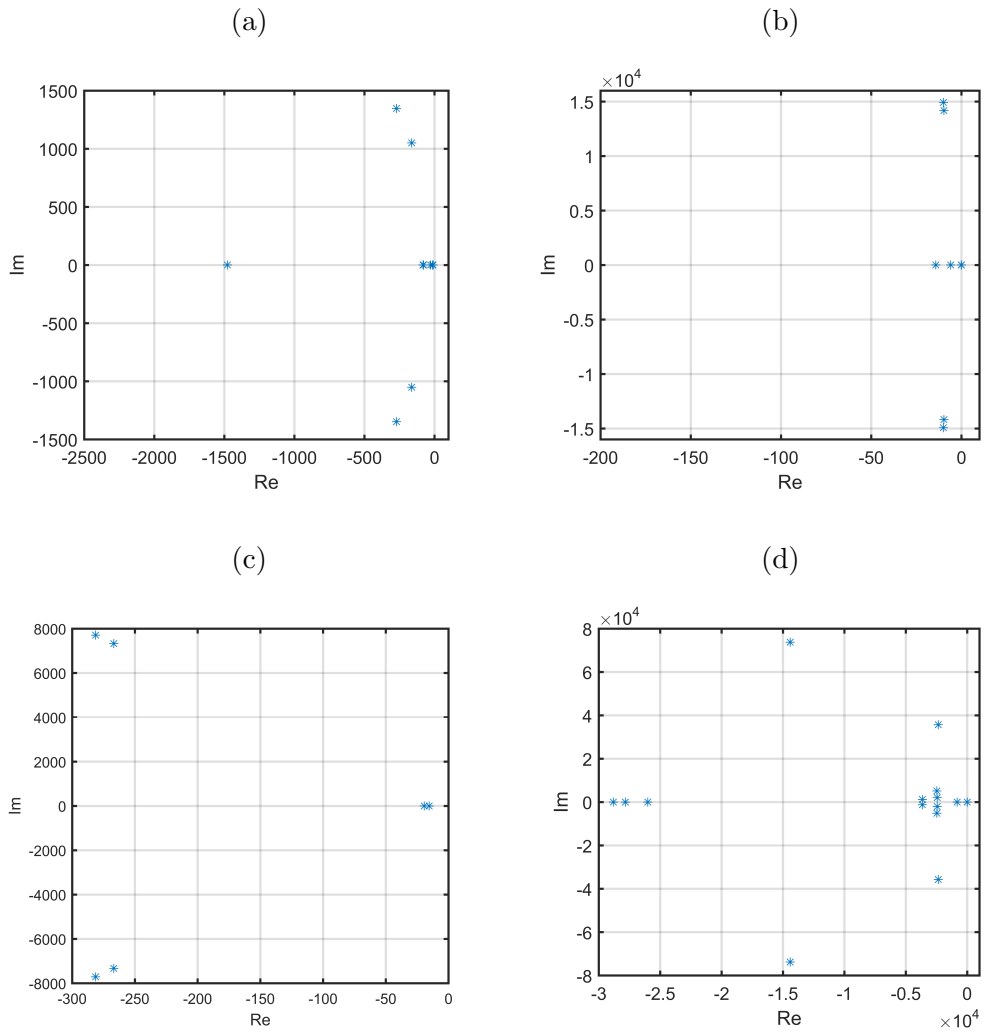

Figure 5.5: Eigenvalues of the state matrices of the (a) droop controlled GSVSC, (b)constant power controlled GSVSC, (c) WFVSC and (d) DC grid.

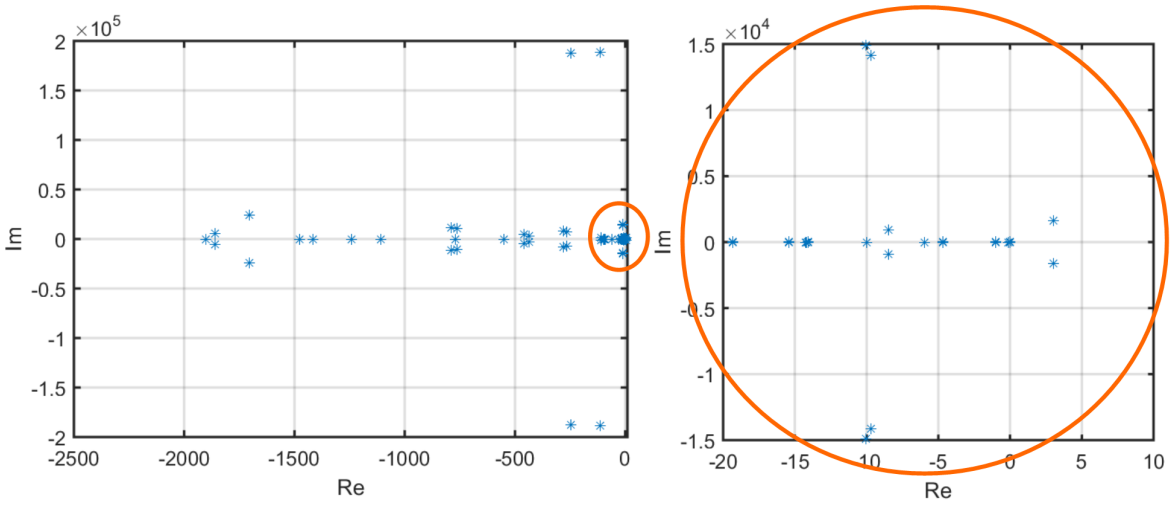

Figure 5.6: Eigen values of the overall system state matrix.

5.4.2 Time domain validation

The proposed tuning methodology has been used to tune the test system VSCs local controllers' gains. These gains are validated by simulate the test system with the tunes gains by the MATLAB/Simulink SymPowerSystem toolbox. The system was operating at 50% rated power from the Cb-A1 converter, in addition the two wind farms C and D was delivering 0.9% of their rated power. A 10% step of wind power was applied to the two WF VSCs Cb-C1 and Cb-C2. Fig. 5.7 shows the response of the active power flows through the converters Cb-B1, Cb-B2 and Cb-E1. As can be seen, the active power of the converters Cb-B1 and Cb-E1 has a fast response that takes less than 50 msec. As the Cb-B1 is connected to a long transmission line, which can be considered a weak grid, the response of Cb-B1 is slower than that of Cb-E1 due to the slower PLL response, while for Cb-B2 the active power response enhancement is limited by the connection to the DC grid through a long DC line and to a weak AC grid, which in turn increases slows down the PLL response.

Fig. 5.8 shows the fast response of DC voltage at the terminals of Cb-A1, Cb-C1 and Cb-D1. this fast response is due to the fast response of the active power control of the grid side converters and the high droop gains ($R_D = 14\ \Omega$). Due to the decoupling of the inner and the outer control loops of the WF VSCs from both the DC grid and the wind farms dynamics using the feed forward, the response of the AC voltage control is very fast, less than 10 msec. Fig. 5.9 shows the response of the AC voltage at the Cb-C1 and Cb-D1 PCC.

Fig. 5.10 shows the AC voltages at the PCC of the Cb-B1 and Cb-B2 have slower responses due to the dynamics of the PLL, which affect the dynamics of the active power and hence the AC voltage.

(a)

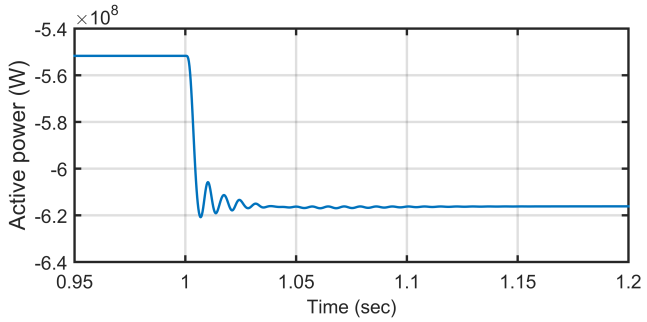

(b)

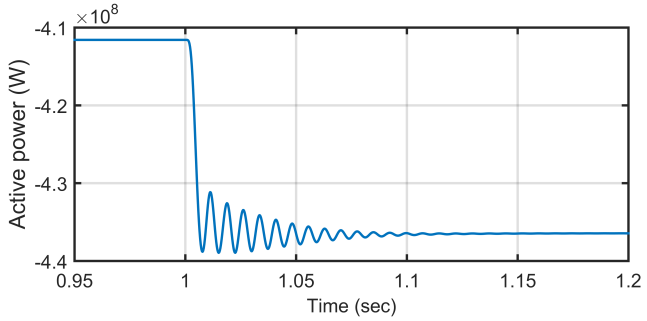

(c)

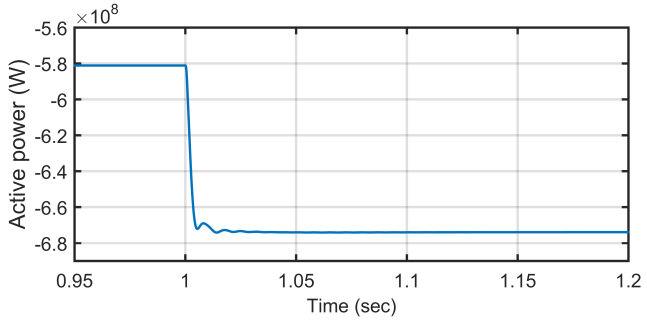

Figure 5.7: Active power response at AC side of the VSCs (a)Cb-B1 , (b)Cb-B2 and (c) Cb-E1.

(a)

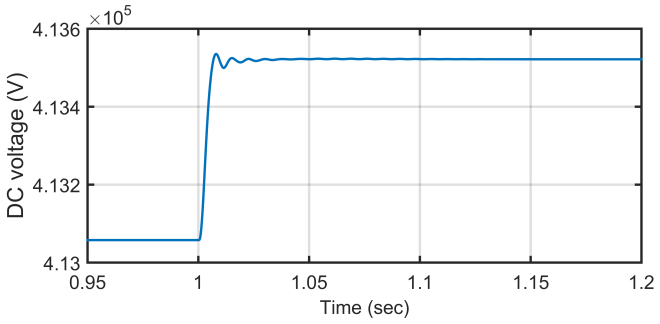

(b)

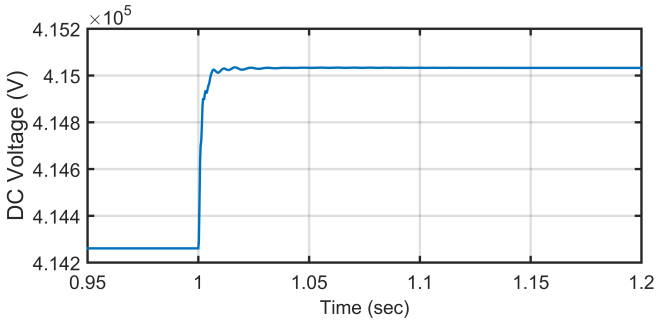

(c)

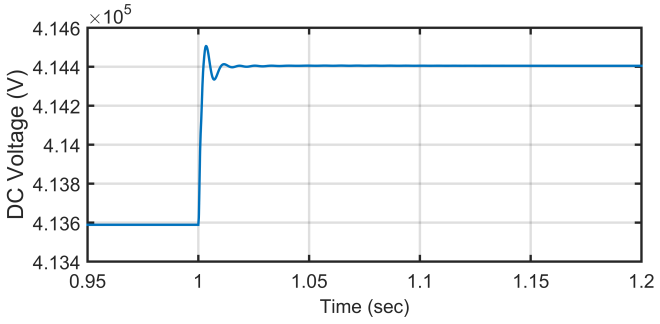

Figure 5.8: DC voltage response at the terminals of the VSCs (a)Cb-A1 , (b)Cb-C1 and (c) Cb-D1.

(a)

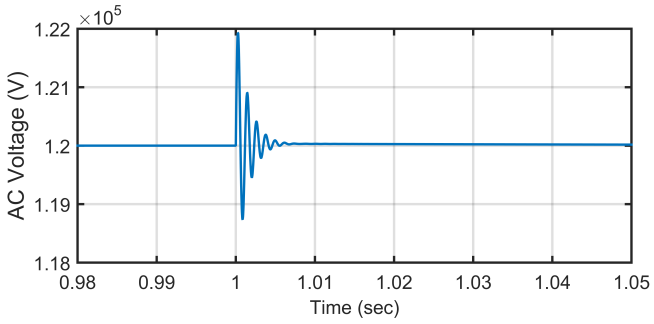

(b)

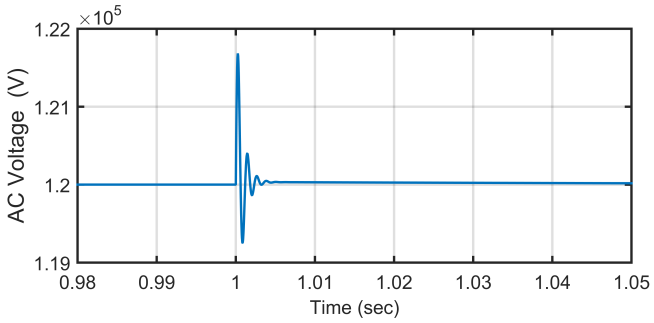

Figure 5.9: AC voltage response at the PCC of the VSCs (b)Cb-C1 and (c) Cb-D1.

(a)

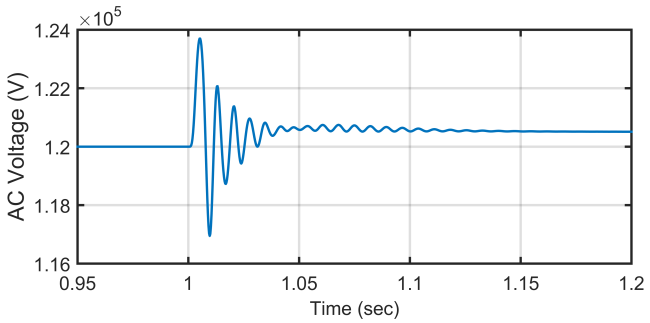

(b)

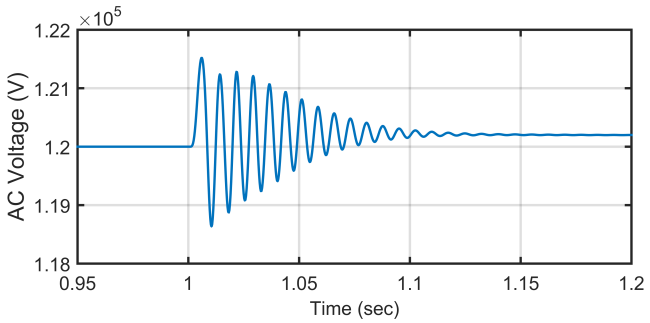

Figure 5.10: AC voltage response at the PCC of the VSCs (b)Cb-B1 and (c) Cb-B2.

5.5 Discussion

In this chapter, a detailed derivation of a MT VSC-HVDC wind farm integration system state-space linearized model was provided. That model was used in the proposed VSCs local controller parameter tuning methodology, which is based on the selection of the optimal parameters that increase the system performance band width and damping. The optimal parameters were selected to minimize the real parts of the dominant eigenvalues and maximize the damping ratio. This tuning process is performed every time the steady-state operating conditions are changed by the proposed power sharing control strategy in chapter 4. Through the time domain simulation results, the linearized state-space model was verified and the validation of the proposed tuning methodology was demonstrated. However, in some abnormal cases, such as the converter outage case, the GS VSCs operate at their maximum power limits and their local controllers lose their ability of regulating the DC voltage. In such scenarios, a control strategy is needed to control the DC voltage by control the active power generation of the wind farms, which is performed by the DC voltage control strategy that is proposed in the next chapter.

Chapter 6

DC Voltage Control during Permanent Converter-Outages for Power Flow Continuity in Offshore Multi-Terminal VSC-HVDC Systems

6.1 Introduction

Point-to-point HVDC links or MT HVDC networks isolate the offshore WF AC grids from the effects of onshore AC grid faults, which leads to temporary or permanent outages the onshore converters. This isolation results in the continuation of wind power generation by the wind turbines at the pre-fault operating level. If the onshore HVDC converters that receive the offshore wind power generation operate close to the maximum power capacity, they will be unable to absorb the active power of the disconnected onshore converter. In such cases, all onshore converters, which are responsible for regulating the DC voltage, operate at their rated power (i.e., in constant power control mode) and lose their ability to regulate the DC voltage. As a result, an overvoltage occurs, triggering protection devices and possibly leading to system collapse.

6.2 Proposed DC voltage Control Strategy

In literature, the FRT control strategies used to control the DC overvoltage were originally proposed for addressing the effects of temporary faults in onshore AC grids or temporary onshore VSC outages. Using such strategies to deal with permanent VSC outages is either infeasible, such as with DC chopper and FESS methods, or produces large oscillations in the system variables, such as fast wind power reduction methods. As mentioned previously, these oscillations arise as a result of the use of discontinuous (on/off) control rules in the wind generators. To reduce these oscillations, continuous fast-power-reduction control rules for WF-VSCs and wind generators were proposed in this work [**?**]. The proposed DC voltage controller relies on a reduction in the active current component of the wind generator, which has a faster control response than that of the pitch angle and can deal with the rapid rise in the DC voltage. This control strategy prevents the DC voltage from exceeding the maximum limit but not within the normal operating region. An additional stage of power reduction is therefore proposed for curtailing wind generation at steady-state conditions in order to return the system to its pre-outage state through the adjustment of the pitch angle of the wind turbine blades, which has a slower control response and cannot be used during the fast-power-reduction stage. The two stages of the proposed control strategy are explained in the following subsections.

6.2.1 Fast wind power reduction

This stage involves the reduction of the AC voltage level of the offshore WF grid by the WF-VSC as a function of the DC voltage rise after the occurrence of an onshore VSC outage. As a result of the AC voltage reduction, the proposed control rule for controlling the type 3 and 4 wind generators reduces the active power generation, rapidly, as a function of the AC voltage level [78].

WF-VSC DC voltage Control Rule

If the local DC voltage V_{DC} at the WF-VSC terminals is below a specified threshold level $V_{DC_{th}}$, which is usually the upper limit of the normal DC operating voltage range, the AC

voltage is set at its nominal value, i.e., 1 p.u., by setting the reference value of the d-axis component u_{WFd} at 1 p.u. and that of the q-axis component u_{WFq} at 0. However, if the DC voltage exceeds V_{DCth}, the WF-VSC decreases the reference value of the AC voltage d-axis component as a function of the rise in the DC voltage as expressed in (6.1) and illustrated in Fig. 6.1a.

$$u_{WF_d} = \begin{cases} 1 & , \; V_{DC} \leq V_{DC_{th}} \\ 1 - K_{DC-AC}\left(V_{dc} - V_{dc_{th}}\right) & , \; V_{dc} > V_{dc_{th}} \end{cases} \tag{6.1}$$

where K_{DC-AC} is calculated as follows:

$$K_{DC-AC} = \frac{u_{WF_{do}} - u_{WF_{dmin}}}{V_{dc_{max}} - V_{dc_{th}}} \tag{6.2}$$

where, $u_{WF_{do}}$is the nominal AC voltage level of the wind farm, $u_{WF_{dmin}}$is the minimum wind farm AC voltage level, and $V_{dc_{max}}$ is the maximum DC voltage that the VSC's switches can withstand.

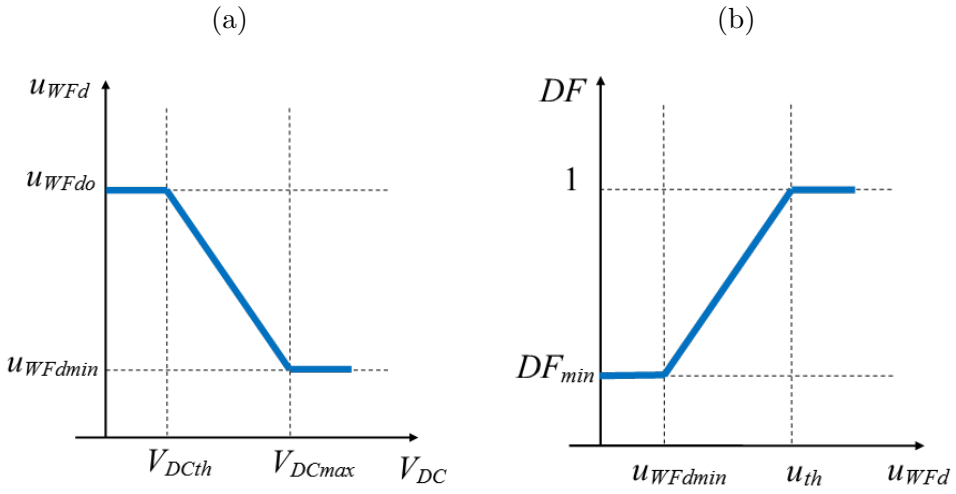

Figure 6.1: Relationships between (a) the HVDC and the WF AC voltages and (b) the DF and the WF AC voltage.

Wind Generator Power Reduction Control Rule

The fast wind power reduction is performed by reducing the reference value of the active component (i.e., the d-axis component) of the stator current in PMSGs or the rotor current in DFIGs based on a deloading factor (DF) ranging from 0 to 1, i.e., from zero generation to full generation. If the d-axis of the WF AC voltage u_{WFd} decreases below a specified threshold value u_{th}, which is usually equal to the nominal AC voltage of the system, i.e., 1 p.u., the value of the DF is calculated using (6.3), i.e., as a function of the local WF AC voltage at the terminals of the wind turbines [79]. This relation is depicted in Fig. 6.1b. To allow the proposed controller to operate properly, the reactive power based AC voltage regulation must be disabled. Therefore, in normal operation, the AC voltage level at the wind turbine bus is equal to or greater than the nominal value. This reasoning is behind both the reduction of the WF AC voltage below the nominal value if the voltage exceeds its threshold value and the selection of the threshold value of the WF AC voltage to be equal to the nominal voltage.

$$DF = \begin{cases} 1 & , u_{WF_d} \geq u_{th} \\ 1 - K_{AC-DF} \ (u_{WF_d} - u_{th}) & , u_{WF_d} < u_{th} \end{cases} \tag{6.3}$$

where K_{AC-DF} is calculated as follows:

$$K_{AC-DF} = \frac{1 - \ DF_{min}}{u_{WF_{do}} - \ u_{WF_{dmin}}} \tag{6.4}$$

where DF_{min} is the minimum DF, which is selected so that the oscillations in wind power are eliminated through the limiting of the wind generation reduction to a value greater than zero. In this study, the minimum DF is calculated as follows:

$$DF_{min} = \left(\frac{N-1}{N} \right) P_{W_{rated}} \tag{6.5}$$

where N is the number of power-receiving VSCs, and $P_{W_{rated}}$ is the per-unit rated power of the i^{th} power-receiving VSC.

The local wind generator control rules are implemented by modifying the controller of the PMSG MSC proposed in [61], [69], and that of the DFIG RSC, which is presented

in [66]. The modification is to multiply their active current component (d-axis) reference value by the value of the DF, as indicated in Fig. 6.2.

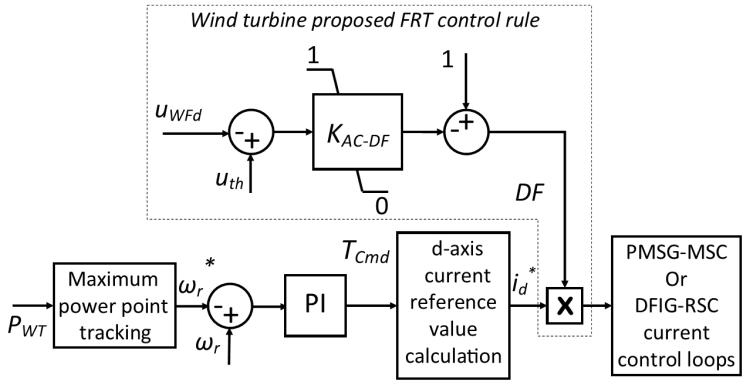

ω_r^* and ω_r : reference and actual rotor speeds, respectively.
PW_T : measured wind turbine active power output.
T_{cmd} : reference torque used for calculating the d-axis reference current.

Figure 6.2: Proposed DC voltage control rule of the wind turbine

6.2.2 Wind power curtailment

At steady-state conditions, the wind power is curtailed by adjusting the pitch angle of the wind turbine blades. This process is achieved using the pitch angle active power compensator described in [80], which modifies the reference pitch angle set by the rotor speed controller, which is used as presented in [66], [69][for types 3 and 4 variable-speed wind turbines in order to limit wind power generation at a maximum value P_{max}. After confirming the occurrence of a permanent onshore VSC outage and limiting of the DC voltage using the fast-power-reduction stage, the WF grid frequency F_{WF} is employed as a maximum power reference signal from the WF-VSC station to the wind turbines. The WF-VSC station sets the value of F_{WF} based on the P_{max} value desired, as follows:

$$F_{WF} = F_{WF_o} + K_{F-P}\ (1 - \ P_{max}) \tag{6.6}$$

where F_{WFo} is the nominal frequency of the WF, and K_{F-P} is calculated as follows:

$$K_{F-P} = \frac{F_{WF_{max}} - F_{WF_o}}{P_{WT_r} - P_{WT_{min}}} \tag{6.7}$$

where $F_{WF_{max}}$ is the maximum frequency of the WF, P_{WTr} is the per-unit rated power of the wind turbine, and $P_{WT_{min}}$ is the allowable minimum power generation of the wind turbine.

Based on the frequency value, the local controller of the wind turbines measures the WF grid frequency and calculates the desired P_{max} using (6.8) the reference point for the pitch angle active power compensator.

$$P_{max} = P_{WT_r} - \frac{F_{WF} - F_{WF_o}}{K_{F-P}} \tag{6.8}$$

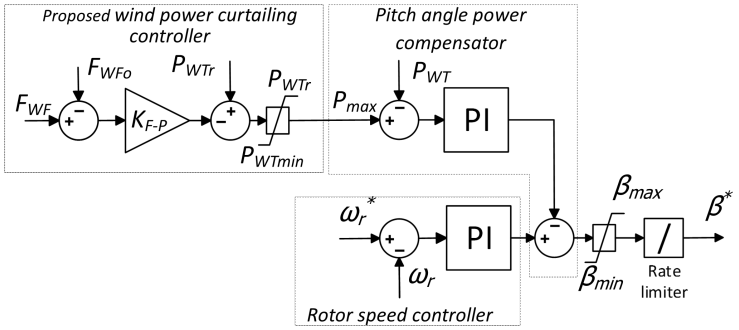

β^* : reference pitch angle
β_{max} and β_{min} : limits of the pitch angle
ω_r^* and ω_r : reference and actual rotor speeds, respectively.

Figure 6.3: Structure of the wind turbine power curtailment controller.

The implementation of the proposed wind power curtailment controller is illustrated in Fig. 6.3. The value of P_{max}can be selected in different ways based on the desired scenario. For example, the P_{max} of each WF can be calculated using an optimal power flow (OPF) algorithm to minimize the transmission loss from the HVDC network after the share attributable to the faulted onshore VSC has been disconnected. For the work presented in this paper, the P_{max} values of all WFs are assumed to be equal, with their

summation is assumed to be equal to its pre-fault value after the removal of the share arising from the faulted converter.

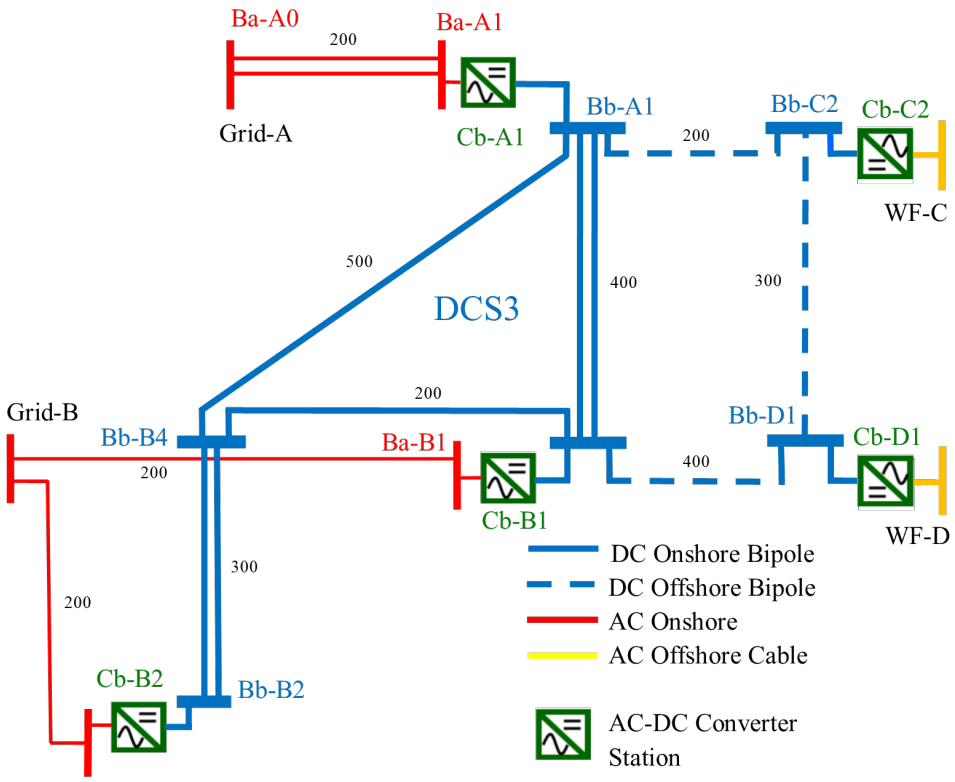

Figure 6.4: Modified CIGRE-B4 MT-HVDC test system.

6.3 Simulation Results

The DC voltage control strategy proposed in this chapter was validated using a modified CIGRE B4 DC grid test system, which included two onshore AC grids and four offshore AC grids (wind farms). Detailed system data can be found in [2]. The modifications applied to the system are in the number of terminals and the ratings of the wind farms. The modified bipolar HVDC B4 CIGRE test system grid depicted in Fig. 6.4 was used as the

test system, emulating two offshore wind farms C and D, which are connected to onshore AC grids A and B through the overhead and cable DC links of the HVDC network DCS3. The AC grid B has two VSC ports to the DCS3 network: Cb-B1 and Cb-B2. The AC grid A and wind farms C2 and D1 are also connected to the DCS3 network through VSCs: Cb-A1, Cb-C2, and Cb-D1, respectively. The modification is performed on the ratings of the system VSCs and the corresponding system parameters as stated in Table 4.1 and Table 4.2, respectively. The per-unit data were calculated based on common base values, as follows: base power $S_{base} = 1200$ MVA, base DC voltage $V_{DC_{base}} = 400$ kV, onshore and offshore base AC voltage $V_{AC_{base}} = 120$ kV, and base frequency $F_{base} = 60$ Hz. The DC voltage limits of the HVDC system are set to be 105 % and 95 % of the nominal voltage, which was selected as the base DC voltage. During normal operation, the AC voltage limits of the wind farms C and D are 1.05 p.u. and 0.95 p.u.

The effectiveness of the proposed control strategy was tested for two main scenarios: a permanent VSC outage and a temporary VSC outage. For the permanent outage scenario, the new strategy was examined for two different cases: DFIG- and PMSG-based offshore WFs. The simulation was performed using Matlab/Simulink software. In addition, a previously recent proposed fast wind-power-reduction FRT control strategy was applied to the test system for the permanent VSC outage scenario, in order to show its deficiencies with respect to dealing with that condition. For the simulation, the wind power generated was shared between the two onshore AC grids, A and B, through the three VSCs, Cb-A1, Cb-B1, and Cb-B2, which are able to absorb up to 2.5 p.u. active power. To test the proposed control strategy, two different types of VSC outages were introduced at the Cb-A1 converter: a permanent and a 500 ms temporary outage, resulting in the power absorbed by the onshore AC grid A dropping to zero. The capacity of the onshore VSCs was consequently reduced to 1.667 p.u. rather than 2.5 p.u. To create a power imbalance in the HVDC network, the wind generation from the offshore wind farms WF-C and WF-D was adjusted to be greater than 1.667 p.u. so that Cb-B1 and Cb-B2 were unable to absorb part of the offshore wind power. As a result, they operated in constant power control mode at their rated power, leaving the DC voltage of the HVDC network without regulation. The result was a rise in the DC voltage, which in turn, triggered the FRT control rules of the wind farms at the moment the DC voltage threshold V_{DCth} was exceeded. The value of $V_{DC_{th}}$ was selected to be 1.05 p.u.

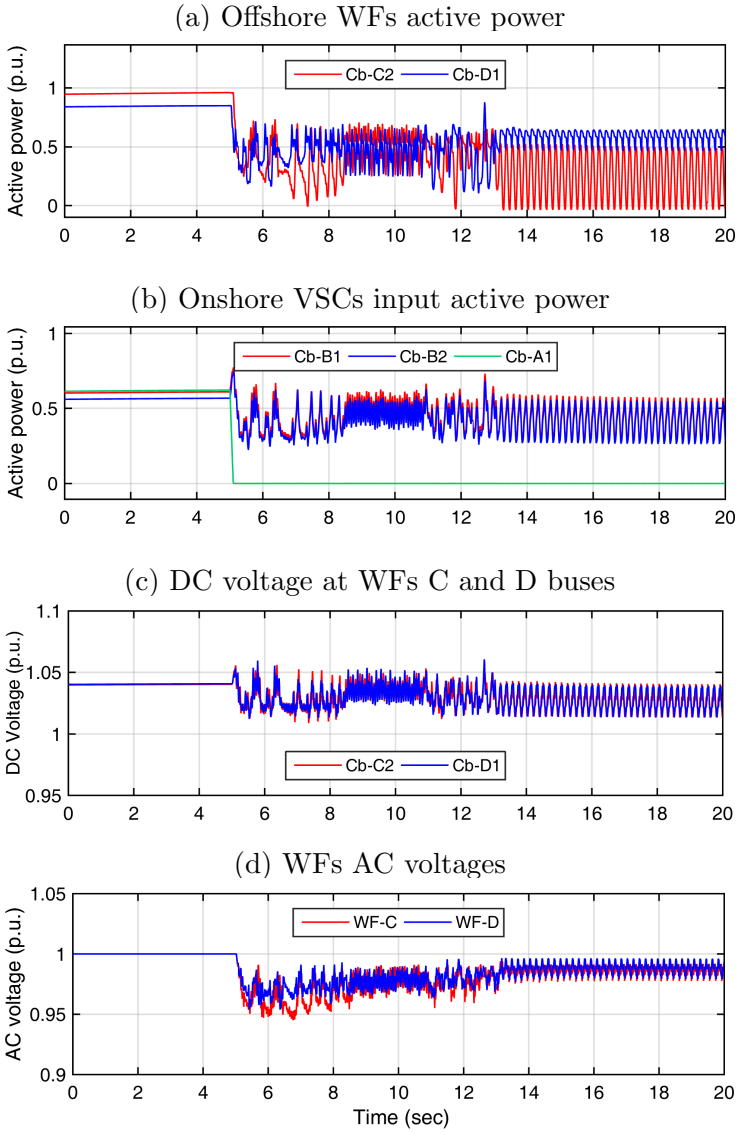

Figure 6.5: System performance after a permanent outage at Cb-A1 with the previously proposed FRT control strategy

6.3.1 Permanent outage scenarios

Previous FRT control strategy case:

The fast-power-reduction FRT control strategy previously proposed in [63], [57], [61], which addressed only temporary outage scenarios, was applied to the test system, which is equipped with DFIG-based wind farms, during a permanent outage at the Cb-A1 VSC. The outage began at second 5. As shown in Fig. 6.5, the previous FRT control strategy failed to mitigate the DC voltage rise without producing an instability and large oscillations in the active power, the DC voltage, and the WF AC voltage.

Proposed control strategy cases:

The proposed DC voltage control strategy was evaluated for two different cases: offshore windfarms equipped with DFIG wind turbines and with PMSG wind turbines. In both cases, based on the parameters listed in Table III, the proposed DC voltage controller gains KDC-AC, KAC-DF, and KF-P were calculated to be 2, 6.667, and 0.01, respectively. The wind power generation was curtailed after the outage by setting Pmax = 0.667 p.u. for each offshore wind farm, which was calculated by subtracting the capacity of the faulted converter from the summation of the rated power of the WF-VSCs.

a) DFIG-based offshore wind farm case:

In this case, the offshore wind farms C and D are equipped with DFIG (type 3) wind turbines. The generation levels of the two offshore wind farms C and D were 0.95 p.u. and 0.89 p.u., respectively. As shown in Fig. 6.6a and Fig. 6.6b, at second 5, Cb-A1 was disconnected permanently, and its power dropped to zero. Converters Cb-B1 and Cb-B2 were then able to absorb only the active power up to their rated value, 0.833 p.u., and were unable to absorb the 1.83 p.u. active power from the wind farms. The DC voltage consequently began to rise and triggered the proposed DC voltage control strategy of the offshore wind farms, as indicated in Fig. 6.6c. The DC voltage control rules in the WF-VSCs Cb-C2 and Cb-D1 reduced the AC voltage of their wind farms as a function of the rise in the DC voltage (Fig. 6.6d). This AC voltage reduction then triggered the proposed control rule in the local controller of the wind turbines, which decreased the active power generation rapidly by reducing the generator direct current component. The fast wind

power reduction slow down the DC voltage increasing rate and kept the DC voltage level below its maximum value of 1.1 p.u. and to be 1.07 p.u. The DC voltage, AC voltage and active power dynamics due to the proposed DC voltage first stage, i.e., fast power reduction stage, are shown in the period between second 5 and second 10.

In order to confirm that the outage is permanent or for long time and not temporary, the wind power generation curtailment stage was activated after 5 seconds following the outage by increasing the wind farm frequency. Hence, the VSCs of wind farms C and D raised their WF grid frequency to 1.0033 p.u., as depicted in Fig. 6.6e , so that the system could recover to its pre-outage state. The active power generation of each of the two offshore wind farms was curtailed at 0.667 p.u., following the DC voltage decreased to approximately its pre-outage value within normal operating limits. The difference in the DC voltage before the outage and after recovery is due to the changes in the system configuration and the operating conditions, which could be more accurate if the Pmax value of each wind farm were selected through an OPF algorithm so that the same shares would be maintained for Cb-B1 and Cb-B2. The period between seconds 10 and 28 shows the dynamics of the pitch angle controller, which is very small compared with the first stage dynamics. Thus, power reduction using the pitch angle controller cannot be used to deal with the fast DC voltage rise, and it used only for reducing the active power to control the steady-state active power generation.

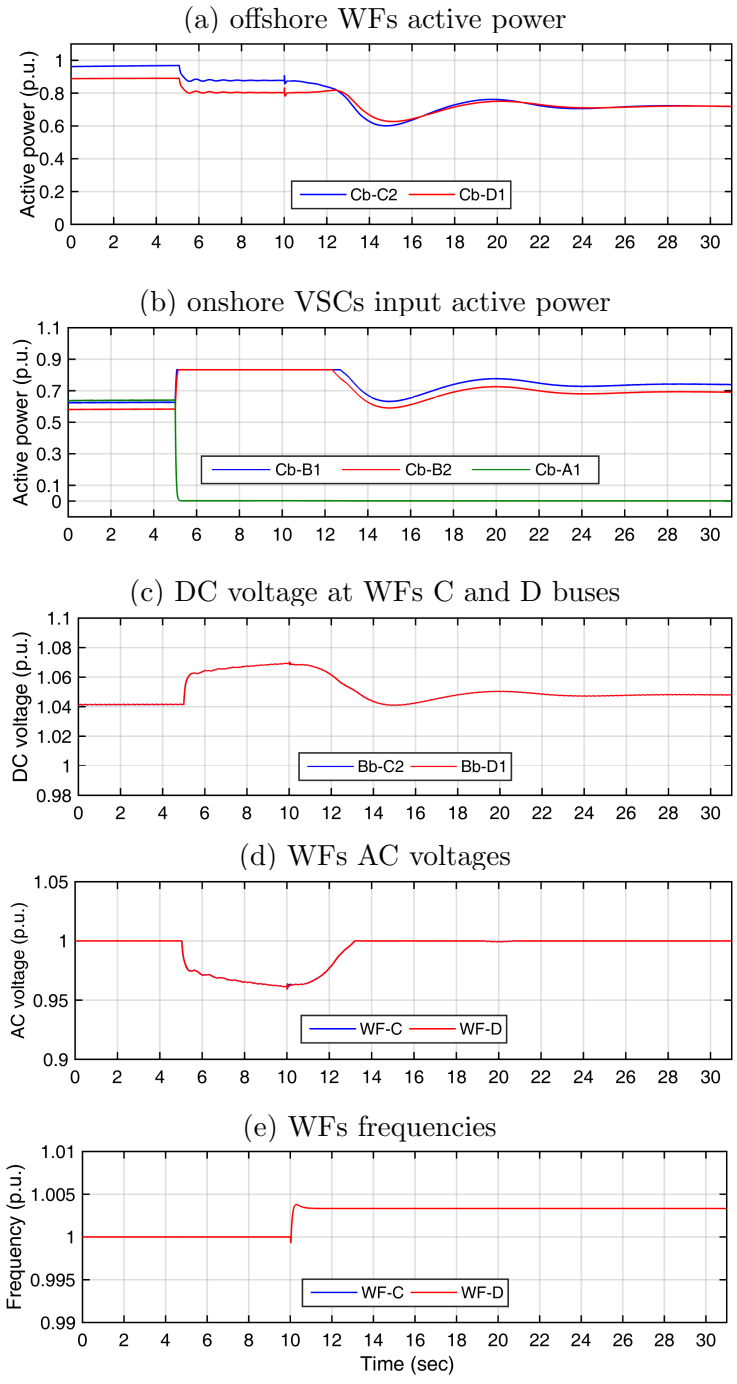

Figure 6.6: Performance of the proposed control strategy after a permanent converter outage in the case of wind farms with a DFIG wind turbine

b) PMSG-based offshore wind farm case

This case demonstrates the effectiveness of the proposed control strategy with respect to addressing permanent VSC outages in the case of PMSG-equipped wind farms. The wind power generation was adjusted to be 0.9 p.u. and 0.94 p.u. for wind farms C and D, respectively. The disconnection of one of the onshore VSCs thus causes a power imbalance in the HVDC network, producing a DC overvoltage. After the disconnection of Cb-A1 at second 5 producing a rapid DC overvoltage, which triggered the DC voltage control process in the offshore wind farms. As indicated in Fig. 6.7, the DC voltage control followed the same steps as with the DFIG wind farm case. In addition, the wind power was curtailed by increasing the offshore WF frequencies to 1.004 p.u. after 5 seconds from the outage, see Fig. 6.7e in order to set the Pmax value of each wind farm at 0.65 p.u. As can be seen in Fig. 6.7a and Fig. 6.7b, the fast response of the fast power reduction by reducing the AC current component of the generators is able to limit the DC overvoltage to be less than the maximum value 1.1 p.u. , exactly at 1.07 p.u, see Fig. 6.7c. Furthermore, Fig. 6.7 shows the slow dynamics of the pitch angle controller, which takes 18 second from changing the wind farm frequency to settle. Fig. 6.7d show the dynamics of the AC voltage of the two wind farms.

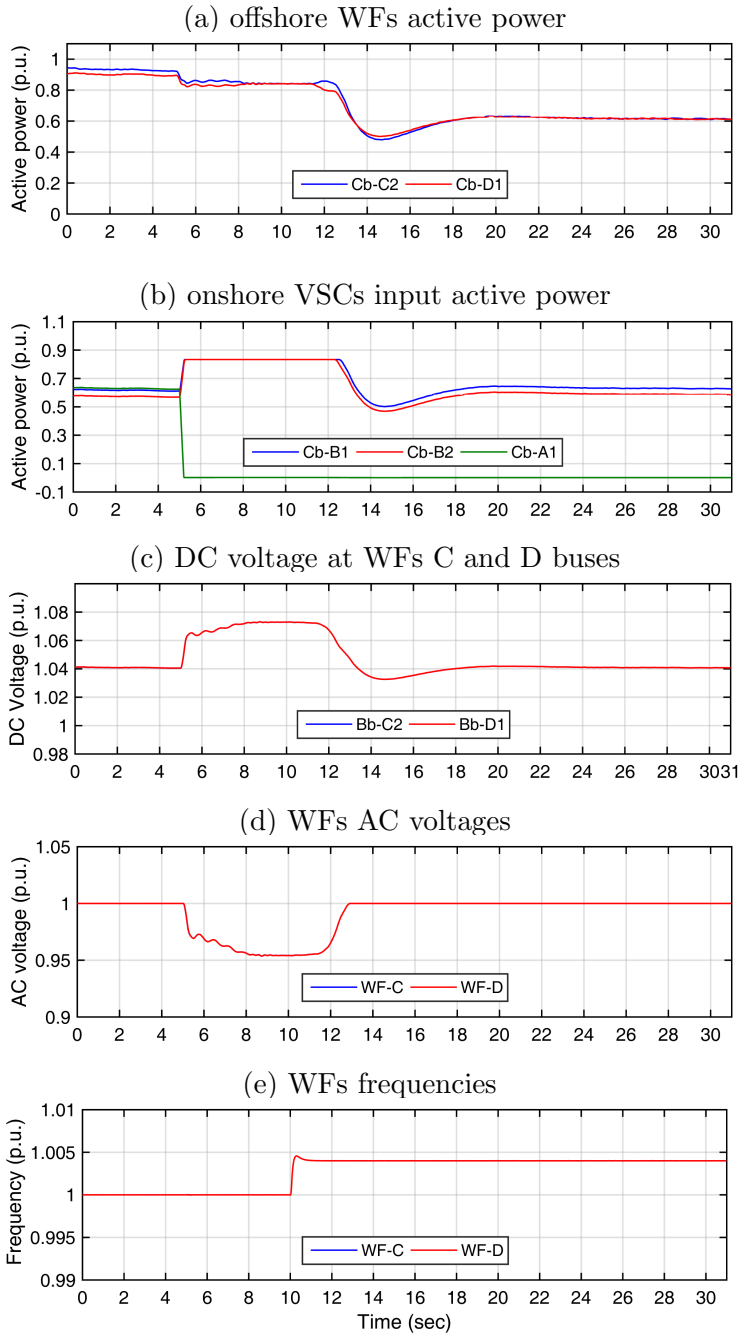

Figure 6.7: Performance of the proposed control strategy after a permanent converter outage in the case of wind farms with a PMSG wind turbine

6.3.2 Temporary outage scenario

In this scenario, the proposed control strategy was validated for the case of a temporary outage at one of the onshore converters, as a FRT control strategy for mitigating the effects of a temporary outage in an onshore VSC. This scenario was tested for two cases: a wind farm equipped with a DFIG wind turbine and one with a PMSG wind turbine. In both cases, the wind power generation was adjusted to be greater than the capacity of the onshore converter during a converter outage, i.e., during a disconnection of one of the onshore converters. A temporary 500 ms outage was introduced into the onshore Cb-A1. The same control gains as in the permanent outage scenario were applied in this scenario. As can be seen in Fig. 6.9, the temporary fault began at second 1 and ended after 0.5 s. During the fault period, the DC voltage at the wind farm DC buses increased due to the power imbalance in the HVDC network, consequently triggering the proposed controller. Then, the wind turbines then rapidly reduced their generation, which in turn, reduced the rate of the rise in the DC voltage, thus preventing it from exceeding its maximum limit during the outage period. Fig. 6.8a to Fig. 6.8d show the performance of the proposed control strategy for the DFIG wind turbine. the DC voltage rise limitation performance during a temporary outage the PMSG wind turbine are shown in Fig. 6.9a to Fig. 6.9d. As concluded from the results, the proposed controller is able to limits the DC overvoltage during the temporary outage, and it has a similar performance as that proposed in [57].

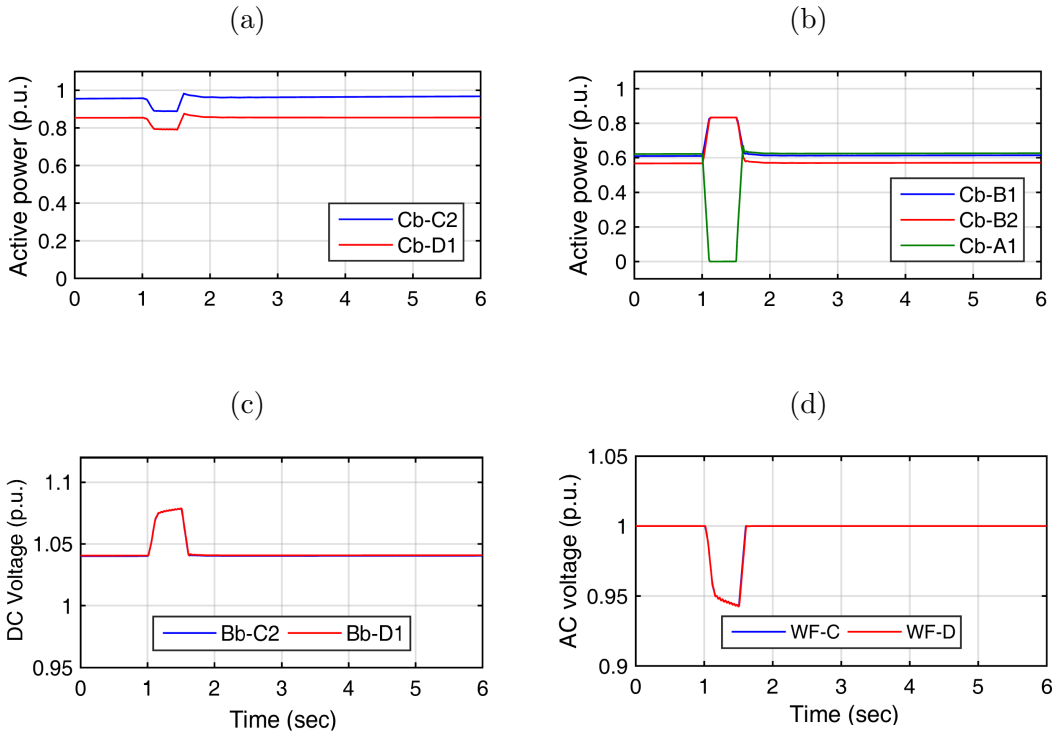

Figure 6.8: Performance of the proposed control strategy in the case of DFIG and PMSG wind farms during a temporary converter outage for the DFEG case (a) offshore WFs active power; (b) onshore VSCs input active power; (c) DC voltage at WFs C and D buses; (d) WFs AC voltages.

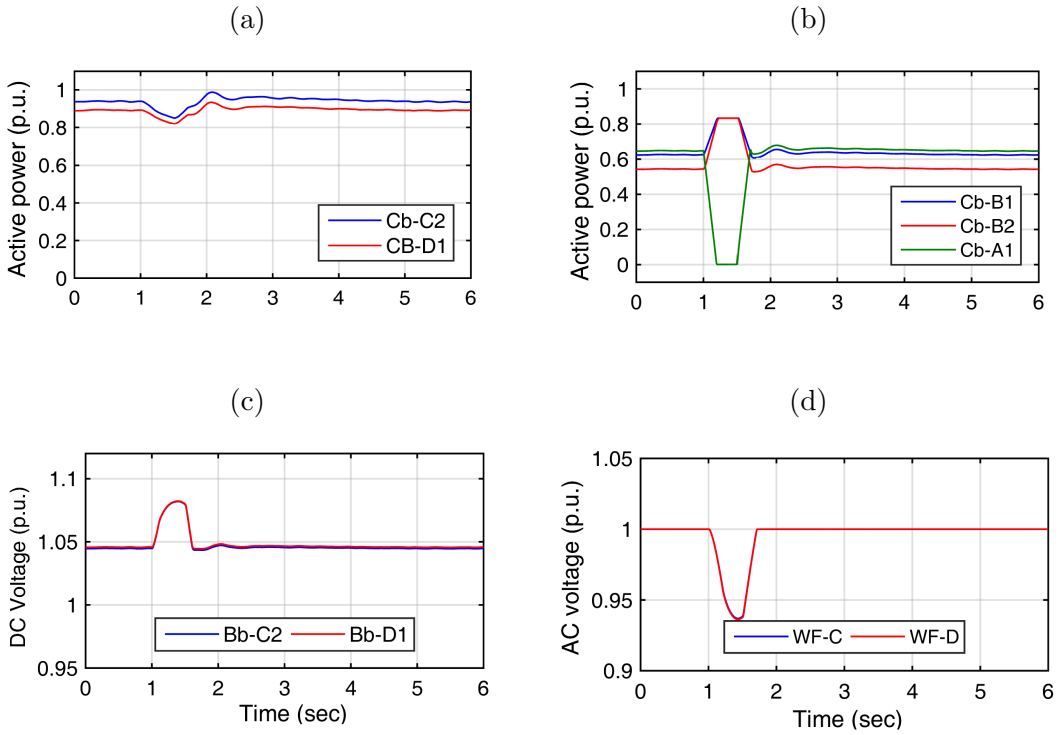

Figure 6.9: Performance of the proposed control strategy in the case of DFIG and PMSG wind farms during a temporary converter outage for the PMSG case (a) offshore WFs active power ; (b) onshore VSCs input active power; (c) DC voltage at WFs C and D buses; (d) WFs AC voltages.

6.4 Discussion

This chapter has proposed a DC voltage control strategy for regulating the DC voltage during permanent or temporary outages in onshore GS VSCs for offshore MT HVDC systems. The new control strategy relies on communication-free decentralized control rules implemented in the local controllers of the WF-VSCs and the wind turbines. The proposed control rules have been designed for wind farms VSCs and two types of wind turbines: DFIGs and PMSGs. The proposed controller also provides wind power curtailment, which can be used to curtail the output power of the WFs during normal operation or as a means of restoring the system to its pre-fault state after a permanent onshore VSC outage. All of the simulation results reveal that the proposed control strategy is able to limit fast rises in the DC voltage and to keep it at levels lower than its maximum limit using the first stage of the strategy. Furthermore, the second stage of the control strategy, wind power curtailing stage, is able to restore the steady state pre-outage conditions of the system by curtailing the wind power using the pitch angle control of the wind turbines. The simulation was performed on a modified B4 CIGRE test system for two different scenarios: permanent and temporary converter outages, and for two cases within each scenario: DFIG and PMSG wind farms.

Chapter 7

Summary, Conclusion and Contributions

7.1 Summary and Conclusion

The main objective of this thesis was proposing an operation and control strategies for a MT VSC-HVDC based offshore wind farms integration system by developing a centralize (supervisory) controller for both the steady-state operation and the transient dynamics performance perspectives. From the steady-state perspective, an adaptive droop-based power-sharing control strategy was proposed in chapter 4 in order to control the sharing of the active power transmitted by a MT VSC-HVDC network among a number of onshore AC grids or offshore loads based on the desired percentage shares utilizing voltage droop concepts. Due to the nonlinearity of the system, the system dynamic performance is dependent on its operating condition as shown in chapter 5. From this perspective, two methodologies for selecting the optimal droop gains and the VSCs local controllers' gains are proposed in chapters 4 and 5 to enhance the system dynamic performance. Furthermore, in case of a permanent outage in one of the gird side converters which may cause a DC voltage control loss and power imbalance, a control strategy was proposed in 6 to mitigate the effects of this outages and recover the system to its pre-outage state.

In chapter 4 power-sharing control and voltage regulation strategy was proposed. The

primary objective of the new control strategy is achieving accurate sharing of the active power from offshore wind farms or onshore AC grids and transmitted by a MT HVDC network among a number of onshore AC grids or offshore loads based on the desired percentage shares, while keeping the DC voltage at all buses within the operating range. The control strategy is based on two hierarchal levels: voltage-droop control as the primary controller and secondary (supervisory) controller, which uses an optimal-power flow (OPF) algorithm and a novel droop gain selection methodology for selecting the optimal droop parameters considering the DC voltage transient and steady-state dynamic responses.

In chapter 5 a tuning methodology is proposed for selecting the optimum local controller parameters of the VSCs in an offshore MT HVDC network to enhance the dynamic performance and the small-signal stability of the system by maximizing the control system bandwidth and damping. As a part of the proposed methodology, a derivation procedure of the aggregated linearized state-space model of a MT VSC-HVDC based offshore wind farm integration system was provided.

In chapter 6 a control strategy for controlling the DC voltage of the HVDC network during a permanent and temporary grid side converter outages was proposed. The proposed control strategy relies on the reduction of the active current component of the wind generator, which has a faster control response than that of the pitch angle and can deal with the rapid rise in the DC voltage. This control strategy prevents the DC voltage from exceeding the maximum allowable limit, which is not within the normal operating region. An additional stage of power reduction is therefore proposed for curtailing wind generation at steady-state conditions in order to return the system to its pre-outage state through the adjustment of the pitch angle of the wind turbine blades.

7.2 Contributions

The main contributions of the work are

1. Develop a new power-sharing control strategy that utilizes an adaptive voltage-droop scheme, in which the voltage-droop parameters are optimally selected as a means of achieving accurate power sharing based on the desired shares, which are optimized in

advance by the system operator in order to fulfill the active power requirements of the connected AC grids, while also including consideration of the DC voltage dynamics, including transient and steady-state performance.

2. Develop a new tuning methodology for selecting the optimum local controller parameters of the VSCs in an offshore MT HVDC network to mitigate the effects of the operating conditions changes on the transient performance and the small-signal stability of the system.

3. Develop a novel control strategy to mitigate DC overvoltage effects without producing oscillations in the DC voltage and the wind power generation in case of permanent outage in an onshore VSCs, which can be used in temporary fault/outage ride through control as well.

7.3 Future Research Directions

Based on the studies and findings illustrated in this thesis, the following directions are suggested for future studies:

1. Developing a decentralized online methodology for VSCs local controller parameters tuning, which is based on the VSC impedance reshaping considering the VSC impedance and the estimated AC and DC grid impedances. the new methodology will increase the system reliability and the control robustness.

2. Developing a PI compensator-based fast power reduction control rule in the wind turbine local controller for regulating the DC overvoltage during permanent converter outages. Introducing such a compensator needs more investigation and modeling for both the wind turbine and the wind farm grid. The integral part of this compensator will eliminate the steady state error in the DC voltage from the threshold during the outage, which in turn not only limiting it below the allowable maximum value but also regulates the DC voltage within the permissible operating limits.

References

[1] European Wind Energy Association, "The European Offshore Wind Industry - Key Trends And Statistics 1st Half 2013," Association, European Wind Energy, Tech. Rep., 2013. xiii, 1, 2

[2] CIGREE B4 working group, "The CIGRE B4 DC Grid Test System," 2013. xiv, 50, 51, 93

[3] European Wind Energy Association, "Pure Power - Wind Energy Scenarios up to 2030," Tech. Rep., 2008. 1, 11

[4] K. Bell, D. Cirio, A. M. Denis, L. He, C. C. Liu, G. Migliavacca, C. Moreira, and P. Panciatici, "Economic And Technical Criteria For Designing Future Off-shore HVDC Grids," in *Innov. Smart Grid Technol. Conf. Eur. (ISGT Eur. IEEE PES*, 2010, pp. 1–8. 1, 11

[5] K. M. Omatola, "AC Versus DC Transmission System Technology," *J. Phys. Sci. Innov.*, vol. 3, pp. 1–7, 2011. 1

[6] D. M. Larruskain, I. Zamora, A. J. Mazón, O. Abarrategui, and J. Monasterio, "Transmission and Distribution Networks : AC versus DC," in *IEEE Power Eng. Soc. Gen. Meet.*, 2007, pp. 1–5. 1

[7] L. Xu, L. Yao, and C. Sasse, "Grid Integration of Large DFIG-Based Wind Farms Using VSC Transmission," *IEEE Trans. Power Syst.*, vol. 22, no. 3, pp. 976–984, 2007. 1, 13

[8] M. Starke and L. M. Tolbert, "AC vs . DC Distribution : A Loss Comparison," in *Transm. Distrib. Conf. Expo.*, 2008, pp. 1–7. 2

[9] O. Gomis-Bellmunt, J. Liang, J. Ekanayake, R. King, and N. Jenkins, "Topologies of Multiterminal HVDC-VSC Transmission for Large Offshore Wind Farms," *Electr. Power Syst. Res.*, vol. 81, no. 2, pp. 271–281, feb 2011. [Online]. Available: http://linkinghub.elsevier.com/retrieve/pii/S0378779610002166 2

[10] European Transmission System Operators, "European Wind Integration Study (EWIS) towards a successful integration of wind power into European electricity grids - final report," Tech. Rep., 2007. 2

[11] J. Reeve, L. X. Bui, and S. Casoria, "Modeling of the hydro-quebec - new england HVDC system and digital controls with emtp," *IEEE Trans. Power Deliv.*, vol. 8, no. 2, pp. 559–566, 1993. 3

[12] F. Mazzoldi, J. P. Taisne, C. J. B. Martin, and B. A. Rowe, "Adaptation of the control equipment to permit 3terminal operation of the HVDC link between sardinia, corsica and mainland italy," *IEEE Power Eng. Rev.*, vol. 9, no. 4, p. 87, 1989. 3

[13] T. Nakajima and S. Irokawa, "A control system for HVDC transmission by voltage sourced\nconverters," in *1999 IEEE Power Eng. Soc. Summer Meet. Conf. Proc. (Cat. No.99CH36364)*, vol. 2, 1999, pp. 1113–1119. 3

[14] M. K. Bucher, R. Wiget, G. Andersson, and C. M. Franck, "Multiterminal HVDC Networks What is the Preferred Topology ?" *IEEE Trans. Power Deliv.*, vol. 29, no. 1, pp. 406–413, 2014. 11

[15] J. Beerten, S. Cole, and R. Belmans, "Modeling of Multi-Terminal VSC HVDC Systems With Distributed DC Voltage Control," *IEEE Trans. Power Syst.*, vol. 29, no. 1, pp. 34–42, jan 2014. [Online]. Available: http://ieeexplore.ieee.org/lpdocs/epic03/wrapper.htm?arnumber=6588621 12, 19, 25

[16] G. O. Kalcon, G. P. Adam, O. Anaya-Lara, S. Lo, and K. Uhlen, "Small-Signal Stability Analysis of Multi-Terminal VSC-Based DC Transmission Systems," *IEEE Trans. Power Syst.*, vol. 27, no. 4, pp. 1818–1830, nov 2012. [Online]. Available:

http://ieeexplore.ieee.org/lpdocs/epic03/wrapper.htm?arnumber=6185716 13, 22, 24, 25

[17] G. Pinares, L. B. Tjernberg, L. A. Tuan, C. Breitholtz, and A.-A. Edris, "On the Analysis of the DC Dynamics of Multi-terminal VSC-HVDC Systems Using Small Signal Modeling," *2013 IEEE Grenoble Conf.*, pp. 1–6, jun 2013. [Online]. Available: http://ieeexplore.ieee.org/lpdocs/epic03/wrapper.htm?arnumber=6652303 13, 22, 24, 32

[18] A. Yazdani and Reza Iravani, *Voltage-Sourced Converters in Power Systems: Modeling, Control, and Applications*. WILEY and IEEE PRESS, 2010. 14, 36

[19] J. Z. Zhou, H. Ding, S. Fan, Y. Zhang, and A. M. Gole, "Impact of short circuit ratio and phase locked loop parameters on the small signal behavior of a VSC HVDC converter," *IEEE Trans. Power Deliv.*, vol. 29, no. 5, pp. 2287–2296, 2014. [Online]. Available: http://ieeexplore.ieee.org/lpdocs/epic03/wrapper.htm?arnumber=6850084 14, 36

[20] T. M. Haileselassie and K. Uhlen, "Impact of DC Line Voltage Drops on Power Flow of MTDC Using Droop Control," *IEEE Trans. Power Syst.*, vol. 27, no. 3, pp. 1441–1449, aug 2012. [Online]. Available: http://ieeexplore.ieee.org/lpdocs/epic03/wrapper.htm?arnumber=6169971 14, 21

[21] E. Prieto-Araujo, F. D. Bianchi, A. Junyent-Ferré, and O. Gomis-Bellmunt, "Methodology for Droop Control Dynamic Analysis of Multiterminal VSC-HVDC Grids For Offshore Wind Farms," *IEEE Trans. Power Deliv.*, vol. 26, no. 4, pp. 2476–2485, 2011. 15, 21, 22, 43, 44, 45

[22] J. Liang, T. Jing, S. Member, and O. Gomis-bellmunt, "Operation and Control of Multiterminal HVDC Transmission for Offshore Wind Farms," *IEEE Trans. Power Deliv.*, vol. 26, no. 4, pp. 2596–2604, 2011. 15, 18

[23] X. Zhao and K. Li, "Adaptive Backstepping Droop Controller Design for Multi-terminal High-Voltage Direct Current Systems," *IET Gener. Transm. Distrib.*, vol. 9, pp. 975–983, 2015. [Online]. Available: http://digital-library.theiet.org/content/journals/10.1049/iet-gtd.2014.0582 15, 21

[24] R. Teixeira Pinto, S. F. Rodrigues, P. Bauer, and J. Pierik, "Comparison of Direct Voltage Control Methods of Multi-Terminal DC (MTDC) Networks through Modular Dynamic Models," in *14th Eur. Conf. onPower Electron. Appl. (EPE 2011),*, 2011, pp. 1–10. 17, 19

[25] P. Kankanala, S. Member, S. C. Srivastava, S. Member, A. K. Srivastava, N. N. Schulz, A. The, M.-z. M. Voltage, and D. C. Mvdc, "Optimal Control of Voltage and Power in a Multi-Zonal MVDC Shipboard Power System," *IEEE Trans. Power Syst.*, vol. 27, no. 2, pp. 642–650, 2012. 18

[26] K. Rudion and A. G. Orths, "Offshore Power System Operation Planning Considering Energy Market Schedules," *IEEE Trans. Sustain. ENERGY*, vol. 4, no. 3, pp. 725–733, 2013. 18

[27] Y. Tokiwa, F. Ichikawa, and K. Suzuki, "Novel Control Strategies for HVDC System with Self-contained Converter Tokyo Electric Power Co ." *Electr. Eng. Japan*, vol. 113, no. 5, pp. 19–26, 1993. 19

[28] C. Dierckxsens, K. Srivastava, M. Reza, S. Cole, J. Beerten, and R. Belmans, "A Distributed DC Voltage Control Method for VSC MTDC Systems," *Electr. Power Syst. Res.*, vol. 82, no. 1, pp. 54–58, jan 2012. [Online]. Available: http://linkinghub.elsevier.com/retrieve/pii/S0378779611001933 19

[29] F. Gonzalez and J. Roldan, "Effects of DC Voltage Control Strategy on Voltage Response on Multi-Terminal HVDC following Loss of a Converter Station," in *Power Energy Soc. Gen. Meet. (PES), IEEE*, 2013. 19

[30] K. Rouzbehi, S. Member, A. Miranian, J. I. Candela, A. Luna, and P. Rodriguez, "A Generalized Voltage Droop Strategy for Control of Multiterminal DC Grids," *IEEE Trans. Ind. Appl.*, vol. 51, no. 1, pp. 607–618, 2015. 19

[31] R. T. Pinto, P. Bauer, S. F. Rodrigues, E. J. Wiggelinkhuizen, J. Pierik, and B. Ferreira, "A Novel Distributed Direct-Voltage Control Strategy for Grid Integration of Offshore Wind Energy Systems Through MTDC Network," *IEEE Ind. Electrinics*, vol. 60, no. 6, pp. 2429–2441, 2013. 19

[32] S. Rodrigues, S. Member, R. T. Pinto, P. Bauer, S. Member, and J. Pierik, "Optimal Power Flow Control of VSC-Based Multiterminal DC Network for Offshore Wind Integration in the North Sea," *IEEE J. Emerg. Sel. Top. Power Electron.*, vol. 1, no. 4, pp. 260–268, 2013. 19

[33] A. S. Abdel-khalik, S. Member, A. M. Massoud, A. A. Elserougi, and S. Ahmed, "Optimum Power Transmission-Based Droop Control Design for Multi-Terminal HVDC of Offshore Wind Farms," *IEEE Trans. Power Syst.*, vol. 28, no. 3, pp. 3401–3409, 2013. 20

[34] L. Xu and L. Yao, "DC voltage control and power dispatch of a multi-terminal HVDC system for integrating large offshore wind farms," *IET Renew. Power Gener.*, vol. 5, no. 3, p. 223, 2011. [Online]. Available: http://digital-library.theiet.org/content/journals/10.1049/iet-rpg.2010.0118 20

[35] J. Beerten and R. Belmans, "Modeling and Control of Multi-Terminal VSC HVDC Systems," *Energy Procedia*, vol. 24, pp. 123–130, jan 2012. [Online]. Available: http://linkinghub.elsevier.com/retrieve/pii/S1876610212011332 20

[36] M. Aragüés-Peñalba, A. Egea-Àlvarez, S. G. Arellano, and O. Gomis-Bellmunt, "Droop control for loss minimization in HVDC multi-terminal transmission systems for large offshore wind farms," *Electr. Power Syst. Res.*, vol. 112, pp. 48–55, jul 2014. [Online]. Available: http://linkinghub.elsevier.com/retrieve/pii/S037877961400100X 20

[37] E. Prieto-Araujo, A. Egea-Alvarez, S. F. Fekriasl, and O. Gomis-Bellmunt, "DC voltage droop control design for multi-terminal HVDC systems considering AC and DC grid dynamics," *IEEE Trans. Power Deliv.*, vol. PP, no. 99, pp. 1–11, 2015. 21

[38] N. R. Chauhudri and B. Chauhudri, "Adaptive Droop Control for Effective Power Sharing in Multi-Terminal DC (MTDC) Grids," *IEEE Trans. Power Syst.*, vol. 28, no. 1, pp. 21–29, 2013. 21, 44

[39] R. Eriksson, J. Beerten, M. Ghandhari, and S. Member, "Optimizing DC Voltage Droop Settings for AC / DC System Interactions," *IEEE Trans. Power Deliv.*, vol. 29, no. 1, pp. 362–369, 2014. 21

[40] X. Lu, J. M. Guerrero, K. Sun, and J. C. Vasquez, "An Improved Droop Control Method for DC Microgrids Based on Low Bandwidth Communication With DC Bus Voltage Restoration and Enhanced Current Sharing Accuracy," *IEEE Trans. Power Electron.*, vol. 29, no. 4, pp. 1800–1812, 2014. 21, 44

[41] X.-F. Wang, Y. Song, and M. Irving, *Modern Power systems Analyss.* Springer Science+Business Media, 2008. 22

[42] N. R. Chaudhuri, R. Majumder, B. Chaudhuri, and J. Pan, "Stability Analysis of VSC MTDC Grids Connected to Multimachine AC Systems," *IEEE Trans. Power Deliv.*, vol. 26, no. 4, pp. 2774–2784, oct 2011. [Online]. Available: http://ieeexplore.ieee.org/lpdocs/epic03/wrapper.htm?arnumber=6026937 22

[43] J. Beerten, S. D'Arco, and J. A. Suul, "Identification and Small-Signal Analysis of Interaction Modes in VSC MTDC Systems," *IEEE Trans. Power Deliv.*, vol. 31, no. 2, pp. 888–897, 2016. 22, 25

[44] M. Amin, J. A. Suul, S. D. Arco, E. Tedeschi, and M. Molinas, "Impact of state-space modelling fidelity on the small-signal dynamics of VSC-HVDC systems," *Conf. AC DC Power Transm. 11th IET Int.*, no. February 2015, pp. 1–11, 2015. 22

[45] G. Pinares and M. Bongiorno, "Modeling and Analysis of VSC-Based HVDC Systems for DC Network Stability Studies," *IEEE Trans. Power Deliv.*, vol. 31, no. 2, pp. 848–856, 2016. 24

[46] L. Xu and L. Fan, "Impedance-based resonance analysis in a vsc-hvdc system," *IEEE Trans. Power Deliv.*, vol. 28, no. 4, pp. 2209–2216, 2013. 24, 36

[47] W. Wenyuan, A. Beddard, M. Barnes, and O. Marjanovic, "Analysis of Active Power Control for VSC-HVDC," *Power Deliv. IEEE Trans.*, vol. 29, no. 4, pp. 1978–1988, 2014. [Online]. Available: http://ieeexplore.ieee.org/ielx7/61/6861487/06824844.pdf?tp={&}arnumber=6824844{&}isnumber=6861487 24

[48] B. Berggren, R. Majumder, and N. Johansson, "A Generic VSC HVDC Primary Control Structure Suitable for Stability Studies," pp. 1–8, 2013. 25

[49] M. Janaki, R. Thirumalaivasan, and N. Prabhu, "Design of robust controller for VSC based HVDC using Genetic Algorithm," *2014 Int. Conf. Adv. Electr. Eng.*, pp. 1–6, jan 2014. [Online]. Available: http://ieeexplore.ieee.org/lpdocs/epic03/wrapper.htm?arnumber=6838495 25

[50] H. Latorre, M. Ghandhari, and L. Söder, "Active and reactive power control of a VSC-HVdc," *Electr. Power Syst. Res.*, vol. 78, no. 10, pp. 1756–1763, oct 2008. [Online]. Available: http://linkinghub.elsevier.com/retrieve/pii/S0378779608000965 25

[51] T. M. Haileselassie, M. Molinas, and T. Undeland, "Multi-Terminal VSC-HVDC System for Integration of Offshore Wind Farms and Green Electrification of Platforms in the North Sea," in *Nord. Work. Power Ind. Electron.*, 2008, pp. 1–8. 25

[52] C. Bajracharya, M. Molinas, M. Ieee, J. A. Suul, T. M. Undeland, and F. Ieee, "Understanding of tuning techniques of converter controllers for VSC-HVDC," in *Nord. Work. Power Ind. Electron.*, 2008. 26

[53] R. Preece and J. V. Milanovic, "Tuning of a Damping Controller for Multiterminal VSC-HVDC Grids Using the Probabilistic Collocation Method," *IEEE Trans. Power Deliv.*, vol. 29, no. 1, pp. 318–326, feb 2014. [Online]. Available: http://ieeexplore.ieee.org/lpdocs/epic03/wrapper.htm?arnumber=6675861 26

[54] N. Nayak, S. Mishra, S. Choudhury, and P. Rout, "Optimal design of VSC based HVDC using Particle Swarm Optimization technique," *2012 2nd Int. Conf. Power, Control Embed. Syst.*, pp. 1–5, dec 2012. [Online]. Available: http://ieeexplore.ieee.org/lpdocs/epic03/wrapper.htm?arnumber=6508072 26

[55] M. Janaki, R. Thirumalaivasan, and N. Prabhu, "Design of robust controller for VSC based HVDC using Genetic Algorithm," *2014 Int. Conf. Adv. Electr. Eng.*, pp. 1–6, jan 2014. [Online]. Available: http://ieeexplore.ieee.org/lpdocs/epic03/wrapper.htm?arnumber=6838495 26

[56] S. Bernal-perez, S. Añó-villalba, R. Blasco-gimenez, and J. R. Derlée, "Efficiency and Fault Ride-Through Performance of a Diode-Rectifier- and VSC-Inverter-Based

HVDC Link for Offshore Wind Farms," *IEEE Trans. Ind. Electron.*, vol. 60, no. 6, pp. 2401–2409, 2013. 27

[57] B. Silva, C. L. Moreira, H. Leite, and J. A. P. Lopes, "Control Strategies for AC Fault Ride Through in Multiterminal HVDC Grids," *IEEE Trans. Power Deliv.*, vol. 29, no. 1, pp. 395–405, 2014. 27, 28, 29, 96, 101

[58] J. Wu, S. Zhang, and D. Xu, "Modeling and control of Multi-terminal HVDC with Offshore Wind Farm Integration and DC Chopper Based Protection strategies," *IECON 2013 - 39th Annu. Conf. IEEE Ind. Electron. Soc.*, pp. 1013–1018, nov 2013. [Online]. Available: http://ieeexplore.ieee.org/lpdocs/epic03/wrapper.htm?arnumber=6699272 27

[59] M. I. Daoud, A. M. Massoud, A. S. Abdel-khalik, A. Elserougi, and S. Ahmed, "A Flywheel Energy Storage System for Fault Ride Through Support of Grid-Connected VSC HVDC-Based Offshore Wind Farms," *IEEE Trans. Power Syst.*, vol. PP, no. 99, pp. 1–10, 2015. 27

[60] S. Nanou and S. Papathanassiou, "Evaluation of a Communication-Based Fault Ride-Through Scheme for Offshore Wind Farms Connected Through High-Voltage DC Links Based on Voltage Source Converter," *IET Renew. Power Gener.*, vol. 9, no. 8, pp. 882–891, nov 2015. [Online]. Available: http://digital-library.theiet.org/content/journals/10.1049/iet-rpg.2015.0017 28

[61] G. Ramtharan, A. Arulampalam, J. Ekanayake, F. Hughes, and N. Jenkins, "Fault Ride Through of Fully Rated Converter Wind Turbines With AC and DC Transmission Systems," *IET Renew. Power Gener.*, vol. 3, no. 4, p. 426, 2009. [Online]. Available: http://digital-library.theiet.org/content/journals/10.1049/iet-rpg.2008.0018 28, 90, 96

[62] W. Lu and B.-t. Ooi, "DC Overvoltage Control During Loss of Converter in Multiterminal Voltage-Source Converter-Based HVDC (M-VSC-HVDC)," *IEEE Trans. Power Deliv.*, vol. 18, no. 3, pp. 915–920, jul 2003. [Online]. Available: http://ieeexplore.ieee.org/lpdocs/epic03/wrapper.htm?arnumber=1208376 28

[63] C. Feltes, H. Wrede, and F. W. Koch, "Enhanced Fault Ride-Through Method for Wind Farms Connected to the Grid Through," *IEEE Trans. Power Syst.*, vol. 24, no. 3, pp. 1537–1546, 2009. 28, 96

[64] L. Xuan, S. Qiang, L. Wenhua, R. Hong, X. Shukai, and L. Xiaolin, "Fault Ride-Through Control and Its Impacts on Wind Generators in a VSC-HVDC System," in *2013 IEEE Int. Symp. Ind. Electron.* Ieee, may 2013, pp. 1–6. [Online]. Available: http://ieeexplore.ieee.org/lpdocs/epic03/wrapper.htm?arnumber=6563758 28

[65] J. Mohammadi, S. Afsharnia, and S. Vaez-Zadeh, "Efficient Fault-Ride-Through Control Strategy of DFIG-Based Wind Turbines During The Grid Faults," *Energy Convers. Manag.*, vol. 78, pp. 88–95, feb 2014. [Online]. Available: http://linkinghub.elsevier.com/retrieve/pii/S019689041300664X 28, 29

[66] L. Yang, Z. Xu, J. Stergaard, Z. Y. Dong, and K. P. Wong, "Advanced Control Strategy of DFIG Wind Turbines for Power System Fault Ride Through," *IEEE Trans. Power Syst.*, vol. 27, no. 2, pp. 713–722, 2012. 28, 29, 91

[67] a.D. Hansen and G. Michalke, "Multi-pole permanent magnet synchronous generator wind turbines' grid support capability in uninterrupted operation during grid faults," *IET Renew. Power Gener.*, vol. 3, no. 3, p. 333, 2009. 28, 29

[68] S. Muyeen, R. Takahashi, T. Murata, and J. Tamura, "Low voltage ride through capability enhancement of fixed speed wind generator," *2009 IEEE Bucharest PowerTech*, pp. 1–6, 2009. [Online]. Available: http://ieeexplore.ieee.org/lpdocs/epic03/wrapper.htm?arnumber=5282108 28

[69] S. M. Muyeen, R. Takahashi, T. Murata, and J. Tamura, "A Variable Speed Wind Turbine Control Strategy to Meet Wind Farm Grid Code Requirements," *IEEE Trans. Power Syst.*, vol. 25, no. 1, pp. 331–340, 2010. 29, 90, 91

[70] Y. Huang, X. Yuan, J. Hu, and P. Zhou, "Modeling of VSC Connected to Weak Grid for Stability Analysis of DC-Link Voltage Control," *IEEE J. Emerg. Sel. Top. Power Electron.*, vol. 3, no. 4, pp. 1193–1204, 2015. 36

[71] T. M. Haileselassie and K. Uhlen, "Power Flow Analysis of Multi-terminal HVDC Networks," *2011 IEEE Trondheim PowerTech*, no. 4, pp. 1–6, jun

2011. [Online]. Available: http://ieeexplore.ieee.org/lpdocs/epic03/wrapper.htm?arnumber=6019349 38

[72] M. A. Abdelwahed and E. F. El-Saadany, "Power Sharing Control Strategy of Multi-terminal VSC-HVDC Transmission Systems Utilizing Adaptive Voltage Droop," *IEEE Trans. Sustain. Energy*, vol. PP, no. 99, pp. 1–10, 2016. 42

[73] ——, "Droop Gains Selection Methodology for Offshore Multi-Terminal HVDC Networks," in *2016 IEEE Electr. Power Energy Conf.*, 2016, pp. 1–5. 44

[74] J. Peralta, H. Saad, and S. Dennetière, "Detailed and Averaged Models for a 401-Level MMCHVDC System," *IEEE Trans. Power Deliv.*, vol. 27, no. 3, pp. 1501–1508, 2012. 44

[75] S. Skogestad and I. Postlethwaite, *Multivariable Feedback Control Analysis and design*. JOHN WILEY & SONS, 2005. 47

[76] R. H. Byrd, R. B. Schnabel, and G. A. Shultz, "A Trust Region Algorithm for Nonlinearly Constrained Optimization," *SIAM J. Numer. Anal.*, vol. 24, no. 5, pp. 1152–1170, 1987. [Online]. Available: http://epubs.siam.org/doi/abs/10.1137/0724076 50

[77] K. Deb, *Multi-objective optimization using evolutionary algorithms*, 1st ed. JOHN WILEY & SONS, 2004, no. 1st edition. 73

[78] M. A. Abdelwahed and E. El-saadany, "Converter Outage Fault Ride-Through Control Strategy for Offshore MT-HVDC Network," in *2016 IEEE Can. Conf. Electr. Comput. Eng.*, 2016, pp. 1–6. 88

[79] M. Abdelwahed and E. F. El-Saadany, "DC voltage control for multi-terminal HVDC networks during permanent converter outage," in *2016 4th IEEE Int. Conf. Smart Energy Grid Eng. SEGE 2016*, 2016, pp. 41–45. 90

[80] N. Miller, J. Sanchez-Gasca, W. Price, and R. Delmerico, "Dynamic Modeling of GE 1.5 and 3.6 MW Wind Turbine-Generators for Stability Simulations," in *2003 IEEE Power Eng. Soc. Gen. Meet. (IEEE Cat. No.03CH37491)*, vol. 3, no. July, 2003, pp. 1977–1983. 91

APPENDIX

The state-space model of the Cigree system DC grid is as follows:

$$\dot{\boldsymbol{x}}_{\boldsymbol{DC}} = \boldsymbol{A}_{\boldsymbol{DC}}\, \boldsymbol{x}_{\boldsymbol{DC}} + \boldsymbol{B}_{\boldsymbol{DC}}\, \boldsymbol{u}_{\boldsymbol{DC}}, \quad \boldsymbol{y}_{\boldsymbol{DC}} = \boldsymbol{C}_{\boldsymbol{DC}}\, \boldsymbol{x}_{\boldsymbol{DC}} \tag{1}$$

where

$$B_{DC} = \begin{bmatrix} 0 & 0 & 0 \\ 0 & 0 & 0 \\ 0 & 0 & 0 \\ 0 & 0 & 0 \\ 0 & 0 & 0 \\ 0 & 0 & 0 \\ 0 & 0 & 0 \\ 0 & 0 & 0 \\ 0 & 0 & 0 \\ 0 & 0 & 0 \\ 0 & 0 & 0 \\ \frac{1}{C_4} & 0 & 0 \\ 0 & \frac{1}{C_5} & 0 \\ 0 & 0 & \frac{1}{C_6} \\ 0 & 0 & 0 \end{bmatrix} \tag{2}$$

$$C_{DC} = \begin{bmatrix} 0\,0\,0\,0\,0\,0\,0\,0\,0\,0\,0\,0\,1\,0\,0\,0 \\ 0\,0\,0\,0\,0\,0\,0\,0\,0\,0\,0\,0\,0\,1\,0\,0 \\ 0\,0\,0\,0\,0\,0\,0\,0\,0\,0\,0\,0\,0\,0\,1\,0 \end{bmatrix} \tag{3}$$

$$A_{DC} = \begin{bmatrix}
\frac{-R_{13}}{L_{13}} & 0 & 0 & 0 & 0 & 0 & 0 & 0 & \frac{-1}{L_{13}} & 0 & \frac{1}{L_{13}} & 0 & 0 & 0 & 0 \\
0 & \frac{-R_{14}}{L_{14}} & 0 & 0 & 0 & 0 & 0 & 0 & \frac{-1}{-R_{14}} & 0 & 0 & \frac{1}{-R_{14}} & 0 & 0 & 0 \\
0 & 0 & \frac{-R_{17}}{L_{17}} & 0 & 0 & 0 & 0 & 0 & \frac{1}{L_{17}} & 0 & 0 & 0 & 0 & 0 & \frac{-1}{L_{17}} \\
0 & 0 & 0 & \frac{-R_{27}}{L_{27}} & 0 & 0 & 0 & 0 & 0 & \frac{-1}{L_{27}} & 0 & 0 & 0 & 0 & \frac{-1}{L_{27}} \\
0 & 0 & 0 & 0 & \frac{-R_{36}}{L_{36}} & 0 & 0 & 0 & 0 & 0 & \frac{-1}{L_{36}} & 0 & 0 & \frac{1}{L_{36}} & 0 \\
0 & 0 & 0 & 0 & 0 & \frac{-R_45}{L_{45}} & 0 & 0 & 0 & 0 & 0 & \frac{-1}{L_{45}} & \frac{1}{L_{45}} & 0 & 0 \\
0 & 0 & 0 & 0 & 0 & 0 & \frac{-R_{47}}{L_{47}} & 0 & 0 & 0 & 0 & \frac{1}{L_{47}} & 0 & 0 & \frac{-1}{L_{47}} \\
0 & 0 & 0 & 0 & 0 & 0 & 0 & \frac{-R_{56}}{L_{56}} & 0 & 0 & 0 & 0 & \frac{-1}{L_{56}} & \frac{1}{L_{56}} & 0 \\
\frac{1}{C_1} & \frac{1}{C_1} & \frac{-1}{C_1} & 0 & 0 & 0 & 0 & 0 & \frac{-G_{D_1}}{C_1} & 0 & 0 & 0 & 0 & 0 & 0 \\
0 & 0 & 0 & \frac{1}{C_2} & 0 & 0 & 0 & 0 & 0 & \frac{-G_{D_2}}{C_2} & 0 & 0 & 0 & 0 & 0 \\
\frac{-1}{C_3} & 0 & 0 & 0 & \frac{1}{C_3} & 0 & 0 & 0 & 0 & 0 & \frac{-G_{D_1}}{C_3} & 0 & 0 & 0 & 0 \\
0 & \frac{-1}{C_4} & 0 & 0 & 0 & \frac{1}{C_4} & \frac{-1}{C_4} & 0 & 0 & 0 & 0 & 0 & 0 & 0 & 0 \\
0 & 0 & 0 & 0 & 0 & \frac{-1}{C_5} & 0 & \frac{1}{C_5} & 0 & 0 & 0 & 0 & 0 & 0 & 0 \\
0 & 0 & 0 & 0 & \frac{-1}{C_6} & 0 & 0 & \frac{-1}{C_6} & 0 & 0 & 0 & 0 & 0 & 0 & 0 \\
0 & 0 & \frac{1}{C_7} & \frac{-1}{C_7} & 0 & 0 & \frac{1}{C_7} & 0 & 0 & 0 & 0 & 0 & 0 & 0 & 0
\end{bmatrix} \tag{4}$$